# Universidade Federal do Espírito Santo

## Programa de Pós-Graduação em Astrofísica, Cosmologia e Gravitação

# Statistical tools in cosmology: model selection and covariance matrix comparison

## Tassia Andrade Ferreira

Thesis submitted as part of the requirements for the degree of

Doctor of Philosophy in Astronomy & Physics

Supervisor:      Prof. Dr. Valerio Marra

*Núcleo de Astrofísica e Cosmologia*

*Universidade Federal do Espírito Santo, Brazil*

Co-supervisor:   Prof. Dr. Scott Dodelson

*Department of Physics*

*Carnegie Mellon University, United States of America*

PPGCosmo

## 2021

**Universidade Federal do Espírito Santo**

**Centro de Ciências Exatas**

Programa de Pós-Graduação em Astrofísica, Cosmologia e Gravitação

**Statistical tools in cosmology: model selection and covariance matrix comparison**

Tassia Andrade Ferreira

A presente tese "*Statistical tools in cosmology: model selection and covariance matrix comparison*" foi submetida por *Tassia Andrade Ferreira* ao PPGCosmo, tendo sido apresentada e aprovada no ano de 2021 como parte dos requisitos para a obtenção do título de Doutora em Astronomia e Física.

Comissão avaliadora:

Prof. Dr. Valerio Marra (UFES), orientador,

Prof. Dr. Scott Dodelson (CMU, USA), co-orientador,

Profa. Dra. Mariana Penna-Lima (Universidade de Brasília),

Profa. Dra. Flávia Sobreira (Universidade Estadual de Campinas),

Prof. Dr. Martin Makler (Centro Brasileiro de Pesquisas Físicas).

# Abstract

Albeit $\Lambda$CDM's fame as the concordance model, there are many interesting mysteries worth exploring, such as the nature of dark energy. Here, we test the viability of several classes of scenarios of the dark sector with linear and non-linear interacting terms. To do so, we use a Bayesian model selection with data from type Ia supernovae, cosmic chronometers, cosmic microwave background and two sets of baryon acoustic oscillations measurements: 2-dimensional angular measurements (BAO2), and 3-dimensional angle-averaged measurements (BAO3). On the other hand, we consider covariance matrices, which are important tools for parameter estimation. We explore ways of compressing them by analysing their eigenvalues and signal-to-noise ratio, by employing a tomographic compression and, lastly, with the Massively Optimized Parameter Estimation and Data compression (MOPED). We find that MOPED is a powerful tool in the comparison of covariance matrices and, towards that end, we build a python code that uses a fast Monte Carlo simulation to obtain comprehensible values for differences between two covariance matrices. This method thus eliminates the need for a full cosmological analysis as we relate its output to the corresponding parameter constraints.

# Resumo

Apesar da fama do $\Lambda$CDM como o modelo de concordância, existem muitos mistérios interessantes que merecem ser explorados, tais como a natureza da energia escura. Aqui, nós testamos a viabilidade de várias classes de cenários do setor escuro com termos de interação lineares e não-lineares. Para este fim, nós usamos o modelo de seleção Bayesiana com dados de supernovas do tipo Ia, relógios cósmicos, radiação cósmica de fundo de micro-ondas e dois conjuntos de medidas de oscilações acústicas bariônicas: medidas angulares bidimensionais (BAO2) e medidas tridimensionais de média angular (BAO3). Em contrapartida, nós consideramos matrizes de covariância, as quais são ferramentas importantes para estimativas de parâmetros. Nós exploramos diferentes formas de comprimi-las analisando seus autovalores, a razão sinal-ruído, empregando a compressão tomográfica e, finalmente, utilizando o *Massively Optimized Parameter Estimation and Data compression* (MOPED). Nós encontramos que MOPED é uma ferramenta poderosa de compressão de matrizes de covariância e, para este fim, nós construímos um código em python que utiliza uma simulação rápida de *Monte Carlo* para obter valores compreensíveis relacionados à diferença entre duas matrizes de covariância. Este método, então, elimina a necessidade da análise cosmológica completa, pois relacionamos seus resultados aos obtidos a diferença em suas restrições de parâmetros.

# Acknowledgements

# Contents

# 7   Conclusion                                                                123

# Introduction

Space: the final frontier.

Star Trek

The standard cosmological model has been able to account for a myriad of cosmological observations and given us a rich and informative picture of the universe. Nonetheless, ΛCDM faces problems both observationally and theoretically. Some of these are the inconsistencies at small scales [1, 2] and the tensions between datasets, such as the famous $H_0$ crisis from local observations and the Cosmic Microwave Background (CMB) [3]; and, most recently, the disagreement on the value of $S_8$ between the Kilo-Degree Survey-1000 (KiDS-1000) and Planck experiments [4]. A review of the derivation and framework of the standard model is done in Chapter 2.

The momentum generated by these discoveries has been paving the way for a broader and more extensive study of the dark sector. A class of interacting models that alleviates some of the shortcomings of ΛCDM is presented in Chapter 3. We will see that some of these models are indistinguishable from the standard model, where model selection is concerned, for a combined analysis with a number of

observables.

The coming era of cosmological surveys will shed light to many paradigms, with an unprecedented amount of data yielding high-precision tests. As the datasets increase, however, so does the need for sophisticated statistical inference. In cosmology, the popular approach is to use Bayesian probability theory, where information is the key concept and data can be interpreted in the context of a theoretical model. Cosmological parameter inference is done by employing Bayesian statistics to produce posterior probability distributions (or likelihoods). This requires constructing a pipeline which can use Monte Carlo Markov Chains (MCMC), or Nested Sampling (NS), for example, to explore the parameter space. These methods rely on results from tens of thousands of model evaluations; with the current tools, analysing data from the upcoming Stage IV experiments could take several years [5].

One way of addressing this issue is to use data compression. In Chapter 4 we introduce cosmic shear statistics, which is the observable we use for examining four such methods to reduce the size of the covariance matrix, as described in Chapter 5. Since covariance matrices are one of the most challenging components of cosmological analyses, we seek to isolate its most essential parts to parameter estimation. The compression schemes are presented in increasing order of complexity, starting with the removal of 200 modes associated with the lowest eigenvalues, moving on to the 200 modes with the lowest signal-to-noise, then to compression at the tomographic level and, finally, with the Massively Optimized Parameter Estimation and Data compression (MOPED). We show that compression schemes are an important tool for comparing covariance matrices, thus laying down the groundwork for building an effective method of covariance matrix comparison.

Chapter 6 deals with the problem of comparing covariance matrices. The compressed covariance matrices are fed to a python code that produces results in terms

of the difference in their diagonal elements, and of the elements of their correlation matrices. These results are in good agreement with the interpretation derived from considering the differences in their parameter constraints. This indicates that the algorithm is capable of replacing a full cosmological analysis, in favour of a faster, and computationally cheaper alternative.

Finally, this thesis is concluded in Chapter 7, where the main results are summarised.

# Introduction to cosmology

To boldly go where no one has gone before.

Star Trek

## 2.1 Geometry and distances in the universe

### 2.1.1 The Cosmological Principle

The cosmological principle can be interpreted as a generalised form of the **Copernican Principle**, which states that the earth is not in any particularly privileged position in the universe [6]. The cosmological principle states that, for sufficiently large scales, the universe can be considered spatially homogeneous and isotropic. Homogeneity implies that the geometry of the universe looks the same in any point in space; isotropy, on the other hand, means that the universe is identical in all directions. This is a very strong hypothesis, and it is the base for all modern cosmology.

In order to better understand this principle, we introduce the concept of **fundamental observers** for each point in space, who see the universe as being isotropic.

This is important because two observers at the same given point, each with their own distinct velocities, cannot both see isotropy in the universe. To say that the universe is homogeneous, it is only necessary that all fundamental observers see isotropic angular distances for redshifts of up to third order, in agreement with the Copernican principle. Similarly, for the universe to be isotropic, these observers need to see an isotropic Cosmic Microwave Background (CMB) radiation for up to the octupole [7]. There are a multitude of observations which support the cosmological principle, like, for example, photons from the CMB travelling from different regions of the universe have similar temperatures. Other observations like the distribution of galaxies in the universe, and weak lensing, also provide evidence for this principle. The universe, however, is not homogeneous on small scales, and these inhomogeneities can be considered to be small perturbations evolving in the homogeneous background that is the universe. We will be discussing this important aspect later in this chapter.

## 2.1.2 The Friedmann–Lemaître–Robertson–Walker metric

As we just saw, the universe is homogeneous and isotropic in space, which implies that it has the maximum possible number of Killing vectors. We represent our spacetime with $\mathbf{R} \times \Sigma$, where $\mathbf{R}$ is the time direction and $\Sigma$ is a three-dimensional manifold. The line element of our metric is,

$$ds^2 = g_{\mu\nu}dx^\mu dx^\nu = -dt^2 + a^2(t)d\sigma^2 \ . \tag{2.1}$$

where, throughout the text, the Greek indices are [0,3] and the Latin indices are [1,3], and $c = 1$. The term $g_{\mu\nu}$ is the **metric tensor**, the function $a(t)$ is the cosmological **scale factor**, which describes how distances increase with time and, finally, $d\sigma^2 = \gamma_{ij}dx^i dx^j$, where $\gamma_{ij}$ is the three-dimensional spatial metric.

The coordinates of $d\sigma^2$ are known as the **comoving coordinates** and can be used to define the **comoving distance**, $\chi(r)$, as well as to describe fundamental observers [8].

To obtain information about the curvature of the universe, we need to calculate the **Riemann tensor**, or the **curvature tensor**, which, for maximally symmetric metrics, is given by [9]

$$\mathcal{R}_{ijkl} = K \left( \gamma_{ik}\gamma_{jl} - \gamma_{il}\gamma_{jk} \right) . \tag{2.2}$$

Its contraction, the **Ricci tensor**, is then

$$\gamma^{ik}\mathcal{R}_{ijkl} = K \left( \gamma^{ik}\gamma_{ik}\gamma_{jl} - \gamma^{ik}\gamma_{il}\gamma_{jk} \right) ,$$

$$R_{jl} = K \left( 3\gamma_{jl} - \gamma_{jl} \right) , \tag{2.3}$$

$$R_{jl} = 2K\gamma_{jl} ,$$

and we can obtain the constant $K$ by contracting both sides once more,

$$K = \frac{\mathcal{R}}{6} , \tag{2.4}$$

where $\mathcal{R}$ is the **Ricci scalar**. Substituting this result, gives

$$\mathcal{R}_{jl} = \frac{\mathcal{R}\gamma_{jl}}{3} . \tag{2.5}$$

Next, we take the most general metric for a static, spherically symmetric spacetime,

$$ds^2 = -e^{2\alpha(r)}dt^2 + e^{2\beta(r)}dr^2 + r^2(d\theta^2 + \sin^2\theta d\phi^2) , \tag{2.6}$$

with $r$ being the radial coordinate. Since we only want the spherical part, we set

$\alpha = 0$. To solve for $\beta(r)$, we evaluate the Christoffel symbols [9],

$$\Gamma^{\mu}_{\nu\lambda} = \frac{1}{2}g^{\mu\alpha}(g_{\alpha\nu,\lambda} + g_{\alpha\lambda,\nu} - g_{\nu\lambda,\alpha}) \ , \tag{2.7}$$

which yield,

$$\Gamma^{r}_{rr} = \partial_r\beta \ , \qquad\qquad \Gamma^{r}_{\theta\theta} = -re^{-2\beta} \ , \quad \Gamma^{r}_{\phi\phi} = -re^{-2\beta}\sin^2\theta \ ,$$
$$\Gamma^{\theta}_{\phi\phi} = -\sin\theta\cos\theta \ , \quad \Gamma^{\phi}_{\theta\phi} = \frac{\cos\theta}{\sin\theta} \ , \qquad \Gamma^{\theta}_{r\theta} = \Gamma^{\phi}_{r\phi} = \frac{1}{r} \ , \tag{2.8}$$

for the non-zero components. We can then calculate the Ricci tensor via,

$$\mathcal{R}_{\mu\nu} = \Gamma^{\alpha}_{\mu\nu,\alpha} - \Gamma^{\alpha}_{\mu\alpha,\nu} + \Gamma^{\alpha}_{\mu\nu}\Gamma^{\beta}_{\alpha\beta} - \Gamma^{\alpha}_{\mu\beta}\Gamma^{\beta}_{\alpha\nu} \ . \tag{2.9}$$

Plugging in the values, we have

$$\mathcal{R}_{rr} = \frac{2}{r}\partial_r\beta \ ,$$
$$\mathcal{R}_{\theta\theta} = e^{-2\beta}\left(r\partial_r\beta - 1\right) + 1 \ , \tag{2.10}$$
$$\mathcal{R}_{\phi\phi} = \left[e^{-2\beta}\left(r\partial_r\beta - 1\right) + 1\right]\sin^2\theta \ .$$

Finally, we can use Eq. (2.5) to find

$$\beta = -\frac{1}{2}\ln(1 - Kr^2) \ , \tag{2.11}$$

that we use to write Eq. (2.1) as

$$ds^2 = -dt^2 + a^2(t)\left[\frac{dr^2}{1 - Kr^2} + r^2(d\theta^2 + \sin^2\theta d\phi^2)\right] \ . \tag{2.12}$$

This equation is known as the **Friedmann–Lemaître–Robertson–Walker met-**

**ric** (FLRW). The constant $K$ can take the values $+1, 0, -1$ for an open, flat, and closed universe, respectively. In the case of a closed geometry, the universe is described by a three-sphere; for the flat case it is a quadridimensional pseudo-Euclidean space; and the open geometry is represented more simply by a saddle.

### 2.1.3 Cosmological redshift

Since most of the cosmological observations are obtained via electromagnetic waves, it is essential to understand how photons propagate in a homogeneous and isotropic universe.

Consider the comoving coordinate

$$\chi(r) = \begin{cases} \sin^{-1} r & (K = +1) , \\ r & (K = 0) , \\ \sinh^{-1} r & (K = -1) , \end{cases} \tag{2.13}$$

and the conformal time

$$\tau(t) = -\int_0^t \frac{dt'}{a(t')} . \tag{2.14}$$

We can then rewrite the metric in terms of $\chi$ and $\tau$,

$$ds^2 = a^2(\tau) \left[ d\tau^2 - d\chi^2 - f_K^2(\chi)(d\theta^2 + \sin^2 \theta d\phi^2) \right] , \tag{2.15}$$

where,

$$f_K(\chi) = \begin{cases} \sin \chi & (K = +1) , \\ \chi & (K = 0) , \\ \sinh \chi & (K = -1) , \end{cases} \tag{2.16}$$

Since photons move along a null geodesic, with $ds = 0$, their trajectories can be described by

$$d\tau(t) = d\chi(r) \; . \tag{2.17}$$

As such, when a pulse is emitted by a source at $r = r_e$ in the instant $t_e$, it will reach the observer at $r = 0$ in $t_0$, where

$$d\tau(t_0) - d\tau(t_e) = d\chi(r_e) \; . \tag{2.18}$$

For a successive pulse we then have

$$d\tau(t_0 + \delta t_0) - d\tau(t_e + \delta t_e) = d\chi(r_e) \; . \tag{2.19}$$

Since $\delta t_e \ll t_e$ and $\delta t_0 \ll t_0$, we can write

$$\frac{d\tau(t_0)}{a(t_0)} \approx \frac{d\tau(t_e)}{a(t_e)} \; , \tag{2.20}$$

and so its period, as well as its wavelength, increase proportionally to the scale factor. We thus define the redshift as the fractional change in wavelength,

$$z = \frac{\lambda_0 - \lambda_e}{\lambda_e} \; , \tag{2.21}$$

which, if we rewrite $a(t_0) = a_0$ and $a(t_e) = a$, can also be expressed as

$$1 + z = \frac{a_0}{a} \; . \tag{2.22}$$

The cosmological redshift was discovered by Edwin Hubble when analysing the spectral lines emitted by nearby galaxies which, in great part, were moving away from us [10]. Due to the expansion of the universe, the further an object is,

the faster it will be moving away from us. If we take, for example, the **Big Bang model**, which describes how the universe began, larger redshifts will then correspond to a younger universe. This is useful because it allows us to measure how far into the past we are probing, thus enabling a study of the dynamics of the universe at different epochs, and to test our different hypotheses.

On the other hand, for nearby objects, such as those in our Local Group[1], we observe a blueshift, which indicates that they are moving towards us. This occurs mostly due to gravitational effects, which attract nearby galaxies in such a way that the expansion of the universe is subdominant. The blueshift can also be used to determine the direction of the rotation of binary systems in the universe.

### 2.1.4 The Friedmann equations

Before presenting the **Friedmannn equations**, we start with a brief overview of the **Einstein equations**, which relate the geometry of spacetime to the matter and energy content of the universe. In Einstein's General Relativity (GR), gravity is a manifestation of the curvature of spacetime; this is well illustrated in **Einstein's equation**,

$$G_{\mu\nu} = \mathcal{R}_{\mu\nu} - \frac{1}{2}g_{\mu\nu}\mathcal{R} = 8\pi G T_{\mu\nu} \ , \tag{2.23}$$

where $G_{\mu\nu}$ is called the **Einstein tensor**, $G$ is the gravitational constant and $T_{\mu\nu}$ is the **energy-momentum tensor**. The lhs of Eq. (2.23) characterises the geometry of the universe, while the rhs describes the energy and the momentum of

---

[1]It is the group of galaxies that the Milky Way belongs to; its diameter is approximately 3 Mpc [11]

its components [12]. We use Eq. (2.7) to obtain the non-zero Christoffel symbols,

$$\Gamma^t_{rr} = \frac{a^2 H}{1 - K r^2} \ , \qquad \Gamma^r_{rr} = \frac{K r}{1 - K r^2} \ , \qquad \Gamma^\theta_{\phi\phi} = -\sin\theta\cos\theta \ ,$$

$$\Gamma^t_{\theta\theta} = a^2 H r^2 \ , \qquad \Gamma^r_{\theta\theta} = -r(1 - K r^2) \ , \qquad \Gamma^\theta_{\phi\theta} = \cot\theta \ ,$$

$$\Gamma^t_{\phi\phi} = a^2 H r^2 \sin^2\theta \ , \qquad \Gamma^r_{\phi\phi} = -r(1 - K r^2)\sin^2\theta \ , \qquad \Gamma^\theta_{r\theta} = \Gamma^\phi_{r\phi} = \frac{1}{r} \ ,$$

$$\Gamma^r_{tr} = \Gamma^\theta_{t\theta} = \Gamma^\phi_{t\phi} = H \ ,$$

$$\tag{2.24}$$

where we've defined the **Hubble parameter**, $H = \frac{\dot{a}}{a}$. We can then obtain the Ricci tensor

$$\mathcal{R}_{00} = -3\frac{\ddot{a}}{a} \ ,$$

$$\tag{2.25}$$

$$\mathcal{R}_{ij} = \left[ \frac{\ddot{a}}{a} + 2\left(\frac{\dot{a}}{a}\right)^2 + 2\frac{K}{a^2} \right] g_{ij} \ ,$$

which leads to

$$\mathcal{R} = 6\left[ \frac{\ddot{a}}{a} + \left(\frac{\dot{a}}{a}\right)^2 + \frac{K}{a^2} \right] \ . \tag{2.26}$$

We have thus worked out the lhs of Einstein's equation, our next step is to tackle the rhs. The energy-momentum tensor of a perfect, isotropic fluid, is

$$T_{\mu\nu} = \begin{pmatrix} \rho & 0 & 0 & 0 \\ 0 & p & 0 & 0 \\ 0 & 0 & p & 0 \\ 0 & 0 & 0 & p \end{pmatrix} \ , \tag{2.27}$$

where $\rho$ is the density and $p$ is the pressure of the fluid. To obtain the evolution of the scale factor, we need only take the time-time component of Eq. (2.23),

$$\mathcal{R}_{00} - \frac{1}{2} g_{00} \mathcal{R} = 8\pi G T_{00} \ , \tag{2.28}$$

which yields

$$H^2 = \frac{8\pi G}{3}\rho + \frac{K}{a^2} \ . \tag{2.29}$$

And, for the spatial components

$$\left(\frac{\ddot{a}}{a} + H^2 + \frac{K}{a^2}\right) g_{ij} = -8\pi G T_{ij} \ . \tag{2.30}$$

If we substitute Eq. (2.29) in Eq. (2.30), and take its trace, we have

$$\frac{\ddot{a}}{a} = -\frac{4\pi G}{3}(\rho + 3p) \ . \tag{2.31}$$

We have thus derived the **Friedmann equations**, which correspond to Eqs. 2.29 and 2.31.

You will notice that I have not included the $\Lambda$ term up till this point, and if this makes you anxious, worry not. The reason for this is that I am interpreting $\Lambda$ as being a fluid, and it is thus contained in the rhs of Einstein's equation, i.e. in the $T_{\mu\nu}$. $\Lambda$ will be properly introduced when we come to the section which deals with the components of the universe.

## 2.1.5 Measuring distances in the universe

### 2.1.5.1 Proper distance

We can define the **proper distance**, $d_p$, as the spatial geodesic for two points in the universe at a given value for $a(t)$. For two observables at $(0, \theta, \phi)$ and $(r, \theta, \phi)$ , we have

$$d_p = a(t) \int_0^r \frac{dr'}{\sqrt{1 - Kr'^2}} = a(t)\chi(r) \ , \tag{2.32}$$

where $\chi(r)$ depends on the value of $K$, as described by Eq. (2.13). In the absence of a peculiar velocity, the relative velocity of an object is then

$$\dot{d}_p = H d_p \ , \tag{2.33}$$

or, alternatively, $H_0 d_p$ if we take the value of the Hubble constant evaluated today. The above expression is known as the **Hubble-Lemaître law**. It states that, for small enough redshifts, the observed recession velocity increases linearly with the distance. In 1929, when Hubble first discovered it, he measured $H_0 \approx 500$ km s$^{-1}$ Mpc$^{-1}$ [10]. The current value today stands at $73.2 \pm 1.3$ km s$^{-1}$ Mpc$^{-1}$ [13], or $69.6 \pm 0.8$ km s$^{-1}$ Mpc$^{-1}$ [14], or $67.4 \pm 0.5$ km s$^{-1}$ Mpc$^{-1}$ [15]. The large discrepancy between Hubble's value and today's was due to an incorrect calibration of the Cepheid stars used, which yield distances that were underestimated by a factor $\sim 7$; the correct value would thus have been $H_0 \approx 71.4$ km s$^{-1}$ Mpc$^{-1}$ [16].

### 2.1.5.2 Luminosity distance

Consider a luminous object at a distance $d_L$, in flat space, its flux, over the luminosity is inversely proportional to the area of a sphere centred around the object

$$\frac{\mathcal{F}}{L_s} = \frac{1}{4\pi d_L^2} \ . \tag{2.34}$$

In an expanding universe, however, this is slightly different. Since the flux is diluted, its absolute luminosity, $L_s$, at the source, is not the same as the observed luminosity, $L_0$. The flux is then

$$\mathcal{F} = \frac{L_0}{4\pi f_K(\chi)^2} \ , \tag{2.35}$$

and the luminosity distance becomes

$$d_L^2 = f_K(\chi)^2 \frac{L_s}{L_0} \ . \tag{2.36}$$

To find the ratio between the luminosities, we have two factors to consider: the energy of the photon and the time it takes to reach us. The wavelength of the photon is inversely proportional to its energy, therefore $\Delta E_s / \Delta E_0 = 1 + z$. The interval of time, $\Delta t$ between the emission of one photon and the next is also dilated, such that it is measured at $(1 + z)\Delta t$ apart. Combining these, we have

$$d_L = (1 + z) f_K(\chi) \ . \tag{2.37}$$

We can derive a final expression by taking Eqs 2.16 and 2.17, such that

$$\chi = \int_t^0 \frac{dt'}{a(t')} \ , \tag{2.38}$$

where we can change the integration variable $t \to a$,

$$\chi = \int_a^1 \frac{da'}{a'^2 H(a')} \ , \tag{2.39}$$

and, if we change the integration variable a second time, $a \to z$,

$$\chi = \int_0^z \frac{dz'}{H(z')} \ . \tag{2.40}$$

We can finally rewrite Eq. (2.37),

$$d_L = \frac{1 + z}{\sqrt{-K}} \sinh \left( \sqrt{-K} \int_0^z \frac{dz'}{H(z')} \right) \ , \tag{2.41}$$

or

$$d_L = (1 + z) \int_0^z \frac{dz'}{H(z')} \; , \tag{2.42}$$

for a flat universe.

### 2.1.5.3 Angular diameter distance

The angular diameter distance is more commonly employed when dealing with larger objects such as galaxies and galaxy clusters, since it takes into consideration the angle $\theta$ that subtends the proper size of the object, $R$. The angular diameter distance is defined as

$$\begin{aligned} d_A &= \frac{R}{\theta} \; , \\ &= \frac{f_K(\chi)}{(1 + z)} \; , \end{aligned} \tag{2.43}$$

which conveniently reduces to

$$d_A = \frac{d_L}{(1 + z)^2} \; , \tag{2.44}$$

which is known as Etherington's reciprocity theorem. Despite its name, this equation was first derived by Richard Tolman, in 1930 [17], and was later revisited by Ivor Etherington in 1933 [18], where he critic ised Tolman's different definition of brightness. In his paper, Etherington's equation lacks the square factor, but he concluded by claiming that both his and Tolman's results are in agreement.

## 2.2 Contents of the universe

The Friedmann equations introduced in the previous section include terms describing the pressure and the energy density of the components of the universe. In this section we discuss what these components are and how the composition of

the universe has evolved through time.

### 2.2.1 The conservation of energy and the equation of state

We have previously shown the energy-momentum tensor, $T_{\mu\nu}$, in its matrix form in Eq. (2.27). Its covariant conservation is

$$\nabla_\mu T^{\mu\nu} = \partial_\mu T^{\mu\nu} + \Gamma^\mu_{\mu\lambda} T^{\lambda\nu} + \Gamma^\nu_{\mu\lambda} T^{\mu\lambda} = 0 . \tag{2.45}$$

For $\nu = 0$, we have

$$\dot{\rho} = -3\frac{\dot{a}}{a}(\rho + p) , \tag{2.46}$$

and, for $\nu = i$,

$$\partial_i p = 0 . \tag{2.47}$$

The **conservation equation** then amounts to Eq. (2.46). We consider **equations of state** of the form

$$p = \omega\rho . \tag{2.48}$$

If we plug this in Eq. (2.46),

$$\rho \propto a^{-3(1+\omega)} , \tag{2.49}$$

which relates the evolution of the energy density to the scale factor, $a$, and the equation of state, $\omega$.

### 2.2.2 Components of the universe

The three types of perfect fluids which have equations of state as presented in Eq. (2.48), and make up the universe we live in, are: dust, relativistic particles, and vacuum energy. In this section, we give a brief overview of each.

We start with dust, which is taken to be any kind of matter that is non-

relativistic, such as baryonic matter, which makes up everything that we see, from trees to planets, to stars, and dark matter, that will be discussed in the next subsection. Dust is pressureless, thus $p = 0$ and $\rho_m \propto a^{-3}$. The next component are the relativistic particles, that can be approximated to an ultra-relativistic radiation fluid. In their case, $\omega = 1/3$, and so $\rho_r \propto a^{-4}$, which is expected, since the energy per photon scales as $a^{-1}$ and the number density of photons as $a^{-3}$.

Finally, we have the **vacuum energy**, also referred to as the zero-point energy, which is a well-known quantity in Quantum Field Theory. Consider the Hamiltonian of a quantum harmonic oscillator [19],

$$\mathcal{H} = \hbar\omega \left( a^\dagger a + \frac{1}{2} \right) \, , \tag{2.50}$$

where, $\omega$ is the frequency, and the ladder operators obey the commutation relation $\left[ a, a^\dagger \right] = 1$. If we apply the vacuum state,

$$\mathcal{H} \left| 0 \right\rangle = \frac{1}{2} \hbar\omega \left| 0 \right\rangle \, , \tag{2.51}$$

then, the zero-point energy, $\frac{1}{2}\hbar\omega$, is an eigenvalue of $\mathcal{H}$. Since the laws of physics are universal, this energy should also exist in a cosmological context. It does, in fact, we have included it in the rhs of Eq. (2.23). We can write it now explicitly

$$\mathcal{R}_{\mu\nu} - \frac{1}{2} g_{\mu\nu} \mathcal{R} = 8\pi G \left( T^{(\mathrm{m})}_{\mu\nu} + T^{(\mathrm{vac})}_{\mu\nu} \right) \, , \tag{2.52}$$

where the (m) and the (vac) indices represent matter and vacuum, respectively. The energy-momentum tensor for vacuum is

$$T^{(\mathrm{vac})}_{\mu\nu} = -\rho_{\mathrm{vac}} g_{\mu\nu} \, , \tag{2.53}$$

which implies that the fluid has negative density. In other words, its internal

energy increases as it expands. Before we continue our discussion of this strange fluid, we conclude our derivation for the equation of state for the components of the universe: we find that $\omega = -1$ and $\rho_{\text{vac}} \propto a^0$.

If we replace $\rho_{\text{vac}}$ with the famous **cosmological constant**, $\Lambda$, we can rearrange Eq. (2.52),

$$\mathcal{R}_{\mu\nu} - \frac{1}{2}g_{\mu\nu}\mathcal{R} + \Lambda g_{\mu\nu} = 8\pi G T_{\mu\nu} \ . \tag{2.54}$$

Eqs. 2.52 and 2.54 may look similar, but they mean different things. The cosmological constant on the rhs tells the reader that we perceive it as a fluid, it is a component of the universe just as radiation and matter are. When it is placed on the lhs, however, then it is seen as a geometric property of spacetime.

The cosmological constant was first introduced by Albert Einstein, in 1917, in his attempt to create a static cosmological model. This was done to explain the cosmological observations of the time, which seemed to imply that the universe was static. Einstein removed the cosmological constant from his equations a few years later, following Hubble's discovery in 1929 that the universe was, in fact, expanding [10][2]. Einstein did not live long enough to see his cosmological constant be invoked, once again, in 1998, as two independent groups discovered, using data from type Ia supernovae, that the universe is in a state of accelerated expansion [20, 21]. This acceleration was attributed to a **dark energy**, as consequence of its equation of state, since $\rho + 3p < 0$ causes an accelerated expansion. The cosmological constant is currently the best candidate for dark energy, since it is capable of describing most of our cosmological observations. We call this the $\Lambda$ **Cold Dark Matter model**, or $\Lambda$CDM, and this is the cosmological model adopted throughout this thesis, unless otherwise stated.

The equation describing the evolution of the components of $\Lambda$CDM model is a

---

[2]The author takes this opportunity to note here how dangerous it is to succumb to petty pressure from one's colleagues, as science is best done when one works with honesty, such that their work is legitimate and open to constructive criticism.

simple one, but before deriving it, we first introduce the **density parameter**,

$$\Omega = \frac{8\pi G}{3H^2}\rho = \frac{\rho}{\rho_{\mathrm{crit}}} \ , \tag{2.55}$$

where $\rho_{\mathrm{crit}}$ is the critical density. This allows us to write the Friedmann equation in the form

$$H(z) = H_0\big[\Omega_{m0}(1+z)^3 + \Omega_{r0}(1+z)^4 + \Omega_{\Lambda 0} + \Omega_{K0}(1+z)^2\big]^{1/2} \ , \tag{2.56}$$

by considering the contribution of the spatial curvature as an energy density,

$$\Omega_K = -\frac{K}{H^2 a^2} \ , \tag{2.57}$$

and with the subscript 0 indicating that we are considering the value of the parameter evaluated today.

## 2.3 The $\Lambda$CDM model

As previously stated, the $\Lambda$CDM model, sometimes referred to as the **concordance**, or the **standard**, **model**, has been able to account for and reproduce most of our observations of the universe. Despite its success, many of its aspects remain a mystery. The aforementioned dark energy, in particular, has only had its effects observed, but we know nothing of its nature. Moreover, while vacuum energy has proven to be an excellent candidate, there is yet the problem of its observed value. The estimated value obtained from particle physics and the observed value of dark energy differ by about 120 orders of magnitude [22]. If the value from particle physics were to be believed, then we would not have had to worry about defending a thesis, because the universe would have long been shred

to pieces. There are a number of models which attempt to explain the acceleration of the universe via other mechanisms. The **quintessence model** [23, 24, 25], for example, associates dark energy to a scalar field with $-1 < w < -1/3$, allowing both its density and equation of state to vary in time. Another alternative are theories of modified gravity, like the Horndeski theories [26], which were very popular until being largely constrained by observations of gravitational waves from black hole mergers [27]. Finally, we can have a dynamic, or an interacting dark energy, which will be discussed in the next chapter.

The second part of the standard model's name: Cold Dark Matter, is yet another large unknown. We talked about baryonic matter, which we can see, but only makes up less than 5% of the composition of the universe, whereas **dark matter** makes up about 25%. Dark matter is so called because it is not detectable via the emission of electromagnetic radiation; its presence is inferred through its gravitational interactions. Although dark matter was first proposed by Fritz Zwicky, in 1933 [28], when studying Coma cluster, solid evidence for its existence was only found decades later, by Vera Rubin, in 1970, as she analysed the rotation curve of the Andromeda galaxy [29]. Since then, there have been a number of evidences for dark matter, such as from gravitational lensing [30], x-ray emission from cluster collisions [31] and the formation of structures [32]. Due to this different kind of matter, $\Omega_m$ can sometimes be broken into $\Omega_m = \Omega_b + \Omega_{dm}$.

Finally, we introduce the **cosmological parameters** that will be relevant to this thesis:

- the *dimensionless Hubble parameter*, $h = H_0/100$ s Mpc km$^{-1}$. We will be interchanging between $h$ and $H_0$;

- the *parameter combination* $S_8 = \sigma_8(\Omega_m/0.3)^{0.5}$, which is a convenient way to break the degeneracy of the parameter space in the $\Omega_m - \sigma_8$ plane, where $\sigma_8$ measures the amplitude of the power spectrum on the scale of $8h^{-1}$ Mpc;

- the *density parameter for matter*, $\Omega_m$, as well as the ones for baryons and dark matter, will, at times, be replaced by $\Omega_m h^2 = \Omega_b h^2 + \Omega_c h^2$;

- the *scalar spectral index* (or *tilt*), $n_s$, describes the scale-dependence of the power spectrum;

- the *density parameter of neutrinos*, $\Omega_\nu h^2 = \frac{\Sigma m_\nu}{93.14\text{eV}}$, where $m_\nu$ are the neutrino masses;

- the *ionization optical depth*, $\tau$.

Throughout, we will assume a flat universe and, where relevant, we will be declaring the fixed values for other relevant parameters.

# Bayesian comparison of interacting scenarios

Oft hope is born when all is forlorn.

The Return of the King

In this chapter I will detail the work I did in collaboration with Antonella Cid, Beethoven Santos, Cassio Pigozzo and Jailson Alcaniz, in [33].

## 3.1 Motivation

One of the inconsistencies of the standard cosmological model is the large disagreement between the predicted and the observed value of the cosmological constant. In this chapter we deal with a class of models that have an interacting dark sector (composed of dark energy and dark matter) that allows for a mechanism in which dark energy decays into dark matter, thus alleviating the cosmological problem. This approach has been explored in various contexts, such as for a modified Chaplygin gas, which introduces a varying equation of state for dark energy [34, 35], and

the aforementioned quintessence model [23, 24, 25]. Another question raised by the standard model is in regard to the observed values for the energy densities of dark energy and matter, which are of the same order. This fortunate circumstance is known as the **coincidence problem** and is yet unexplained by the standard model. Most of the models studied in this chapter have been proposed in the literature as a way of obtaining a scaling solution for this problem, since they favour a universe that progresses to a stationary stage where the ratio between these two densities becomes a constant [36, 37, 38, 39, 40].

We test the viability of twenty-one such models by comparing them against the standard model using a Bayesian analysis with data from Type Ia Supernovae, Baryon Acoustic Oscillations, the CMB, and Cosmic Chronometers.

## 3.2 Interacting Cosmological Scenarios

The models presented here follow the same construction as $\Lambda$CDM, in the sense that there is no modification to the Einstein equations, and that the conservation of energy holds. This approach is purely phenomenological, and only applies to the components of the dark sector, such that Eq. (3.2) is rewritten as

$$\dot{\rho}_{dm} + 3\gamma_{dm}H\rho_{dm} = -Q \; ,$$

$$\dot{\rho}_{x} + 3\gamma_{x}H\rho_{x} = Q \; ,$$

(3.1)

where $Q$ is the function that describes the interaction between the two terms, $\gamma_i = 1 + \omega_i$, and we replace the $\lambda$ subscript with $x$, for dark energy. By changing the derivation variable $t \rightarrow 2\ln a$, and with the prime denoting the derivative with

respect to this new variable, we have

$$\rho'_{dm} + \rho_{dm} = -\Gamma \ ,$$

$$\rho'_x + \gamma_x \rho_x = \Gamma \ , \tag{3.2}$$

with $\Gamma = Q/3H$. This allows for a two-way transfer between dark energy and dark matter, only depending on the value of $\Gamma$: if positive, then dark matter decays to dark energy and, if negative, the opposite occurs. The total energy density, and its derivative, for the two-fluid model is [38]

$$\rho = \rho_{dm} + \rho_x \ ,$$

$$\rho' = -\rho_{dm} - \gamma_x \rho_x \ , \tag{3.3}$$

which can be used to obtain

$$\rho_{dm} = -\frac{\gamma_x \rho + \rho'}{1 - \gamma_x} \ ,$$

$$\rho_x = \frac{\rho + \rho'}{1 - \gamma_x} \ . \tag{3.4}$$

Differentiating either of the above equations, and substituting Eq. (3.2), gives us a second order differential equation,

$$\rho'' + (1 + \gamma_x)\rho' + \gamma_x \rho = (1 - \gamma_x)\Gamma \ . \tag{3.5}$$

Table 3.1 shows the five types of interactions considered, which can be either linear, or nonlinear. We now introduce two additional parameters, $\alpha$ and $\beta$, both of which are varied in our cosmological analyses. By adopting the different forms for $\Gamma$, we

can rewrite Eq. (3.5) in terms of the constants $b_1, b_2$ and $b_3$,

$$\rho(\rho'' + b_1\rho' + b_3\rho) + b_2\rho'^2 = 0 . \tag{3.6}$$

The evolution of the dark sector can be described by solving Eq. (3.5),

$$\rho(a) = 3H_0^2(C_1 a^{3\lambda_1} + C_2 a^{3\lambda_2})^{\frac{1}{1+b_2}} , \tag{3.7}$$

where
$$C_1 = (\Omega_{dm0} + \Omega_{x0})^{1+b_2} - C_2 ,$$

$$C_2 = \frac{(\Omega_{dm0} + \gamma_x\Omega_{x0})(1+b_2) + \lambda_1(\Omega_{dm0} + \Omega_{x0})}{(\Omega_{dm0} + \Omega_{x0})^{-b_2}(\lambda_1 - \lambda_2)} ,$$

$$\lambda_1 = \frac{1}{2}\left(-b_1 - \sqrt{b_1^2 - 4b_3(1+b_2)}\right) , \tag{3.8}$$

$$\lambda_2 = \frac{1}{2}\left(-b_1 + \sqrt{b_1^2 - 4b_3(1+b_2)}\right) .$$

Finally, the Hubble expansion can be obtained, in a flat universe, by including the contribution of baryons and radiation in addition to that of the dark sector,

$$H(z) = H_0\left(\Omega_{r0}(1+z)^4 + \Omega_{b0}(1+z)^3 + \left[C_1(1+z)^{-3\lambda_1} + C_2(1+z)^{-3\lambda_2}\right]^{\frac{1}{1+b_2}}\right)^{1/2} . \tag{3.9}$$

While an extensive study of the these classes of interacting models had not yet been carried out, they are not particularly new. The $\Gamma_a$ interaction was first proposed by [25] and [39] in the form of a coupling between quintessence scalar field and a pressureless cold dark matter field. The authors of [38] found that an analytical solution for the dark sector and suggested that interaction $\Gamma_b$ could, in fact, alleviate the coincidence problem. Interaction $\Gamma_c$, on the other hand, was first presented by [36] to solve this problem in terms of a non-canonical scaling of the ratio of the energy densities of the components of the dark sector. Lastly,

models $\Gamma_d$ and $\Gamma_e$ were analysed in [37] in the context of non-linear interactions.

Table 3.1: Definitions of the parameters $b_1$, $b_2$, $b_3$ for interactions $\Gamma(\rho, \rho', \rho'')$.

| Interaction | $b_1$ | $b_2$ | $b_3$ |
|---|---|---|---|
| $\Gamma_a = \alpha\rho_{dm} + \beta\rho_x$ | $1 + \gamma_x + \alpha - \beta$ | $0$ | $\gamma_x + \alpha\gamma_x - \beta$ |
| $\Gamma_b = \alpha\rho'_{dm} + \beta\rho'_x$ | $(1 + \gamma_x + \alpha\gamma_x - \beta)/(1 + \alpha - \beta)$ | $0$ | $\gamma_x/(1 + \alpha - \beta)$ |
| $\Gamma_c = \alpha\rho_{dm}\rho_x/\rho$ | $1 + \gamma_x + \alpha(1 + \gamma_x)/(1 - \gamma_x)$ | $\alpha/(1 - \gamma_x)$ | $\gamma_x + \alpha\gamma_x/(1 - \gamma_x)$ |
| $\Gamma_d = \alpha\rho^2_{dm}/\rho$ | $1 + \gamma_x - 2\alpha\gamma_x/(1 - \gamma_x)$ | $-\alpha/(1 - \gamma_x)$ | $\gamma_x - \alpha\gamma^2_x/(1 - \gamma_x)$ |
| $\Gamma_e = \alpha\rho^2_x/\rho$ | $1 + \gamma_x - 2\alpha/(1 - \gamma_x)$ | $-\alpha/(1 - \gamma_x)$ | $\gamma_x - \alpha/(1 - \gamma_x)$ |

## 3.3 Data description

### 3.3.1 Baryon Acoustic Oscillations

The **Baryon Acoustic Oscillations** (BAO) have their origin at the time when the universe was an ionised fluid composed of photons and baryons that were coupled via Thomson scattering. The interactions between the larger pressure exerted by photons, and the smaller gravitational forces in the perturbations of the baryons, give rise to oscillations of the baryon-photon fluid. These oscillations are similar to sound waves, and hence we refer to their velocities as the **sound speed**, which can be calculated with

$$c_s = \frac{1}{\sqrt{3\left[1 + (3\Omega_{b,0}/4\Omega_{\gamma,0})(1 + z)^{-1}\right]}} \ . \tag{3.10}$$

During recombination, the universe becomes neutral, and the radiation pressure dissipates. At this point, the baryonic configuration freezes, while the photons start to propagate freely, forming a smooth distribution and giving rise to the CMB. As baryons and dark matter interact gravitationally, baryonic matter begins to accumulate at this scale, creating a spherical shell centred at the original

perturbation. This, in turn, fuels the probability of a galaxy being formed close to the remnants of the frozen baryonic wave [41, 42].

If a galaxy were to be formed at the centre of the initial perturbation, it would lead to a bump in the two-point correlation function at the radius of the shell, $r_s$, which would characterise an increase in the probability of finding two galaxies separated by $r_s$. This scale is the maximum distance for which the sound wave can travel in the photon-baryon fluid, from the fluid's formation to the acoustic horizon. We thus obtain

$$r_s = \int \frac{c_s(t)}{a(t)} dt = \int_{z_d}^{\infty} \frac{c_s(z)}{H(z)} dz \ , \tag{3.11}$$

where $r_d = r_s(z_d)$, evaluated at the redshift of the baryon drag epoch, that is, at the moment when the baryons break free from the Compton drag of the photons [43].

We can use BAOs to obtain the **Statistical Standard Ruler** (SSR), which is based on the premise that galaxy clusters and other observables can have a preferential scale, at which, when observed at different redshifts, can be used to constrain the angular diameter distance [44]. In our analyses, we use two different ways of obtaining information from BAOs, termed as BAO3 and BAO2.

### 3.3.1.1 BAO3

Since a change in the cosmological model should not affect $r_s$ significantly, we can treat these variations as a singular dilation in scale. To calculate these, we combine the line-of-sight and transverse dilations to find [45]

$$D_V(z) = \left[ (1+z)^2 \, d_A(z)^2 \frac{z}{H(z)} \right]^{1/3} \ , \tag{3.12}$$

where $d_A(z)$ is the angular diameter distance defined in Eq. (2.44). The **isotropic** BAO measurements are given by the dimensionless ratio,

$$d_z(z) = \frac{D_V(z)}{r_s} \; .$$

(3.13)

On the other hand, since BAO can be approximated to a linear phenomenon, we can disregard its nonlinear effects, so that BAO can be employed as an absolute Alcock-Paczynski test to obtain the product $d_A(z) \times H(z)$ [41]. These two quantities are recovered independently with the Hubble parameter being related to the characteristic scale, $r_\parallel(z)$ along the line-of-sight,

$$H(z) = \frac{\Delta z}{r_\parallel(z)} \; ,$$

(3.14)

and the transverse direction, $r_\perp(z)$, providing the angular diameter distance

$$d_A(z) = \frac{r_\perp(z)}{\Delta\theta(1+z)} \; .$$

(3.15)

These two quantities, which make up the **anisotropic** measurements, are correlated and their corresponding covariance matrices are found in their respective references for BOSS DR12 [46] and BOSS-Ly$\alpha$ [47]. The measurements used for BAO3 are found in Table 3.2.

Before using sets of BAO measurements from different surveys, we have to consider if they can be combined. This is a crucial decision when using different datasets because we have to take into account their correlations. We found that a joint analysis with SDDS-MGS [48], 6dFGS [49] and BOSS-LOWZ [50] (which was updated in [46]) is possible due to the overlapping volumes of their galaxy samples being small enough that any correlations can be ignored. We have further reason to combine these, given that the Planck Collaboration [51], in 2015, used

them in addition to BOSS-CMASS [50].

During the journal's reviewing process, more updated BAO measurements were made available. We decided to include these in one of our analyses to be as thorough as possible. The revised set include 6dFGS, SDSS-MGS, BOSS DR12 [46], eBOSS [52] and BOSS-Ly$\alpha$ [47].

Lastly, we highlight that in order to use BAO data from the references [47, 52, 53], a number of assumptions had to be made. Since these data were collected from quasar Lyman $\alpha$ measurements, we assume universality of quasar continuum spectra, modelling of metal-line and high-column-density neutral hydrogen absorbers, as well as spatial fluctuations in the UV ionising flux [54].

Table 3.2: The BAO3 measurements used in this work. We have that $D_M = (1+z)d_A$ and $D_H = 1/H(z)$. For BOSS DR12 and BOSS-Ly$\alpha$, we used the covariance matrices given in their references.

| Survey | $z_{\text{eff}}$ | Reported Parameter | Redshift Sample | $r_d^{\text{fid}}$ [Mpc] | Ref. |
|---|---|---|---|---|---|
| 6dFGS | 0.106 | $d_z^{-1} = 0.3360 \pm 0.0150$ | $0 < z < 0.24$ | $-$ | [49] |
| SDSS MGS | 0.150 | $d_z = (664 \pm 25)/r_d^{\text{fid}}$ | $0 < z < 0.20$ | 148.69 | [48] |
| BOSS DR12 | 0.380 | $D_M \frac{r_d^{\text{fid}}}{r_d} = (1512.39 \pm 24.99)$ | $0.2 < z < 0.75$ | 147.78 | [46] |
| BOSS DR12 | 0.380 | $D_H/r_d = (81.21 \pm 2.37)/r_d^{\text{fid}}$ | $0.2 < z < 0.75$ | 147.78 | [46] |
| BOSS DR12 | 0.510 | $D_M \frac{r_d^{\text{fid}}}{r_d} = (1975.22 \pm 30.10)$ | $0.2 < z < 0.75$ | 147.78 | [46] |
| BOSS DR12 | 0.510 | $D_H/r_d = (90.90 \pm 2.33)/r_d^{\text{fid}}$ | $0.2 < z < 0.75$ | 147.78 | [46] |
| BOSS DR12 | 0.610 | $D_M \frac{r_d^{\text{fid}}}{r_d} = (2306.68 \pm 37.08)$ | $0.2 < z < 0.75$ | 147.78 | [46] |
| BOSS DR12 | 0.610 | $D_H/r_d = (98.96 \pm 2.50)/r_d^{\text{fid}}$ | $0.2 < z < 0.75$ | 147.78 | [46] |
| BOSS Ly$\alpha$ | 2.400 | $D_M/r_d = 36.6 \pm 1.2$ | $2 \leq z \leq 3.50$ | 147.33 | [47] |
| BOSS Ly$\alpha$ | 2.400 | $D_H/r_d = 8.94 \pm 0.22$ | $2 \leq z \leq 3.50$ | 147.33 | [47] |
| eBOSS | 1.520 | $d_z = 26.47 \pm 1.23$ | $0.80 < z < 2.20$ | 147.78 | [52] |

### 3.3.1.2 BAO2

Since we are testing cosmological models, there are a few extra precautions to take since the fiducial model used to extract the BAO signal from galaxy catalogues is usually $\Lambda$CDM [55]. Moreover, not only are the values chosen for the cosmological

parameters arbitrary, but the formula for computing $r_d^{\text{fid}}$ can also differ (authors may use Eq. (3.11) or CAMB [56] formulas), which could bias the results.

A more model independent way to obtain the BAO signature is to use the 2-point angular correlation function (2PACF) analysis, which, if $r_d$ is known, provides $d_A(z)$ almost model-independently. The signal is obtained from narrow redshift bins, of order $0.01 - 0.02$, to ensure that there is no contamination from the radial BAO signal [57]. We rearrange Eq. (3.15) to obtain

$$\theta_{\text{BAO}}(z) = \frac{r_d}{(1+z)d_A(z)} \, , \qquad (3.16)$$

where $\theta_{\text{BAO}}$ is our measurement of BAO2. The procedure for obtaining $\theta_{\text{BAO}}$ from $\theta_{\text{FIT}}$, which is a parametrization of the 2PACF, as a sum of a power law, a constant and a Gaussian peak, is described in [58]. According to the authors, a correction factor is needed, which takes into consideration the size of the redshift shell. To calculate this factor, a fiducial cosmology is required but, as the authors argue, the dependence on the model is minimal, as is confirmed by tests they performed for various cosmologies.

The BAO2 data used in this work were obtained from analyses of the Sloan Digital Sky Survey (SDSS) and are shown in Table 3.3. Since many of the data used for BAO3 were also taken from SDSS, we do not combine these two datasets in our analyses.

The size of the standard ruler, $r_d$, and the sound horizon at the drag epoch coincide in the case of $\Lambda$CDM, but this is not necessarily true for other models [62]. In fact, the $H_0$ tension, for example, between the value measured using CMB data by Planck [15] and the one found with Cepheids [13], could indicate an incompatibility between the standard ruler for the acoustic scale and its value estimated in a model independent way [63, 64]. We therefore take a more conservative approach

Table 3.3: BAO2 measurements from angular separation of pairs of galaxies.

| Survey | $z$ | $\theta_{\mathrm{BAO}}(z)$ [°] | Ref. |
|---|---|---|---|
| SDSS-DR7 | 0.235 | $9.06 \pm 0.23$ | [59] |
| SDSS-DR7 | 0.365 | $6.33 \pm 0.22$ | [59] |
| SDSS-DR10 | 0.450 | $4.77 \pm 0.17$ | [58] |
| SDSS-DR10 | 0.470 | $5.02 \pm 0.25$ | [58] |
| SDSS-DR10 | 0.490 | $4.99 \pm 0.21$ | [58] |
| SDSS-DR10 | 0.510 | $4.81 \pm 0.17$ | [58] |
| SDSS-DR10 | 0.530 | $4.29 \pm 0.30$ | [58] |
| SDSS-DR10 | 0.550 | $4.25 \pm 0.25$ | [58] |
| SDSS-DR11 | 0.570 | $4.59 \pm 0.36$ | [60] |
| SDSS-DR11 | 0.590 | $4.39 \pm 0.33$ | [60] |
| SDSS-DR11 | 0.610 | $3.85 \pm 0.31$ | [60] |
| SDSS-DR11 | 0.630 | $3.90 \pm 0.43$ | [60] |
| SDSS-DR11 | 0.650 | $3.55 \pm 0.16$ | [60] |
| SDSS-DR12Q | 2.225 | $1.85 \pm 0.33$ | [61] |

by considering two different scenarios: the first involves deriving $r_d$ from Eq. (3.11) and taking $z_d = 1059.6$, as reported by [51]; the second is to consider $r_d h$ a free parameter, and to use the value found in [62] as a prior in our analyses.

### 3.3.2 Cosmic Microwave Background

The CMB is the earliest one can go when probing the evolution of the universe. It is composed of photons from the time of the last scattering at $z \sim 1100$. When it was first detected by Penzias and Wilson [65] in 1963, and for almost three decades afterwards, the CMB provided strong evidence for the cosmological principle, as observers saw a smooth background distribution. It was only through data from the COBE satellite in 1992 [66] that the temperature anisotropies of the CMB were first detected, bringing about a new way to constrain cosmological parameters.

One of the relevant ways in which the CMB is used is through the 2-point function of the temperature distribution, which is a 2-dimentional field measured

in terms of its angular coordinates. This implies that we can benefit from an expansion in spherical harmonics, such that the 2-point function is given in terms of the multipole, $\ell$, instead of the wave number $k$ from its Fourier transform, as is commonly done in other cases (which we will see when discussing cosmic shear in further chapters).

The CMB is an excellent laboratory for testing beyond $\Lambda$CDM models as, for example, a dynamic dark sector can affect the expansion history of the universe and hence modify the distance to the last scattering [67]; it can also modify the growth of structure, resulting in a discrepancy between CMB-obtained values for the amplitude of the fluctuations $A_s$ and the late-time measurements of $\sigma_8$ [68]. Despite this, we limit our analyses to the compressed likelihood, derived from Planck 2015 chains [69], which describe the observed power spectrum. This allows us to use data from the early universe without the need for a perturbative analysis of the interacting models, nor the adaptation of Boltzmann codes such as CAMB [56] or CLASS[1] to obtain their anisotropy power spectrum.

The compressed likelihood is composed by $\{R, \ell_a, \Omega_{b0}h^2, n_s\}$, where

$$R = \sqrt{\Omega_m H_0^2} d_A(z_*) \; , \tag{3.17}$$

is the shift parameter [70] and

$$\ell_a = \frac{\pi}{\theta_*} = \frac{\pi(1 + z_*)d_A(z_*)}{r_s(z_*)} \; , \tag{3.18}$$

is the angular scale of the sound horizon at last scattering when $z = z_*$. In our analyses, we fix $\Omega_{b0}h^2 = 0.0226$, in accordance with [71], and we do not include $n_s$ since it does not appear explicitly in our models. Moreover, since the shift parameter $R$ is sensitive to changes in the matter epoch, fixing it would risk

---

[1]lesgourg.github.io/class_public/class.html

biasing our results, hence we disconsider this parameter in our analyses[2]. The only information from the CMB that we use is then $\ell_a = 301.63 \pm 0.15$ [69]. To calculate $z_*$, we employ the fitting formula found in [72],

$$z_* = 1048 \left[ 1 + 0.00124(\Omega_{b0}h^2)^{-0.738} \right] \left[ (1 + g_1(\Omega_{m0}h^2)^{g_2} \right] , \qquad (3.19)$$

with

$$g_1 = \frac{0.0783(\Omega_{b0}h^2)^{-0.238}}{1 + 39.5(\Omega_{b0}h^2)^{0.763}} \quad \text{and} \quad g_2 = \frac{0.560}{1 + 21.1(\Omega_{b0}h^2)^{1.81}} . \qquad (3.20)$$

We find that the expression for Eq. (3.19) is only weakly dependent on $\Omega_{m0}$, as the discrepancy is less than 1% for $0.1 < \Omega_{dm0} < 0.4$ and $0.6 < h < 0.8$ when compared to $z_* = 1089.9$, given in [51]. We study the impact of fixing $z_*$ to the aforementioned value, by comparing with the results obtained when computing it with Eq. (3.19).

### 3.3.3 Cosmic Chronometers

One of the concerns in cosmology is that there is no direct way to obtain the value of the Hubble parameter. For that to be possible, we would have to determine the rate of expansion of the universe in an independent way, then apply the obtained value to test cosmological models.

A proposed way of deriving this rate is through the **differential age method** [73, 74]. This approach uses **Cosmic Chronometers** (CC) to probe the variation of the age of the universe with respect to the redshift. This is done by calculating the relative age of a galaxy, $\Delta t$, separated by redshift $\Delta z$, then taking derivative

---

[2]Given the nature of the dark energy models used here, in [69] we are cautioned against using their compressed likelihood. I therefore ask that the results shown in this chapter be taken with a grain of salt.

$dz/dt$ to find

$$H(z) = -\frac{1}{1+z}\frac{dz}{dt} \ . \tag{3.21}$$

This method is different from most others because it deals with the study of cosmic time through the propagation of light. It is worth mentioning that, while this is a cosmology-independent way of probing the expansion history of the universe, it is not without faults [75]. One of the challenges is first finding a good distribution of galaxies, which we can use to follow the evolution of the age of the universe in a homogeneous way. We also have to trust our galaxy models, since different models can give discrepant ages for the same galaxy.

The data used here is given in Table 3.4, where the majority of the values were taken from the BC03 catalogue [76]. While more data is available in the literature, we limit ourselves to redshift $< 1.2$, since in [77] the authors raise the issue that higher redshifts bring us closer to the redshift at which these galaxies were formed, thus requiring a more detailed stellar formation history, stellar population model, and the inclusion of the progenitor-bias. Furthermore, it was also found in [75] that the expansion of the universe is smooth within this range.

### 3.3.4 Type Ia Supernova

**Supernova** is the term used to describe the collapse of a star, which usually happens towards the end of its life. This phenomenon can be classified into two groups, depending on the presence of hydrogen lines in their spectrum: type I does not contain hydrogen; type II contains hydrogen. By analysing their spectra, we can further divide type I into three groups,

(a) its spectra are dominated by massive elements like calcium, sulphur, silicon, and iron, but is devoid of helium;

(b) there is an abundance of helium;

Table 3.4: Estimated values of $H(z)$ obtained using the differential age method.

| $z$ | $H$ [km/s/Mpc] | Ref. |
|---|---|---|
| 0.0700 | $69.0 \pm 19.6$ | [78] |
| 0.0900 | $69.0 \pm 12.0$ | [79] |
| 0.1200 | $68.6 \pm 26.2$ | [78] |
| 0.1700 | $83.0 \pm 8.0$ | [79] |
| 0.1790 | $75.0 \pm 4.0$ | [77] |
| 0.1990 | $75.0 \pm 5.0$ | [77] |
| 0.2000 | $72.9 \pm 29.6$ | [78] |
| 0.2700 | $77.0 \pm 14.0$ | [79] |
| 0.2800 | $88.8 \pm 36.6$ | [78] |
| 0.3520 | $83.0 \pm 14.0$ | [77] |
| 0.3802 | $83.0 \pm 13.5$ | [80] |
| 0.4000 | $95.0 \pm 17.0$ | [79] |
| 0.4004 | $77.0 \pm 10.2$ | [80] |
| 0.4247 | $87.1 \pm 11.2$ | [80] |
| 0.4497 | $92.8 \pm 12.9$ | [80] |
| 0.4783 | $80.9 \pm 9.0$ | [80] |
| 0.4800 | $97.0 \pm 62.0$ | [81] |
| 0.5930 | $104 \pm 13.0$ | [77] |
| 0.6800 | $92.0 \pm 8.0$ | [77] |
| 0.7810 | $105 \pm 12.0$ | [77] |
| 0.8750 | $125 \pm 17.0$ | [77] |
| 0.8800 | $90 \pm 40.0$ | [81] |
| 0.9000 | $117 \pm 23.0$ | [79] |
| 1.0370 | $154 \pm 20.0$ | [77] |

(c) it has no helium.

Supernovae of the type Ib, Ic and II are common in massive stars, with $M >$ $M_\odot$[3]. As its nuclear fuel burns out, the force of gravity starts to dominate, and its centre begins to collapse. After the explosion, these supernovae usually form either black holes, or neutron stars. For type Ia supernovae (SNeIa), on the other hand, the explosion occurs in binary systems composed of a white dwarf and a companion star, which could be either another white dwarf, or a more massive

---

[3] $M_\odot$ and $L_\odot$ correspond to the solar mass and luminosity, respectively.

star. The carbon-oxygen white dwarf accretes mass from its companion, until it reaches the Chandrasekhar limit, $\sim 1,4 M_{\odot}$, which is the maximum amount of mass it can have before it starts to collapse. This gives rise to a process known as carbon detonation, which is the violent ignition of a thermonuclear fusion inside the star [82]. The explosion that follows is so powerful that its luminosity can reach up to $L = 4 \times 10^{9} L_{\odot}$ [83].

In the universe, to refer to an object as a **standard candle**, it is necessary to know its luminosity, how it evolves, and its dependence on age and/or position. In short, the object needs to be standardisable. Another vital characteristic is that its luminosity has to be high, such that it can be detected over large distances, thus allowing us to probe the universe at a younger age. Our interest in SNeIa is because it checks all of these requirements.

To use SNeIa in our analyses, we need to obtain the distance modulus, which measures the difference between the apparent magnitude, $m$ and the absolute magnitude, $M$. We have

$$m = -2.5 \log_{10}(f/f_x) \; , \tag{3.22}$$

where $f_x = 2,53 \times 10^{-8} \mathrm{W \; m^{-2}}$, and $f$ is the flux of the source. The absolute magnitude, on the other hand, is the apparent magnitude that would have been observed if the source were at 10 parsecs from the observer. For a source with luminosity $L$

$$M = -2.5 \log_{10}(L/L_x) \; , \tag{3.23}$$

with $L_x = 78,7 L_{\odot}$, which is the luminosity for an object with flux $2,53 \times 10^{-8} \mathrm{W \; m^{-2}}$ [83]. We can now obtain the distance modulus,

$$\mu = m - M = 5 \log_{10}\left(\frac{d_L}{1 \mathrm{Mpc}}\right) + 25 \; . \tag{3.24}$$

For SNeIa data, the magnitudes are taken at the peak of the B band.

### 3.3.4.1 Joint Light-curve Analysis

One of the SNeIa datasets used here is the Joint Light-curve Analysis (JLA) [84], which is compilation of 740 SNeIa with redshift up to 1.3.

Obtaining the theoretical value of $\mu$ is slightly more complicated than Eq. (3.24) would lead us to believe. This is because we have to consider nuisance parameters, including those from the light curve fitter. JLA uses the second version of the Spectral Adaptive Light curve Template (SALT2) [85], which adopts a modified version of the Tripp formula [86] to convert the fit parameters into distances. We thus calculate

$$\mu = m_B - M_B - \alpha_{\text{SN}} x_1 + \beta_{\text{SN}} c , \tag{3.25}$$

where the nuisance parameters $M_B$, $\alpha_{\text{SN}}$ $\beta_{\text{SN}}$, are the absolute magnitude of a fiducial supernova with $x_1 = 0$ and $c = 0$, and the coefficients of the luminosity—stretch and luminosity—colour relations, respectively. The values $c$, the colour, and $x_1$, the light-curve shape, are given by the light-curve fit for each supernova. The covariance matrix is

$$\mathbf{C} = \mathbf{D}_{\text{stat}} + \mathbf{C}_{\text{sys}} . \tag{3.26}$$

$\mathbf{C}_{\text{sys}}$ contains all the systematic errors, like coherent flow corrections and host galaxy extinction, and $\mathbf{D}_{\text{stat}}$ is a diagonal matrix associated with the uncertainty in the redshifts,

$$\mathbf{D}_{\text{stat}} = \left( \frac{5\sigma_z}{z \log 10} \right)^2 + \sigma_{\text{lens}}^2 + \sigma_{\text{coh}}^2 . \tag{3.27}$$

The first term in the above equation is related to the peculiar velocities, the second to the variation of magnitudes due to gravitational lensing, and the third accounts for the all the intrinsic variation of magnitudes not already described by the other two terms.

### 3.3.4.2 Pantheon sample

The Pantheon sample [87] consists of 1048 SNeIa ranging from $0.01 < z < 2.3$, where they combine 279 SNeIa discovered by the Pan-STARRS1 (PS1) Medium Deep Survey, with data from: CfA1-CfA4 [88, 89, 90, 91, 92], CSP [93, 94, 95], SNLS [96, 97], SDSS [98, 99], SCP [100], GOODS [101] and CANDELS/CLASH [102, 103, 104]. The data calibration and information about each survey can be found in the cited references.

Similarly to JLA, Pantheon also uses the SALT2 and has a slightly different expression for $\mu$,

$$\mu = m_B - M_B - \alpha_{\mathrm{SN}} x_1 + \beta_{\mathrm{SN}} c - \Delta_M + \Delta_B \ , \tag{3.28}$$

where $M_B$, $\alpha_{\mathrm{SN}}$, $\beta_{\mathrm{SN}}$, $c$, and $x_1$ are the usual parameters, and $\Delta_M$ and $\Delta_B$ are distance corrections based on the host-galaxy mass of the supernova and on predicted biases from simulations, respectively.

The data is calibrated using the BEAMS[4] with Bias Correction (BBC) method, which uses simulations to predict the correct SALT2 fit parameters $\alpha_{\mathrm{SN}}$ and $\beta_{\mathrm{SN}}$, such that they are not included in our analyses [106]. Its covariance matrix is similar to Eq. (3.26), where the distance error for each supernova is

$$\mathbf{D}_{\mathrm{stat}} = \sigma_{\mathrm{N}}^2 + \sigma_{\mathrm{Mass}}^2 + \sigma_{\mu-\mathrm{z}}^2 + \sigma_{\mathrm{lens}}^2 + \sigma_{\mathrm{int}}^2 + \sigma_{\mathrm{Bias}}^2 \ , \tag{3.29}$$

where $\sigma_{\mathrm{N}}^2$ is the photometric error associated with the distance of the supernova, $\sigma_{\mathrm{Mass}}^2$ is the distance uncertainty resulting from the mass step correction, $\sigma_{\mu-\mathrm{z}}^2$ is related to the uncertainty of the peculiar velocity and of the redshift measurement in quadrature, $\sigma_{\mathrm{lens}}^2 = (0.055z)^2$ is the error from the stochastic gravitational lensing, $\sigma_{\mathrm{int}}^2$ is the intrinsic scatter, and, lastly, $\sigma_{\mathrm{Bias}}^2$ is the uncertainty from the

---

[4]BEAMS: Bayesian Estimation Applied to Multiple Species [105]

distance bias correction.

### 3.3.5 Joint analyses

We adopt a multivariate Gaussian likelihood for BAO2, BAO3, CC, CMB and SNeIa, with the $\chi^2$ function,

$$\chi^2_f(\Theta) = \sum_i \left( \frac{f(z_i) - f(z_i, \Theta)}{\sigma_{f_i}} \right)^2 \,, \tag{3.30}$$

where $f(z_i)$ is the measured value for $f$ at redshift $z_i$. The function $f(z_i, \Theta)$ is the theoretical value, assuming a model with parameters $\Theta$ for $\theta_{\mathrm{BAO}}(z)$, $d_z(z)$, $H(z)$, $\ell_a(z_*)$ and $\mu(z)$ for BAO2, BAO3, CC, CMB and SNeIa data, respectively. The summation $i$ is over the chosen datasets for the corresponding observable.

The joint likelihood is given by

$$\mathcal{L}_{\mathrm{joint}} = \mathcal{L}_{\mu(z)} \times \mathcal{L}_{\mathrm{BAO}} \times \mathcal{L}_{H(z)} \times \mathcal{L}_{\ell_a(z_*)} \,, \tag{3.31}$$

with the subscript BAO implying $\theta_{\mathrm{BAO}}(z)$ or $d_z(z)$, depending on the analysis.

## 3.4 Methodology

### 3.4.1 Bayesian inference and model selection

In cosmology, the most common way of obtaining information about the parameters $\Theta$ of our model $\mathcal{M}$ is to use Bayesian inference, which is a statistical method that employs a subjective probability.

Our first step is to choose an a priori probability distribution or, more simply, a **prior**, which can be either informative or objective. All the knowledge and uncertainties we have regarding the parameters, before analysing them, are con-

tained in the informative prior. On the hand, an objective, or noninformative, prior has minimal influence over the a posteriori probability distribution, which is more commonly known as the **posterior**.

Next, we want to obtain the **likelihood** function, which is the joint probability function of the data; this holds the information obtained from the data. Finally, we need the posterior, which contains the important statistical quantities, such as the values of the parameters, the uncertainties, as well as the correlations [107, 108].

Consider the dataset $\mathcal{D}$, which we use to introduce Bayes theorem,

$$P(\Theta|\mathcal{D}, \mathcal{M}) = \frac{P(\mathcal{D}|\Theta, \mathcal{M}) \; P(\Theta|\mathcal{M})}{P(\mathcal{D}|\mathcal{M})} \; , \qquad (3.32)$$

where $P(\Theta|\mathcal{D}, \mathcal{M}) = \mathcal{P}(\Theta|\mathcal{D})$ is the posterior, $P(\mathcal{D}|\Theta, \mathcal{M}) = \mathcal{L}(\Theta)$ is the likelihood and $P(\Theta|\mathcal{M}) = \pi(\Theta)$ is the prior. The **Bayesian evidence** is $P(\mathcal{D}|\mathcal{M}) = \mathcal{E}$, which is a normalising constant,

$$\mathcal{E} = \int \mathcal{L}(\Theta)\pi(\Theta)d\Theta \; , \qquad (3.33)$$

that can be used to compare models. For such, we define the Bayes factor,

$$B_{ij} = \frac{\mathcal{E}_i}{\mathcal{E}_j} \; , \qquad (3.34)$$

that compares models $\mathcal{M}_i$ and $\mathcal{M}_j$. We interpret the value of $\ln B_{ij}$ with Jeffreys' scale [109] that provides an empirical measure of the strength of the evidence of each model. Negative values of $\ln B_{ij}$ favour the reference model, in the denominator, which we take to be the $\Lambda$CDM model. We adopt the scale defined in [110], and shown in Table 3.5, where the values 1, 2.5 and 5 provide weak, moderate, and strong evidence, and correspond to odds of about 3 : 1, 12 : 1 and 150 : 1, respectively.

Table 3.5: The Jeffreys' scale as presented in [110]. In the left column, we show the threshold for the logarithm of the Bayes factor, while the right column explains its interpretation.

| $|\ln B_{ij}|$ | Interpretation |
|:---:|:---:|
| $< 1$ | inconclusive |
| $1.0 - 2.5$ | weak |
| $2.5 - 5.0$ | moderate |
| $> 5$ | strong |

To explore the parameter space, we use `PyMultiNest`, which implements the MULTINEST [111, 112, 113] algorithm in python and uses nested sampling. As a convergence criterion, we set the global log-evidence tolerance to 0.01; to improve the accuracy in the estimation of the evidence, we use 1000 live points. These settings generated about $\mathcal{O}(10^4)$ samples for all posterior distributions.

### 3.4.2 Priors and parameter choices

One of our goals in this work was to assess the impact of different priors and the considered free parameters. This is relevant because we are considering interacting models, whereas most of the fitting formulas and calibration was done for $\Lambda$CDM. Hence, some considerations might lead to biases in our results by favouring the standard model.

As a first approach, we took the redshift at the drag epoch to be $z_* = 1089.90$ and compute $r_d$ from Eq. (3.11) for $z_d = 1059.60$ [51]. We also used the dimensionless Hubble parameter, $h$, with a uniform prior ten times the size of the error of the value reported in [114]. Our second approach involved a Gaussian prior for $r_d h$ and $h$, and the calculation of $z_*$ using Eq. (3.19). For $r_d h$, we used the prior given in [62], and in the case of $h$, we took the value found in [114] (which is equivalent

to using it as data). We summarise these as,

$$\text{Gaussian prior for } \{\gamma_x, \alpha, \beta\}; \ r_d \text{ obtained from Eq. (3.11)}; \ z_*, z_d \text{ fixed} \quad (3.35)$$

$$\text{Gaussian prior for } \{h, \gamma_x, \alpha, \beta, r_d h\}; \ z_* \text{ obtained from Eq. (3.19)} \quad (3.36)$$

The priors for the aforementioned parameters are shown in Table 3.6, where we chose a conservative uniform prior for $\Omega_{m0}$. For the interacting models, we used a Gaussian prior for $\gamma_x$, corresponding to the $1\sigma$ value in [51], while for $\alpha$ and $\beta$ the Gaussian prior is centred at a negative value (see reference [115]), such that the models $\Gamma_a$, $\Gamma_c - \Gamma_e$ of Table 3.1 favoured a scenario where dark energy decays into dark matter when $\rho_{dm}$ and $\rho_x$ are positive defined. This choice was motivated by thermodynamical arguments that predict this behaviour for some interacting models [116].

Finally, since we expected the interacting models to only influence the dynamics of the dark sector more recently, and not the physics of the primordial universe, we fixed the quantities $\Omega_{b0} h^2 = 0.0226$ [71], $\Omega_{\gamma 0} h^2 = 2.469 \times 10^{-5}$ [117], $\Omega_{r0} = \Omega_{\gamma 0} \left(1 + \frac{7}{8} \left(\frac{4}{11}\right)^{\frac{4}{3}} N_{\text{eff}}\right)$, $N_{\text{eff}} = 3.046$ [118].

Table 3.6: Priors used for the free parameters of the studied models. $\mathcal{U}$ denotes flat in the given range and $\mathcal{G}$ is Gaussian with mean equal to its first argument and dispersion equal to its second.

| Parameter | Status | Prior | Ref. |
|---|---|---|---|
| $\Omega_{dm0}$ | Global Parameter | $\mathcal{U}(0, 1)$ | - |
| $h$ | Global Parameter | $\mathcal{U}(0.5584, 0.9064)$ | [114] |
| | | $\mathcal{G}(0.7324, 0.0174)$ | [114] |
| $\gamma_x$ | Variable state parameter | $\mathcal{G}(-0.006, 0.002)$ | [69] |
| $\alpha$ | Interacting models | $\mathcal{G}(-0.001, 0.01)$ | [115] |
| $\beta$ | Interacting models | $\mathcal{G}(-0.001, 0.01)$ | [115] |
| $r_d h$ | Global Parameter | $\mathcal{G}(102.3, 1.6)$ | [62] |

## 3.5 Analysis and Results

We considered the following choices for the models described in Table 3.1: 0, 1, 2, 3, 4 meaning $\gamma_x = 0$, $\beta = 0$, $\alpha = 0$, $\alpha = \beta$, $\alpha \neq \beta$, respectively. If we choose $\gamma_x = 0$ and $\beta = 0$ for model $\Gamma_a$, for example, we refer to it as $\Gamma_{a01}$; for $\alpha \neq \beta$ and $\gamma_x$ free, for model $\Gamma_b$, we have $\Gamma_{b4}$. We do not show the results for $\Gamma_{b02}$ since it reduces to the $\Lambda$CDM scenario. Tables 3.7-3.13 show the constraints for $h, \Omega_{dm0}, \alpha, \beta$ and $\gamma_x$, in addition to the logarithm of the Bayes' factor and its interpretation, where a value ln$B < 1$ favours the $\Lambda$CDM model.

A comprehensive plot for the evidences is shown in Figure 3.1, where we found that BAO3 data seem to favour $\Lambda$CDM more than BAO2 data do. The contour plots as well as the Probability Density Functions (PDFs) for the models $\Gamma_{a02}$ and $\Gamma_{a2}$, can be seen in Figure 3.2 for (3.35) and in Figure 3.3 for (3.36). In the former, we found a tension in the parameters $h$, $\Omega_{dm0}$ and $\beta$, which is only very slightly alleviated when introducing the barotropic index $\gamma_x$ to the analyses. In the latter, while there is a tension for $r_d h$ , it is less pronounced in the aforementioned parameters. This tendency is present in all the other models, hence we do not show them for brevity.

### 3.5.1 Scenario 1

Here we summarise the results using the priors described by 3.35.

There are several important findings to highlight from Table 3.7 and Table 3.8. The first is regarding the strength with which the interacting models are disfavoured against $\Lambda$CDM. The only difference between the two tables is that Table 3.7 uses BAO2 data while Table 3.8 uses BAO3. The models which were weakly disfavoured with BAO2, become moderately so, when considering BAO3. This shows a clear preference for $\Lambda$CDM by BAO3 data.
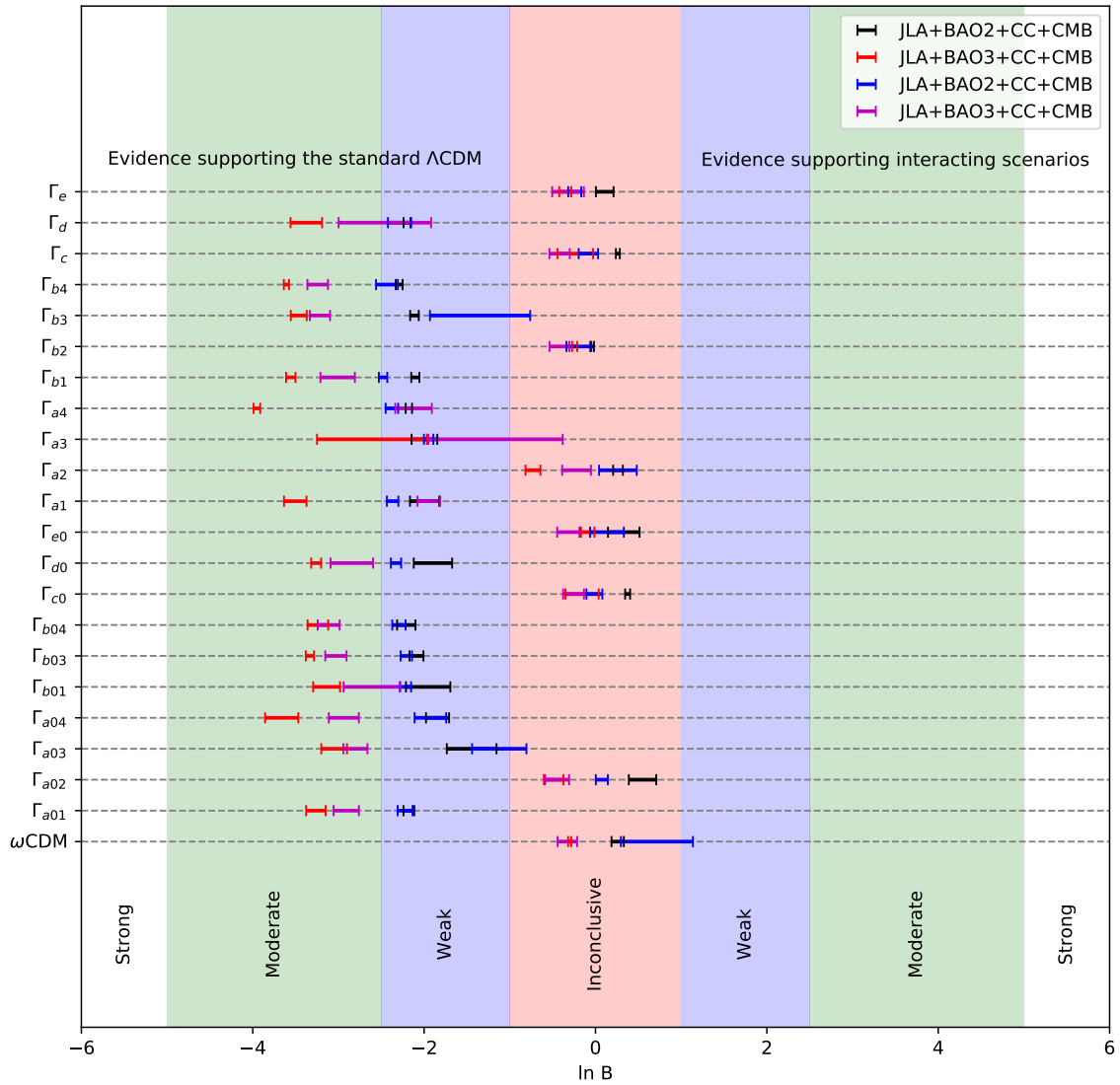
Figure 3.1: Summary of Bayesian comparison between interacting models and ΛCDM. We show the classification in terms of the Jeffreys' scale, where $\ln B < -1$ favours the ΛCDM scenario. The coloured intervals represent the $1\sigma$ region in the estimation of the Bayes' factor. Intervals in black and red consider as priors scenario (3.35) and those in blue and magenta consider as prior scenario (3.36).

The second result we note is in regard to models $\Gamma_{a02}$, $\Gamma_{c0}$, $\Gamma_{e0}$, $\Gamma_{a2}$, $\Gamma_{b2}$, $\Gamma_c$ and $\Gamma_e$, with inconclusive evidence, which is consistent for both BAO2 and BAO3 data. In the analyses shown in Table 3.9 where we replaced the JLA dataset with the Pantheon sample, for BAO2, the results are similar, with the evidence against some of the interacting models increasing from weak to moderate. These models correspond to $\Gamma \propto \rho_x$ or $\Gamma \propto \rho'_x$, with an energy transfer from dark energy to dark matter. Furthermore, $\Gamma_{a10}$, $\Gamma_{a20}$, $\Gamma_{c0}$, $\Gamma_{d0}$ and $\Gamma_{e0}$ were analysed in [119], where the authors used the full CMB temperature anisotropy spectrum, JLA and BAO3, where they found that models with $\Gamma \propto \rho_m$ were virtually discarded. This was not necessarily true, however, for $\Gamma \propto \rho_x$.

The constraints for $h$ seem to suggest that BAO data may be a useful ingredient to the $H_0$ tension [120], since we found higher values of $h$ for BAO2 when compared to BAO3. Finally, the values of the fitted barotropic index and the interacting parameters are about an order of magnitude higher for BAO2, which is another hint of the preference for $\Lambda$CDM by BAO3 data.

### 3.5.2 Scenario 2

Here we summarise the results using the priors described by 3.36.

The conclusions drawn from model comparison are the same as in the previous sections, with inconclusive evidence for the models $\Gamma_{a02}$, $\Gamma_{c0}$, $\Gamma_{e0}$, $\Gamma_{a2}$, $\Gamma_{b2}$, $\Gamma_c$ and $\Gamma_e$. When considering the analyses with BAO2, in Table 3.10, the disfavoured models are only weakly so, but they do not all become moderately disfavoured with BAO3 data, seen in Table 3.11, as was the case in Scenario 1. While this is still true for most cases, it is not as evident that BAO3 is biasing the results to $\Lambda$CDM; the results using the Pantheon sample with BAO3 data, shown in Table 3.12, are analogous to these.

As expected, the values for $h$ and $r_d h$ closely follow their prior. We did not

note any particular trends for the values of $\alpha$, $\beta$ or $\gamma_x$ regarding the choice of observables and different scenarios.

Finally, in Table 3.13, we show the results for the joint analyses with the Pantheon compilation, CC, CMB and the updated set of BAO3 data. The parameter constraints are compatible with those in Table 3.12, however, the weak evidence in support of $\Lambda$CDM becomes moderate, which is similar to what we observe for the comparison between the evidences in Table 3.7 and Table 3.7. These results seem to suggest that the model dependency of BAO3 could be related to the calculation of $r_d$ from Eq. (3.11).

### 3.5.3 Remarks regarding external analyses

Some of the models we have studied here were also analysed and compared against $\Lambda$CDM in [115]. The authors performed a joint analysis with Union2.1 + BAO3 + H(z) + CMB, and compared the models using the Akaike and Bayesian information criteria (AIC and BIC, respectively). They reported that the strong evidence against some of the interacting models became moderate when swapping the Union2.1 sample for binned JLA data.

The $\Gamma_{a01}$ model was considered in the work done in [121], for a joint analysis with JLA data and a slightly different BAO3 measurements. While we found moderate evidence against this model, in comparison with $\Lambda$CDM, their results showed a moderate evidence in favour of $\Gamma_{a01}$. One of the major differences between our analyses and theirs is that we considered CMB data and more up-to-date measurements of BAO2 and BAO3 with higher redshift. Moreover, they included data from WiggleZ, which was not used in our work. Finally, they used Eisenstein's approximation for computing the redshift at the drag epoch, whereas our Scenario 1 uses the Planck 2015 value, and Scenario 2 has $r_d h$ as a free parameter.

### 3.5.4 Final remarks

One of our goals in this work was to use cosmological data to explore the viability of different classes of interacting models. We proposed twenty-one different models, six of which corresponded to a nonlinear interaction and fifteen to a linear one. The data seemed to prefer the nonlinear scenarios, as only two of them were rejected with weak or moderate evidence, as compared to twelve models with a linear interaction, which were discarded with weak or moderate evidence.

We also investigated the impact of using the usual BAO3 measurements as compared to the almost model independent BAO2 data. We discovered that the strength of the evidence disfavouring the interacting models is lessened when employing BAO2. This was anticipated since BAO3 data use $\Lambda$CDM as fiducial model. Our findings with regard to scenarios (3.35) and (3.36) seem to indicate that this model-dependency is partially embedded in the computation of $r_d$.
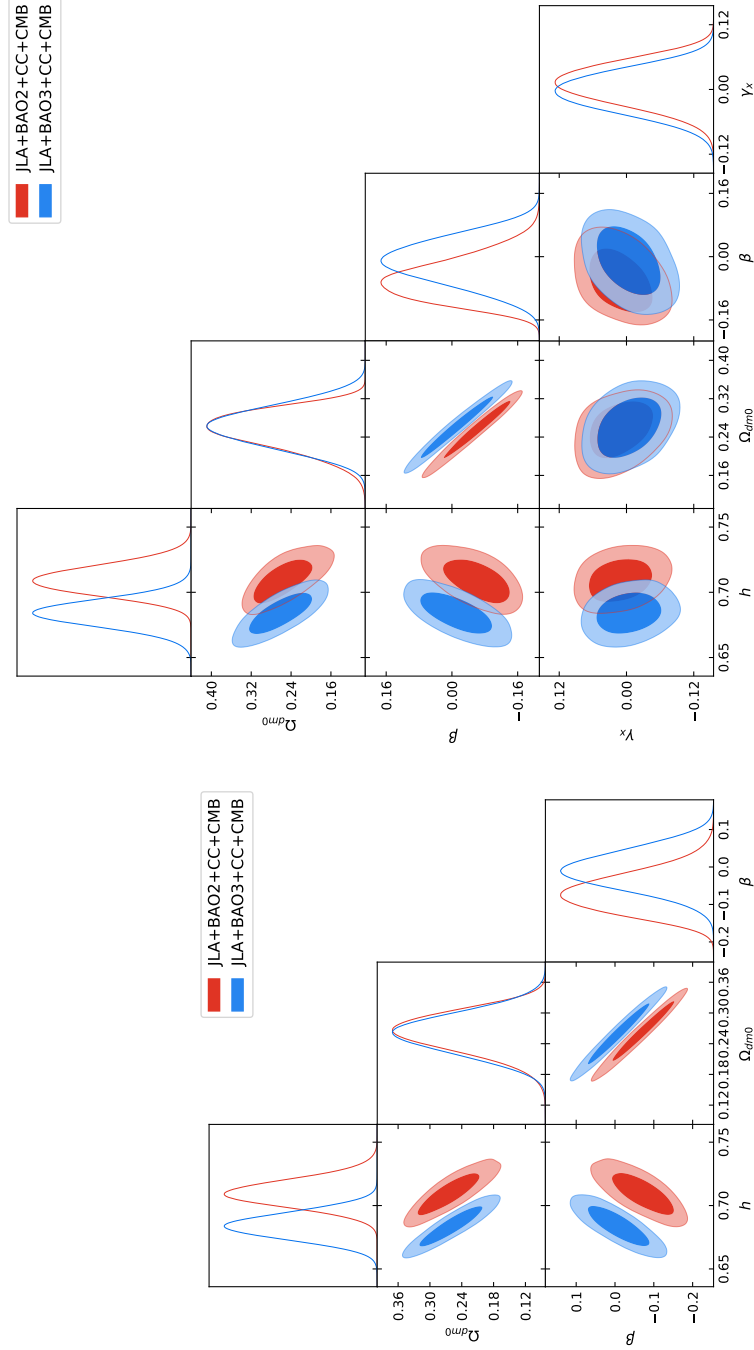
Figure 3.2: Example of contour plots and PDFs (models $\Gamma_{a02}$ and $\Gamma_{a2}$ at top and bottom, respectively). The results consider as priors scenario (3.35).
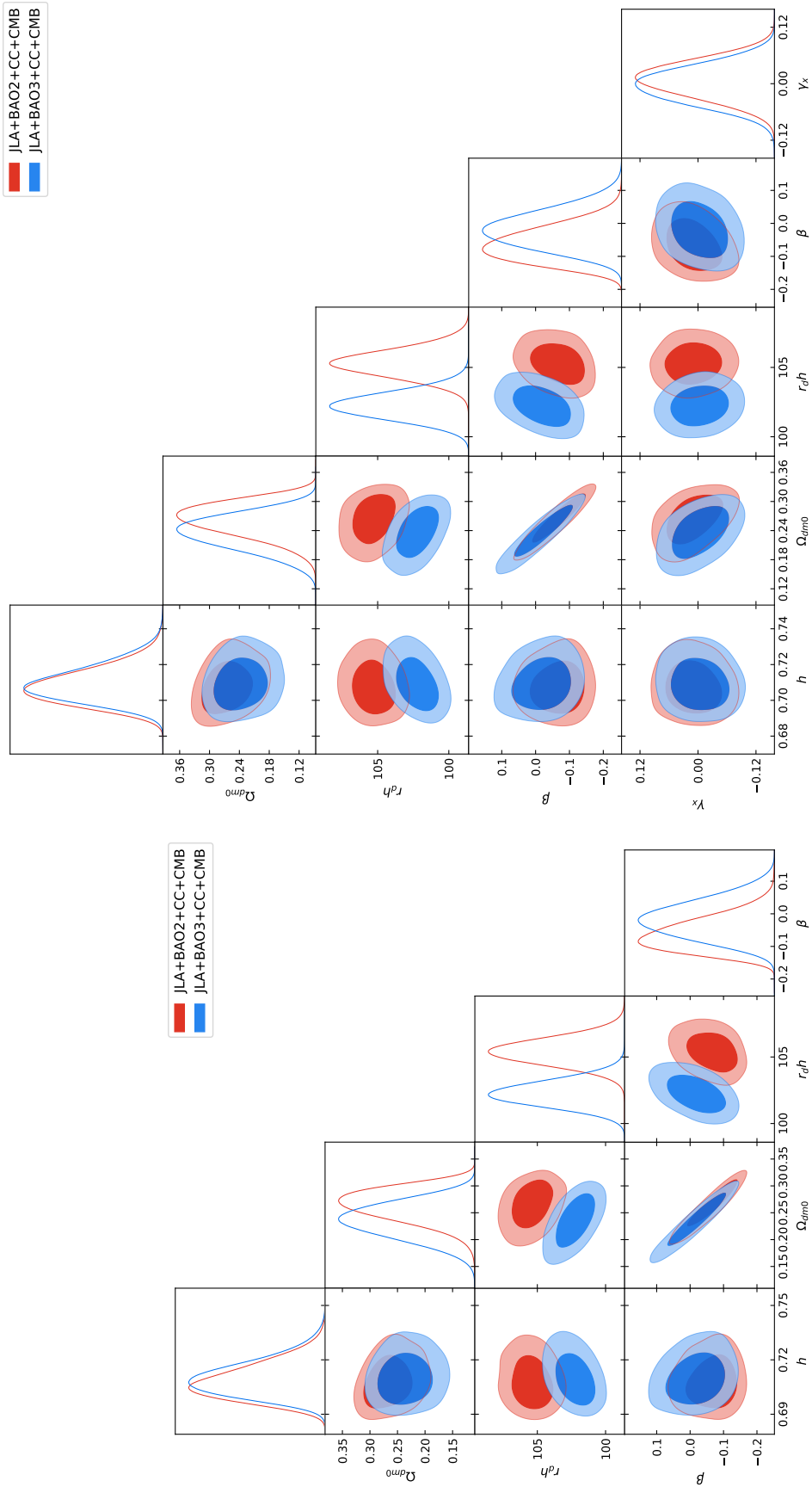
Figure 3.3: Example of contour plots and PDFs (models $\Gamma_{a02}$ and $\Gamma_{a2}$ at top and bottom, respectively). The results consider as priors scenario (3.36).

Table 3.7: Best fit parameters for the joint analysis JLA + BAO2 + CC + CMB. The last two columns show the Bayes factor ($\ln B$) and the interpretation of the strength of the evidence. Note that $\ln B < -1$ favours the $\Lambda$CDM model. These results consider as priors scenario (3.35).

| Model | $h$ | $\Omega_{dm0}$ | $\alpha$ | $\beta$ | $\gamma_x$ | $\ln B$ | Interpretation |
|---|---|---|---|---|---|---|---|
| $\Lambda$CDM | $0.720 \pm 0.008$ | $0.2127^{+0.0078}_{-0.0088}$ | - | - | - | - | |
| $\Gamma_{a01}$ | $0.693 \pm 0.020$ | $0.2166^{+0.0084}_{-0.0094}$ | $-0.0077^{+0.0065}_{-0.0045}$ | - | - | $-2.178 \pm 0.063$ | Weak |
| $\Gamma_{a02}$ | $0.710 \pm 0.011$ | $0.262^{+0.041}_{-0.034}$ | - | $-0.069^{+0.047}_{-0.057}$ | - | $0.549 \pm 0.160$ | Inconclusive |
| $\Gamma_{a03}$ | $0.691 \pm 0.021$ | $0.222^{+0.010}_{-0.012}$ | $-0.0079^{+0.0064}_{-0.0047}$ | $-0.0079^{+0.0064}_{-0.0047}$ | - | $-1.445 \pm 0.290$ | Weak |
| $\Gamma_{a04}$ | $0.687 \pm 0.020$ | $0.259^{+0.042}_{-0.034}$ | $-0.0065^{+0.0061}_{-0.0041}$ | $-0.060^{+0.048}_{-0.058}$ | - | $-1.843 \pm 0.135$ | Weak |
| $\Gamma_{b01}$ | $0.692 \pm 0.021$ | $0.2167^{+0.0084}_{-0.0096}$ | $0.0079^{+0.0047}_{-0.0068}$ | - | - | $-1.953 \pm 0.259$ | Weak |
| $\Gamma_{b03}$ | $0.693 \pm 0.021$ | $0.2165^{+0.0085}_{-0.0098}$ | $0.0078^{+0.0046}_{-0.0065}$ | $0.0078^{+0.0046}_{-0.0065}$ | - | $-2.089 \pm 0.081$ | Weak |
| $\Gamma_{b04}$ | $0.693 \pm 0.021$ | $0.2165^{+0.0086}_{-0.0096}$ | $0.0078^{+0.0046}_{-0.0071}$ | $-0.012 \pm 0.097$ | - | $-2.208 \pm 0.107$ | Weak |
| $\Gamma_{c0}$ | $0.7134 \pm 0.0099$ | $0.237 \pm 0.024$ | $-0.075^{+0.057}_{-0.079}$ | - | - | $0.375 \pm 0.029$ | Inconclusive |
| $\Gamma_{d0}$ | $0.694 \pm 0.021$ | $0.2142^{+0.0081}_{-0.0091}$ | $-0.0076^{+0.0068}_{-0.0047}$ | - | - | $-1.897 \pm 0.224$ | Weak |
| $\Gamma_{e0}$ | $0.7173 \pm 0.0086$ | $0.232^{+0.033}_{-0.024}$ | $-0.048^{+0.059}_{-0.075}$ | - | - | $0.330 \pm 0.184$ | Inconclusive |
| $\Gamma_{a1}$ | $0.690 \pm 0.021$ | $0.2159^{+0.0084}_{-0.0094}$ | $-0.0076^{+0.0066}_{-0.0046}$ | - | $0.023^{+0.039}_{-0.032}$ | $-1.994 \pm 0.171$ | Weak |
| $\Gamma_{a2}$ | $0.710 \pm 0.011$ | $0.255^{+0.045}_{-0.032}$ | - | $-0.059^{+0.044}_{-0.062}$ | $0.011^{+0.040}_{-0.036}$ | $0.263 \pm 0.057$ | Inconclusive |
| $\Gamma_{a3}$ | $0.689 \pm 0.021$ | $0.2214^{+0.0098}_{-0.012}$ | $-0.0075^{+0.0063}_{-0.0046}$ | $-0.0075^{+0.0063}_{-0.0046}$ | $0.020^{+0.038}_{-0.031}$ | $-1.996 \pm 0.150$ | Weak |
| $\Gamma_{a4}$ | $0.688 \pm 0.020$ | $0.252^{+0.045}_{-0.038}$ | $-0.0064^{+0.0060}_{-0.0042}$ | $-0.051^{+0.053}_{-0.061}$ | $0.011 \pm 0.039$ | $-2.178 \pm 0.037$ | Weak |
| $\Gamma_{b1}$ | $0.691 \pm 0.021$ | $0.2159 \pm 0.0090$ | $0.0074^{+0.0046}_{-0.0066}$ | - | $0.024^{+0.039}_{-0.033}$ | $-2.103 \pm 0.047$ | Weak |
| $\Gamma_{b2}$ | $0.7164 \pm 0.0089$ | $0.2124 \pm 0.0085$ | - | $0.000 \pm 0.095$ | $0.025^{+0.037}_{-0.029}$ | $-0.039 \pm 0.021$ | Inconclusive |
| $\Gamma_{b3}$ | $0.691 \pm 0.021$ | $0.2160^{+0.0084}_{-0.0097}$ | $0.0074^{+0.0047}_{-0.0064}$ | $0.0074^{+0.0047}_{-0.0064}$ | $0.023^{+0.039}_{-0.031}$ | $-2.113 \pm 0.050$ | Weak |
| $\Gamma_{b4}$ | $0.690 \pm 0.020$ | $0.2159 \pm 0.0093$ | $0.0075^{+0.0045}_{-0.0065}$ | $-0.007 \pm 0.094$ | $0.024^{+0.038}_{-0.032}$ | $-2.291 \pm 0.040$ | Weak |
| $\Gamma_c$ | $0.711 \pm 0.010$ | $0.233^{+0.026}_{-0.023}$ | $-0.065^{+0.057}_{-0.082}$ | - | $0.019^{+0.038}_{-0.032}$ | $0.261 \pm 0.023$ | Inconclusive |
| $\Gamma_d$ | $0.692 \pm 0.020$ | $0.2134^{+0.0080}_{-0.0089}$ | $-0.0073^{+0.0065}_{-0.0046}$ | - | $0.024^{+0.038}_{-0.031}$ | $-2.196 \pm 0.044$ | Weak |
| $\Gamma_e$ | $0.7143 \pm 0.0094$ | $0.227^{+0.034}_{-0.023}$ | $-0.036^{+0.056}_{-0.076}$ | - | $0.024^{+0.039}_{-0.031}$ | $0.108 \pm 0.103$ | Inconclusive |

Table 3.8: Best fit parameters for the joint analysis JLA + BAO3 + CC + CMB. The last two columns show the Bayes factor ($\ln B$) and the interpretation of the strength of the evidence. Note that $\ln B < -1$ favours the $\Lambda$CDM model. These results consider as priors scenario (3.35).

| Model | $h$ | $\Omega_{dm0}$ | $\alpha$ | $\beta$ | $\gamma_x$ | $\ln B$ | Interpretation |
|---|---|---|---|---|---|---|---|
| $\Lambda$CDM | $0.6853 \pm 0.0061$ | $0.2537 \pm 0.0080$ | - | - | - | - | |
| $\Gamma_{a01}$ | $0.684 \pm 0.020$ | $0.2543 \pm 0.0088$ | $-0.0005^{+0.0044}_{-0.0035}$ | - | - | $-3.263 \pm 0.114$ | Moderate |
| $\Gamma_{a02}$ | $0.684 \pm 0.010$ | $0.259 \pm 0.038$ | - | $-0.008 \pm 0.052$ | - | $-0.488 \pm 0.114$ | Inconclusive |
| $\Gamma_{a03}$ | $0.684 \pm 0.020$ | $0.255 \pm 0.010$ | $-0.0005^{+0.0044}_{-0.0035}$ | $-0.0005^{+0.0044}_{-0.0035}$ | - | $-3.050 \pm 0.150$ | Moderate |
| $\Gamma_{a04}$ | $0.683 \pm 0.020$ | $0.256 \pm 0.039$ | $-0.0006^{+0.0045}_{-0.0034}$ | $-0.003 \pm 0.053$ | - | $-3.662 \pm 0.194$ | Moderate |
| $\Gamma_{b01}$ | $0.684 \pm 0.020$ | $0.2543 \pm 0.0090$ | $0.0006^{+0.0035}_{-0.0045}$ | - | - | $-3.138 \pm 0.157$ | Moderate |
| $\Gamma_{b03}$ | $0.684 \pm 0.019$ | $0.2542^{+0.0083}_{-0.0094}$ | $0.0005^{+0.0034}_{-0.0043}$ | $0.0005^{+0.0034}_{-0.0043}$ | - | $-3.333 \pm 0.048$ | Moderate |
| $\Gamma_{b04}$ | $0.684 \pm 0.019$ | $0.2542 \pm 0.0087$ | $0.0005^{+0.0034}_{-0.0043}$ | $-0.011 \pm 0.098$ | - | $-3.240 \pm 0.120$ | Moderate |
| $\Gamma_{c0}$ | $0.6839 \pm 0.0091$ | $0.258 \pm 0.025$ | $-0.011 \pm 0.068$ | - | - | $-0.157 \pm 0.194$ | Inconclusive |
| $\Gamma_{d0}$ | $0.684 \pm 0.020$ | $0.2542 \pm 0.0086$ | $-0.0007^{+0.0046}_{-0.0035}$ | - | - | $-3.260 \pm 0.058$ | Moderate |
| $\Gamma_{e0}$ | $0.6852 \pm 0.0075$ | $0.254^{+0.032}_{-0.027}$ | $-0.002 \pm 0.072$ | - | - | $-0.091 \pm 0.078$ | Inconclusive |
| $\Gamma_{a1}$ | $0.684 \pm 0.020$ | $0.2544 \pm 0.0088$ | $-0.0006^{+0.0044}_{-0.0035}$ | - | $0.000 \pm 0.035$ | $-3.504 \pm 0.131$ | Moderate |
| $\Gamma_{a2}$ | $0.684 \pm 0.010$ | $0.261 \pm 0.041$ | - | $-0.011 \pm 0.056$ | $-0.004 \pm 0.037$ | $-0.730 \pm 0.087$ | Inconclusive |
| $\Gamma_{a3}$ | $0.684 \pm 0.020$ | $0.2547^{+0.0095}_{-0.011}$ | $-0.0005^{+0.0044}_{-0.0034}$ | $-0.0005^{+0.0044}_{-0.0034}$ | $0.001 \pm 0.036$ | $-2.608 \pm 0.642$ | Moderate |
| $\Gamma_{a4}$ | $0.683 \pm 0.020$ | $0.256^{+0.044}_{-0.039}$ | $-0.0006^{+0.0045}_{-0.0033}$ | $-0.004 \pm 0.057$ | $-0.002 \pm 0.038$ | $-3.952 \pm 0.039$ | Moderate |
| $\Gamma_{b1}$ | $0.683 \pm 0.020$ | $0.2545 \pm 0.0088$ | $0.0006^{+0.0034}_{-0.0045}$ | - | $0.001 \pm 0.035$ | $-3.556 \pm 0.055$ | Moderate |
| $\Gamma_{b2}$ | $0.6853 \pm 0.0080$ | $0.2539 \pm 0.0082$ | - | $-0.005 \pm 0.093$ | $-0.001 \pm 0.034$ | $-0.243 \pm 0.030$ | Inconclusive |
| $\Gamma_{b3}$ | $0.684 \pm 0.020$ | $0.2542 \pm 0.0089$ | $0.0005^{+0.0034}_{-0.0044}$ | $0.0005^{+0.0034}_{-0.0044}$ | $0.000 \pm 0.036$ | $-3.463 \pm 0.093$ | Moderate |
| $\Gamma_{b4}$ | $0.684 \pm 0.020$ | $0.2543 \pm 0.0092$ | $0.0007^{+0.0035}_{-0.0045}$ | $-0.016 \pm 0.094$ | $0.000 \pm 0.036$ | $-3.607 \pm 0.030$ | Moderate |
| $\Gamma_{c}$ | $0.6844 \pm 0.0097$ | $0.258 \pm 0.026$ | $-0.011 \pm 0.072$ | - | $-0.002 \pm 0.036$ | $-0.236 \pm 0.208$ | Inconclusive |
| $\Gamma_{d}$ | $0.684 \pm 0.020$ | $0.2543 \pm 0.0084$ | $-0.0006^{+0.0045}_{-0.0035}$ | - | $0.000 \pm 0.036$ | $-3.375 \pm 0.184$ | Moderate |
| $\Gamma_{e}$ | $0.6851 \pm 0.0086$ | $0.254^{+0.031}_{-0.026}$ | $-0.004 \pm 0.069$ | - | $0.000 \pm 0.035$ | $-0.353 \pm 0.070$ | Inconclusive |

Table 3.9: Best fit parameters for the joint analysis Pantheon + BAO2 + CC + CMB. The last two columns show the Bayes factor ($\ln B$) and the interpretation of the strength of the evidence. Note that $\ln B < -1$ favours the $\Lambda$CDM model. These results consider as priors scenario (3.35).

| Model | $h$ | $\Omega_{dm0}$ | $r_d h$ [Mpc] | $\alpha$ | $\beta$ | $\gamma_x$ | $\ln B$ | Interpretation |
|---|---|---|---|---|---|---|---|---|
| $\Lambda$CDM | $0.6991^{+0.0091}_{-0.011}$ | $0.238 \pm 0.012$ | $105.6 \pm 1.1$ | - | - | - | - | - |
| $\Gamma_{a01}$ | $0.710^{+0.010}_{-0.013}$ | $0.257 \pm 0.018$ | $105.3 \pm 1.0$ | $0.0046^{+0.0037}_{-0.0020}$ | - | - | $-2.469 \pm 0.226$ | Weak |
| $\Gamma_{a02}$ | $0.7055^{+0.0077}_{-0.011}$ | $0.264^{+0.031}_{-0.026}$ | $105.4 \pm 1.0$ | - | $-0.057^{+0.050}_{-0.057}$ | - | $-0.284 \pm 0.227$ | Inconclusive |
| $\Gamma_{a03}$ | $0.710 \pm 0.012$ | $0.261^{+0.013}_{-0.026}$ | $105.2 \pm 1.1$ | $-0.0069^{+0.016}_{-0.0089}$ | $-0.0079^{+0.0064}_{-0.0047}$ | - | $-2.141 \pm 0.228$ | Weak |
| $\Gamma_{a04}$ | $0.7105^{+0.0091}_{-0.012}$ | $0.256 \pm 0.030$ | $105.3 \pm 1.0$ | $0.00297^{+0.0060}_{-0.00054}$ | $0.006^{+0.069}_{-0.078}$ | - | $-2.625 \pm 0.229$ | Moderate |
| $\Gamma_{b01}$ | $0.7116^{+0.0092}_{-0.012}$ | $0.257 \pm 0.018$ | $105.3 \pm 1.1$ | $-0.0052^{+0.0024}_{-0.0031}$ | - | - | $-2.379 \pm 0.241$ | Weak |
| $\Gamma_{b03}$ | $0.711^{+0.010}_{-0.012}$ | $0.258 \pm 0.018$ | $105.3 \pm 1.1$ | $-0.0001^{+0.0026}_{-0.0083}$ | $-0.0001^{+0.0026}_{-0.0083}$ | - | $-2.365 \pm 0.233$ | Weak |
| $\Gamma_{b04}$ | $0.7110^{+0.0094}_{-0.012}$ | $0.256^{+0.016}_{-0.018}$ | $105.3 \pm 1.1$ | $-0.0052 \pm 0.0029$ | $-0.012 \pm 0.092$ | - | $-1.471 \pm 0.651$ | Weak |
| $\Gamma_{c0}$ | $0.7032^{+0.0066}_{-0.010}$ | $0.246 \pm 0.017$ | $105.5 \pm 1.0$ | $-0.055^{+0.061}_{-0.081}$ | - | - | $-0.118 \pm 0.284$ | Inconclusive |
| $\Gamma_{d0}$ | $0.7112^{+0.0094}_{-0.012}$ | $0.257 \pm 0.018$ | $105.3 \pm 1.0$ | $0.0051^{+0.0031}_{-0.0024}$ | - | - | $-2.418 \pm 0.230$ | Weak |
| $\Gamma_{e0}$ | $0.7024^{+0.0074}_{-0.011}$ | $0.251^{+0.026}_{-0.022}$ | $105.5 \pm 1.0$ | $-0.049^{+0.070}_{-0.079}$ | - | - | $-0.272 \pm 0.228$ | Inconclusive |
| $\Gamma_{a1}$ | $0.7116^{+0.0093}_{-0.012}$ | $0.257 \pm 0.022$ | $105.2 \pm 1.0$ | $0.00320^{+0.0053}_{-0.00040}$ | - | $-0.003 \pm 0.039$ | $-2.518 \pm 0.231$ | Moderate |
| $\Gamma_{a2}$ | $0.7044^{+0.0085}_{-0.011}$ | $0.262^{+0.035}_{-0.029}$ | $105.4 \pm 1.0$ | - | $-0.055^{+0.049}_{-0.059}$ | $0.005^{+0.040}_{-0.036}$ | $-0.399 \pm 0.228$ | Inconclusive |
| $\Gamma_{a3}$ | $0.710^{+0.010}_{-0.012}$ | $0.258^{+0.021}_{-0.025}$ | $105.3 \pm 1.0$ | $0.0001^{+0.0084}_{-0.0024}$ | $0.0001^{+0.0084}_{-0.0024}$ | $-0.003 \pm 0.041$ | $-2.283 \pm 0.254$ | Weak |
| $\Gamma_{a4}$ | $0.7113^{+0.0095}_{-0.012}$ | $0.256 \pm 0.033$ | $105.3 \pm 1.0$ | $0.0055^{+0.0037}_{-0.0029}$ | $0.008 \pm 0.070$ | $-0.004 \pm 0.040$ | $-2.511 \pm 0.267$ | Moderate |
| $\Gamma_{b1}$ | $0.7116^{+0.0090}_{-0.012}$ | $0.257 \pm 0.022$ | $105.3 \pm 1.0$ | $-0.0053^{+0.0024}_{-0.0032}$ | - | $-0.002 \pm 0.039$ | $-2.579 \pm 0.226$ | Moderate |
| $\Gamma_{b2}$ | $0.7017^{+0.0074}_{-0.010}$ | $0.232^{+0.015}_{-0.013}$ | $105.57 \pm 0.99$ | - | $0.000 \pm 0.092$ | $0.016 \pm 0.034$ | $-0.420 \pm 0.228$ | Inconclusive |
| $\Gamma_{b3}$ | $0.7103^{+0.0090}_{-0.012}$ | $0.257 \pm 0.022$ | $105.3 \pm 1.0$ | $-0.0050^{+0.0025}_{-0.0033}$ | $-0.0050^{+0.0025}_{-0.0033}$ | $-0.004 \pm 0.040$ | $-2.428 \pm 0.262$ | Weak |
| $\Gamma_{b4}$ | $0.7124^{+0.0075}_{-0.012}$ | $0.257 \pm 0.022$ | $105.3 \pm 1.0$ | $-0.0054^{+0.0026}_{-0.0030}$ | $-0.016 \pm 0.093$ | $-0.003 \pm 0.038$ | $-2.723 \pm 0.226$ | Moderate |
| $\Gamma_{c}$ | $0.7038^{+0.0071}_{-0.0098}$ | $0.241 \pm 0.020$ | $105.5 \pm 1.0$ | $-0.049^{+0.066}_{-0.079}$ | - | $0.015^{+0.040}_{-0.035}$ | $-0.259 \pm 0.256$ | Inconclusive |
| $\Gamma_{d}$ | $0.7112^{+0.0088}_{-0.012}$ | $0.257 \pm 0.023$ | $105.3 \pm 1.1$ | $0.0050^{+0.0032}_{-0.0023}$ | - | $-0.003 \pm 0.042$ | $-2.510 \pm 0.235$ | Moderate |
| $\Gamma_{e}$ | $0.7034^{+0.0072}_{-0.010}$ | $0.243^{+0.030}_{-0.021}$ | $105.6 \pm 1.0$ | $-0.038^{+0.058}_{-0.077}$ | - | $0.013^{+0.041}_{-0.036}$ | $-0.483 \pm 0.228$ | Inconclusive |

Table 3.10: Best fit parameters for the joint analysis JLA + BAO2 + CC + CMB. The last two columns show the Bayes factor ($\ln B$) and the interpretation of the strength of the evidence. Note that $\ln B < -1$ favours the $\Lambda$CDM model. These results consider as priors scenario (3.36).

| Model | $h$ | $\Omega_{dm0}$ | $r_d h$ [Mpc] | $\alpha$ | $\beta$ | $\gamma_x$ | $\ln B$ | Interpretation |
|---|---|---|---|---|---|---|---|---|
| $\Lambda$CDM | $0.7054^{+0.0072}_{-0.012}$ | $0.231^{+0.014}_{-0.0092}$ | $105.73 \pm 0.98$ | - | - | - | - | |
| $\Gamma_{a01}$ | $0.7104^{+0.0094}_{-0.013}$ | $0.258 \pm 0.024$ | $105.2 \pm 1.1$ | $0.0051^{+0.0038}_{-0.0026}$ | - | - | $-2.222 \pm 0.087$ | Weak |
| $\Gamma_{a02}$ | $0.7079^{+0.0079}_{-0.012}$ | $0.265^{+0.034}_{-0.025}$ | $105.4 \pm 1.0$ | - | $-0.064^{+0.041}_{-0.059}$ | - | $0.074 \pm 0.070$ | Inconclusive |
| $\Gamma_{a03}$ | $0.7091^{+0.0096}_{-0.012}$ | $0.286 \pm 0.042$ | $105.1 \pm 1.1$ | $-0.052^{+0.063}_{-0.091}$ | $-0.052^{+0.063}_{-0.091}$ | - | $-1.123 \pm 0.317$ | Weak |
| $\Gamma_{a04}$ | $0.709^{+0.011}_{-0.013}$ | $0.266 \pm 0.034$ | $105.1 \pm 1.1$ | $0.0030^{+0.0061}_{-0.0016}$ | $-0.015^{+0.066}_{-0.084}$ | - | $-1.927 \pm 0.184$ | Weak |
| $\Gamma_{b01}$ | $0.709^{+0.010}_{-0.013}$ | $0.259 \pm 0.023$ | $105.2 \pm 1.1$ | $-0.0050^{+0.0025}_{-0.0037}$ | - | - | $-2.217 \pm 0.065$ | Weak |
| $\Gamma_{b03}$ | $0.7103^{+0.0092}_{-0.013}$ | $0.258 \pm 0.023$ | $105.2 \pm 1.1$ | $-0.0051^{+0.0026}_{-0.0038}$ | $-0.0051^{+0.0026}_{-0.0038}$ | - | $-2.208 \pm 0.066$ | Weak |
| $\Gamma_{b04}$ | $0.7102^{+0.0090}_{-0.013}$ | $0.260 \pm 0.022$ | $105.2 \pm 1.1$ | $-0.0053^{+0.0027}_{-0.0035}$ | $-0.012 \pm 0.095$ | - | $-2.294 \pm 0.078$ | Weak |
| $\Gamma_{c0}$ | $0.7065^{+0.0074}_{-0.011}$ | $0.242 \pm 0.019$ | $105.59 \pm 0.99$ | $-0.054^{+0.062}_{-0.083}$ | - | - | $-0.013 \pm 0.093$ | Inconclusive |
| $\Gamma_{d0}$ | $0.7104^{+0.0095}_{-0.013}$ | $0.259 \pm 0.024$ | $105.2 \pm 1.1$ | $0.0051^{+0.0035}_{-0.0026}$ | - | - | $-2.328 \pm 0.060$ | Weak |
| $\Gamma_{e0}$ | $0.7066^{+0.0078}_{-0.011}$ | $0.248^{+0.028}_{-0.021}$ | $105.57 \pm 0.98$ | $-0.055^{+0.055}_{-0.078}$ | - | - | $0.134 \pm 0.197$ | Inconclusive |
| $\Gamma_{a1}$ | $0.7097^{+0.0099}_{-0.012}$ | $0.258 \pm 0.027$ | $105.2 \pm 1.1$ | $0.0050^{+0.0038}_{-0.0026}$ | - | $0.004 \pm 0.040$ | $-2.368 \pm 0.067$ | Weak |
| $\Gamma_{a2}$ | $0.7077^{+0.0085}_{-0.011}$ | $0.264^{+0.039}_{-0.029}$ | $105.3 \pm 1.0$ | - | $-0.065^{+0.046}_{-0.060}$ | $0.0096 \pm 0.038$ | $0.262 \pm 0.220$ | Inconclusive |
| $\Gamma_{a3}$ | $0.709^{+0.010}_{-0.012}$ | $0.273^{+0.028}_{-0.045}$ | $105.1 \pm 1.0$ | $-0.034^{+0.045}_{-0.032}$ | $-0.034^{+0.045}_{-0.032}$ | $0.005 \pm 0.040$ | $-1.947 \pm 0.055$ | Weak |
| $\Gamma_{a4}$ | $0.709^{+0.010}_{-0.012}$ | $0.264 \pm 0.037$ | $105.1 \pm 1.0$ | $0.0041^{+0.0050}_{-0.0029}$ | $-0.014^{+0.068}_{-0.082}$ | $0.003 \pm 0.041$ | $-2.376 \pm 0.073$ | Weak |
| $\Gamma_{b1}$ | $0.7099^{+0.0098}_{-0.013}$ | $0.257 \pm 0.028$ | $105.2 \pm 1.0$ | $-0.0049^{+0.0025}_{-0.0041}$ | - | $0.004 \pm 0.042$ | $-2.479 \pm 0.049$ | Weak |
| $\Gamma_{b2}$ | $0.7064^{+0.0074}_{-0.011}$ | $0.226^{+0.014}_{-0.011}$ | $105.62 \pm 0.98$ | - | $-0.001 \pm 0.092$ | $0.020^{+0.038}_{-0.030}$ | $-0.194 \pm 0.145$ | Weak |
| $\Gamma_{b3}$ | $0.7092^{+0.0099}_{-0.013}$ | $0.258 \pm 0.028$ | $105.2 \pm 1.0$ | $-0.0046^{+0.0023}_{-0.0043}$ | $-0.0046^{+0.0023}_{-0.0043}$ | $0.003 \pm 0.042$ | $-1.347 \pm 0.585$ | Weak |
| $\Gamma_{b4}$ | $0.7091^{+0.0099}_{-0.013}$ | $0.259 \pm 0.026$ | $105.2 \pm 1.1$ | $-0.0051^{+0.0026}_{-0.0036}$ | $-0.012 \pm 0.095$ | $0.003 \pm 0.041$ | $-2.434 \pm 0.127$ | Weak |
| $\Gamma_{c}$ | $0.7061^{+0.0076}_{-0.011}$ | $0.238^{+0.023}_{-0.021}$ | $105.47 \pm 0.99$ | $-0.051^{+0.062}_{-0.085}$ | - | $0.017 \pm 0.037$ | $-0.083 \pm 0.113$ | Inconclusive |
| $\Gamma_{d}$ | $0.7089^{+0.0098}_{-0.013}$ | $0.259 \pm 0.028$ | $105.2 \pm 1.0$ | $0.0048^{+0.0040}_{-0.0025}$ | - | $0.004 \pm 0.040$ | $-2.291 \pm 0.131$ | Weak |
| $\Gamma_{e}$ | $0.7069^{+0.0080}_{-0.011}$ | $0.240^{+0.030}_{-0.021}$ | $105.5 \pm 1.0$ | $-0.044^{+0.053}_{-0.074}$ | - | $0.018^{+0.040}_{-0.035}$ | $-0.242 \pm 0.076$ | Inconclusive |

Table 3.11: Best fit parameters for the joint analysis JLA + BAO3 + CC + CMB. The last two columns show the Bayes factor ($\ln B$) and the interpretation of the strength of the evidence. Note that $\ln B < -1$ favours the $\Lambda$CDM model. These results consider as priors scenario (3.36).

| Model | $h$ | $\Omega_{dm0}$ | $r_d h$ [Mpc] | $\alpha$ | $\beta$ | $\gamma_x$ | $\ln B$ | Interpretation |
|---|---|---|---|---|---|---|---|---|
| $\Lambda$CDM | $0.7100^{+0.0077}_{-0.011}$ | $0.225^{+0.012}_{-0.0095}$ | $102.45 \pm 0.88$ | - | - | - | - | |
| $\Gamma_{a01}$ | $0.713^{+0.010}_{-0.012}$ | $0.239 \pm 0.019$ | $101.9 \pm 1.0$ | $0.00090^{+0.0060}_{-0.00092}$ | - | - | $-2.909 \pm 0.148$ | Moderate |
| $\Gamma_{a02}$ | $0.7100^{+0.0079}_{-0.011}$ | $0.235^{+0.036}_{-0.031}$ | $102.26 \pm 0.96$ | - | $-0.017^{+0.054}_{-0.062}$ | - | $-0.448 \pm 0.140$ | Inconclusive |
| $\Gamma_{a03}$ | $0.713^{+0.010}_{-0.013}$ | $0.242^{+0.015}_{-0.025}$ | $101.9 \pm 1.1$ | $-0.0065^{+0.014}_{-0.0059}$ | $-0.0065^{+0.014}_{-0.0059}$ | - | $-2.802 \pm 0.141$ | Moderate |
| $\Gamma_{a04}$ | $0.713^{+0.011}_{-0.013}$ | $0.232 \pm 0.034$ | $101.9 \pm 1.1$ | $0.0030^{+0.0051}_{-0.0029}$ | $0.020 \pm 0.073$ | - | $-2.937 \pm 0.175$ | Moderate |
| $\Gamma_{b01}$ | $0.7136^{+0.0099}_{-0.013}$ | $0.238 \pm 0.019$ | $102.0 \pm 1.1$ | $-0.0026^{+0.0027}_{-0.0044}$ | - | - | $-2.610 \pm 0.330$ | Moderate |
| $\Gamma_{b03}$ | $0.713^{+0.010}_{-0.013}$ | $0.239 \pm 0.018$ | $101.9 \pm 1.0$ | $-0.00063^{+0.00055}_{-0.0063}$ | $-0.00063^{+0.00055}_{-0.0063}$ | - | $-3.030 \pm 0.124$ | Moderate |
| $\Gamma_{b04}$ | $0.714^{+0.010}_{-0.013}$ | $0.238 \pm 0.019$ | $102.0 \pm 1.0$ | $-0.0028^{+0.0029}_{-0.0040}$ | $-0.013 \pm 0.098$ | - | $-3.114 \pm 0.128$ | Moderate |
| $\Gamma_{c0}$ | $0.7100^{+0.0081}_{-0.011}$ | $0.230 \pm 0.019$ | $102.32 \pm 0.91$ | $-0.021^{+0.069}_{-0.082}$ | - | - | $-0.256 \pm 0.122$ | Inconclusive |
| $\Gamma_{d0}$ | $0.7139^{+0.0099}_{-0.013}$ | $0.238 \pm 0.019$ | $101.9 \pm 1.0$ | $0.0028^{+0.0040}_{-0.0028}$ | - | - | $-2.844 \pm 0.248$ | Moderate |
| $\Gamma_{e0}$ | $0.7095^{+0.0078}_{-0.011}$ | $0.230^{+0.029}_{-0.025}$ | $102.33 \pm 0.92$ | $-0.014^{+0.067}_{-0.076}$ | - | - | $-0.317 \pm 0.130$ | Inconclusive |
| $\Gamma_{a1}$ | $0.713^{+0.010}_{-0.013}$ | $0.240 \pm 0.023$ | $101.9 \pm 1.1$ | $0.0027^{+0.0043}_{-0.0027}$ | - | $-0.006 \pm 0.041$ | $-1.945 \pm 0.132$ | Weak |
| $\Gamma_{a2}$ | $0.7096^{+0.0083}_{-0.011}$ | $0.236^{+0.039}_{-0.032}$ | $102.24 \pm 0.98$ | - | $-0.018^{+0.053}_{-0.062}$ | $-0.003 \pm 0.039$ | $-0.221 \pm 0.168$ | Inconclusive |
| $\Gamma_{a3}$ | $0.713^{+0.010}_{-0.013}$ | $0.243^{+0.020}_{-0.028}$ | $101.9 \pm 1.0$ | $-0.0045^{+0.012}_{-0.0042}$ | $-0.0045^{+0.012}_{-0.0042}$ | $-0.006 \pm 0.041$ | $-1.167 \pm 0.784$ | Weak |
| $\Gamma_{a4}$ | $0.713^{+0.011}_{-0.013}$ | $0.235 \pm 0.037$ | $101.9 \pm 1.1$ | $0.0026^{+0.0054}_{-0.0025}$ | $0.017 \pm 0.072$ | $-0.008 \pm 0.041$ | $-2.123 \pm 0.213$ | Weak |
| $\Gamma_{b1}$ | $0.713^{+0.010}_{-0.013}$ | $0.240 \pm 0.023$ | $101.9 \pm 1.0$ | $-0.0027^{+0.0028}_{-0.0042}$ | - | $-0.006 \pm 0.041$ | $-3.009 \pm 0.201$ | Moderate |
| $\Gamma_{b2}$ | $0.7095^{+0.0079}_{-0.011}$ | $0.226^{+0.015}_{-0.013}$ | $102.40 \pm 0.90$ | - | $-0.005 \pm 0.093$ | $0.000 \pm 0.035$ | $-0.421 \pm 0.116$ | Inconclusive |
| $\Gamma_{b3}$ | $0.7134^{+0.0098}_{-0.013}$ | $0.240 \pm 0.023$ | $101.9 \pm 1.1$ | $-0.0027^{+0.0027}_{-0.0042}$ | $-0.0027^{+0.0027}_{-0.0042}$ | $-0.006 \pm 0.040$ | $-3.216 \pm 0.118$ | Moderate |
| $\Gamma_{b4}$ | $0.7136^{+0.0099}_{-0.013}$ | $0.240 \pm 0.023$ | $101.9 \pm 1.0$ | $-0.0029^{+0.0027}_{-0.0040}$ | $-0.010 \pm 0.096$ | $-0.007 \pm 0.040$ | $-3.242 \pm 0.120$ | Moderate |
| $\Gamma_c$ | $0.7097^{+0.0081}_{-0.011}$ | $0.231 \pm 0.021$ | $102.33 \pm 0.90$ | $-0.021^{+0.070}_{-0.086}$ | - | $-0.002 \pm 0.037$ | $-0.419 \pm 0.119$ | Inconclusive |
| $\Gamma_d$ | $0.7141^{+0.0098}_{-0.013}$ | $0.241 \pm 0.023$ | $101.9 \pm 1.0$ | $0.0029^{+0.0040}_{-0.0027}$ | - | $-0.007 \pm 0.041$ | $-2.458 \pm 0.540$ | Weak |
| $\Gamma_e$ | $0.7089^{+0.0087}_{-0.011}$ | $0.230^{+0.032}_{-0.026}$ | $102.30 \pm 0.92$ | $-0.011^{+0.066}_{-0.076}$ | - | $-0.001 \pm 0.038$ | $-0.32 \pm 0.185$ | Inconclusive |

Table 3.12: Best fit parameters for the joint analysis Pantheon + BAO3 + CC + CMB. The last two columns show the Bayes factor ($\ln B$) and the interpretation of the strength of the evidence. Note that $\ln B < -1$ favours the $\Lambda$CDM model. These results consider as priors scenario (3.36).

| Model | $h$ | $\Omega_{dm0}$ | $r_d h$ [Mpc] | $\alpha$ | $\beta$ | $\gamma_x$ | $\ln B$ | Interpretation |
|---|---|---|---|---|---|---|---|---|
| $\Lambda$CDM | $0.7038^{+0.0081}_{-0.010}$ | $0.232^{+0.012}_{-0.010}$ | $102.13 \pm 0.89$ | - | - | - | - | |
| $\Gamma_{a01}$ | $0.713^{+0.011}_{-0.013}$ | $0.244 \pm 0.016$ | $101.70 \pm 0.97$ | $0.0033^{+0.0038}_{-0.0023}$ | - | - | $-2.390 \pm 0.316$ | Weak |
| $\Gamma_{a02}$ | $0.7051^{+0.0085}_{-0.011}$ | $0.240^{+0.032}_{-0.029}$ | $102.01 \pm 0.92$ | - | $-0.016^{+0.054}_{-0.061}$ | - | $-0.138 \pm 0.152$ | Inconclusive |
| $\Gamma_{a03}$ | $0.712^{+0.010}_{-0.013}$ | $0.244 \pm 0.017$ | $101.67 \pm 0.95$ | $0.0019^{+0.0054}_{-0.0010}$ | $0.0019^{+0.0054}_{-0.0010}$ | - | $-2.622 \pm 0.078$ | Moderate |
| $\Gamma_{a04}$ | $0.712^{+0.010}_{-0.013}$ | $0.231 \pm 0.030$ | $101.70 \pm 0.94$ | $0.0047^{+0.0039}_{-0.0029}$ | $0.040 \pm 0.070$ | - | $-2.893 \pm 0.034$ | Moderate |
| $\Gamma_{b01}$ | $0.713^{+0.011}_{-0.013}$ | $0.244 \pm 0.016$ | $101.70 \pm 0.96$ | $-0.0037^{+0.0026}_{-0.0035}$ | - | - | $-2.641 \pm 0.049$ | Moderate |
| $\Gamma_{b03}$ | $0.713^{+0.010}_{-0.013}$ | $0.245 \pm 0.016$ | $101.69 \pm 0.96$ | $-0.0033^{+0.0021}_{-0.0039}$ | $-0.0033^{+0.0021}_{-0.0039}$ | - | $-2.192 \pm 0.330$ | Weak |
| $\Gamma_{b04}$ | $0.7137^{+0.0093}_{-0.012}$ | $0.244 \pm 0.016$ | $101.74 \pm 0.96$ | $-0.0038^{+0.0027}_{-0.0032}$ | $-0.012 \pm 0.096$ | - | $-2.814 \pm 0.046$ | Moderate |
| $\Gamma_{c0}$ | $0.7043^{+0.0083}_{-0.011}$ | $0.237 \pm 0.017$ | $102.06 \pm 0.88$ | $-0.019 \pm 0.075$ | - | - | $-0.057 \pm 0.084$ | Inconclusive |
| $\Gamma_{d0}$ | $0.7133^{+0.0098}_{-0.013}$ | $0.248 \pm 0.020$ | $101.69 \pm 0.98$ | $0.0038^{+0.0033}_{-0.0026}$ | - | - | $-2.769 \pm 0.035$ | Moderate |
| $\Gamma_{e0}$ | $0.7041^{+0.0082}_{-0.010}$ | $0.234^{+0.026}_{-0.023}$ | $102.07 \pm 0.88$ | $-0.007 \pm 0.071$ | - | - | $-0.193 \pm 0.047$ | Inconclusive |
| $\Gamma_{a1}$ | $0.7133^{+0.0098}_{-0.012}$ | $0.248 \pm 0.020$ | $101.70 \pm 0.94$ | $0.0031^{+0.0043}_{-0.0017}$ | - | $-0.012 \pm 0.039$ | $-2.813 \pm 0.032$ | Moderate |
| $\Gamma_{a2}$ | $0.7059^{+0.0079}_{-0.010}$ | $0.242 \pm 0.033$ | $102.04 \pm 0.91$ | - | $-0.021 \pm 0.054$ | $-0.004 \pm 0.038$ | $-0.558 \pm 0.064$ | Inconclusive |
| $\Gamma_{a3}$ | $0.713^{+0.010}_{-0.012}$ | $0.248 \pm 0.020$ | $101.70 \pm 0.94$ | $0.0033^{+0.0043}_{-0.0018}$ | $0.0033^{+0.0043}_{-0.0018}$ | $-0.014 \pm 0.040$ | $-2.412 \pm 0.256$ | Weak |
| $\Gamma_{a4}$ | $0.714^{+0.010}_{-0.012}$ | $0.235 \pm 0.034$ | $101.74 \pm 0.91$ | $0.0048^{+0.0039}_{-0.0026}$ | $0.035 \pm 0.068$ | $-0.013 \pm 0.039$ | $-2.698 \pm 0.141$ | Moderate |
| $\Gamma_{b1}$ | $0.7135^{+0.0094}_{-0.012}$ | $0.249 \pm 0.020$ | $101.70 \pm 0.94$ | $-0.0041^{+0.0024}_{-0.0033}$ | - | $-0.015 \pm 0.039$ | $-2.522 \pm 0.239$ | Moderate |
| $\Gamma_{b2}$ | $0.7050^{+0.0078}_{-0.010}$ | $0.231^{+0.015}_{-0.012}$ | $102.14 \pm 0.87$ | - | $-0.005 \pm 0.094$ | $0.002 \pm 0.035$ | $-0.123 \pm 0.054$ | Inconclusive |
| $\Gamma_{b3}$ | $0.713^{+0.011}_{-0.012}$ | $0.249 \pm 0.020$ | $101.73 \pm 0.94$ | $-0.0039^{+0.0024}_{-0.0034}$ | $-0.0039^{+0.0024}_{-0.0034}$ | $-0.015 \pm 0.040$ | $-2.854 \pm 0.029$ | Moderate |
| $\Gamma_{b4}$ | $0.7145^{+0.0089}_{-0.012}$ | $0.248 \pm 0.020$ | $101.75 \pm 0.92$ | $-0.0043^{+0.0026}_{-0.0031}$ | $-0.014 \pm 0.091$ | $-0.015 \pm 0.038$ | $-2.876 \pm 0.068$ | Moderate |
| $\Gamma_c$ | $0.7049^{+0.0079}_{-0.010}$ | $0.236 \pm 0.020$ | $102.06 \pm 0.91$ | $-0.019^{+0.070}_{-0.082}$ | - | $-0.002 \pm 0.036$ | $-0.215 \pm 0.074$ | Inconclusive |
| $\Gamma_d$ | $0.713^{+0.010}_{-0.012}$ | $0.248 \pm 0.020$ | $101.70 \pm 0.95$ | $0.0038^{+0.0034}_{-0.0025}$ | - | $-0.013 \pm 0.040$ | $-2.685 \pm 0.077$ | Moderate |
| $\Gamma_e$ | $0.7040^{+0.0083}_{-0.010}$ | $0.236^{+0.030}_{-0.024}$ | $102.08^{+0.84}_{-0.94}$ | $-0.011 \pm 0.069$ | - | $-0.002 \pm 0.038$ | $-0.322 \pm 0.048$ | Inconclusive |

Table 3.13: Best fit parameters for the joint analysis Pantheon + BAO + CC + CMB. The last three columns show the Bayesian evidence ($\ln \mathcal{E}$), the Bayes factor ($\ln B$) and the interpretation of the strength of the evidence. Note that $\ln B < -1$ favours the $\Lambda$CDM model. These results consider as priors scenario (3.36) and an updated version of BAO data.

| Model | $h$ | $\Omega_{dm0}$ | $r_d h$ [Mpc] | $\alpha$ | $\beta$ | $\gamma_x$ | $\ln B$ | Interpretation |
|---|---|---|---|---|---|---|---|---|
| $\Lambda$CDM | $0.7010 \pm 0.0076$ | $0.2358 \pm 0.0092$ | $102.14 \pm 0.8$ | - | - | - | - | |
| $\Gamma_{a01}$ | $0.711^{+0.011}_{-0.013}$ | $0.242 \pm 0.011$ | $101.82 \pm 0.88$ | $0.0031^{+0.0030}_{-0.0026}$ | - | - | $-3.005 \pm 0.156$ | Moderate |
| $\Gamma_{a02}$ | $0.7012^{+0.0064}_{-0.0079}$ | $0.248^{+0.030}_{-0.026}$ | $101.99 \pm 0.88$ | - | $-0.022 \pm 0.047$ | - | $-0.850 \pm 0.145$ | Inconclusive |
| $\Gamma_{a03}$ | $0.713^{+0.010}_{-0.013}$ | $0.240 \pm 0.011$ | $101.87 \pm 0.91$ | $0.0036^{+0.0029}_{-0.0026}$ | $0.0036^{+0.0029}_{-0.0026}$ | - | $-2.819 \pm 0.211$ | Moderate |
| $\Gamma_{a04}$ | $0.712^{+0.010}_{-0.013}$ | $0.248 \pm 0.028$ | $101.77 \pm 0.93$ | $0.0032^{+0.0029}_{-0.0026}$ | $-0.011 \pm 0.049$ | - | $-3.602 \pm 0.155$ | Moderate |
| $\Gamma_{b01}$ | $0.712^{+0.011}_{-0.013}$ | $0.242 \pm 0.011$ | $101.85 \pm 0.90$ | $-0.0032^{+0.0026}_{-0.0030}$ | - | - | $-3.046 \pm 0.159$ | Moderate |
| $\Gamma_{b03}$ | $0.711^{+0.011}_{-0.013}$ | $0.242 \pm 0.011$ | $101.83 \pm 0.89$ | $-0.0031^{+0.0026}_{-0.0030}$ | $-0.0031^{+0.0026}_{-0.0030}$ | - | $-2.746 \pm 0.258$ | Moderate |
| $\Gamma_{b04}$ | $0.7119^{+0.0096}_{-0.012}$ | $0.242 \pm 0.011$ | $101.85 \pm 0.89$ | $-0.0033 \pm 0.0027$ | $-0.013 \pm 0.096$ | - | $-3.061 \pm 0.157$ | Moderate |
| $\Gamma_{c0}$ | $0.7013^{+0.0066}_{-0.0078}$ | $0.244 \pm 0.018$ | $102.04 \pm 0.85$ | $-0.035 \pm 0.067$ | - | - | $-0.226 \pm 0.211$ | Inconclusive |
| $\Gamma_{d0}$ | $0.7130^{+0.0097}_{-0.012}$ | $0.242 \pm 0.011$ | $101.83 \pm 0.90$ | $0.0035^{+0.0027}_{-0.0024}$ | - | - | $-3.060 \pm 0.146$ | Moderate |
| $\Gamma_{e0}$ | $0.7014^{+0.0063}_{-0.0078}$ | $0.239^{+0.027}_{-0.022}$ | $102.10 \pm 0.85$ | $-0.014 \pm 0.068$ | - | - | $-0.384 \pm 0.157$ | Inconclusive |
| $\Gamma_{a1}$ | $0.712^{+0.010}_{-0.012}$ | $0.241 \pm 0.013$ | $101.81 \pm 0.92$ | $0.0034^{+0.0029}_{-0.0025}$ | - | $0.005^{+0.038}_{-0.033}$ | $-3.286 \pm 0.147$ | Moderate |
| $\Gamma_{a2}$ | $0.7019^{+0.0060}_{-0.0074}$ | $0.248^{+0.035}_{-0.031}$ | $102.05 \pm 0.86$ | - | $-0.024 \pm 0.051$ | $-0.004 \pm 0.036$ | $-0.821 \pm 0.167$ | Inconclusive |
| $\Gamma_{a3}$ | $0.712^{+0.010}_{-0.013}$ | $0.239 \pm 0.012$ | $101.78 \pm 0.89$ | $0.0033 \pm 0.0027$ | $0.0033 \pm 0.0027$ | $0.006 \pm 0.035$ | $-3.088 \pm 0.200$ | Moderate |
| $\Gamma_{a4}$ | $0.7127^{+0.0095}_{-0.012}$ | $0.249^{+0.037}_{-0.032}$ | $101.75 \pm 0.90$ | $0.0035 \pm 0.0026$ | $-0.013 \pm 0.054$ | $-0.002 \pm 0.039$ | $-3.822 \pm 0.146$ | Moderate |
| $\Gamma_{b1}$ | $0.7128^{+0.0095}_{-0.013}$ | $0.240 \pm 0.012$ | $101.82 \pm 0.90$ | $-0.0034 \pm 0.0026$ | - | $0.004 \pm 0.034$ | $-3.314 \pm 0.148$ | Moderate |
| $\Gamma_{b2}$ | $0.7016^{+0.0061}_{-0.0074}$ | $0.234 \pm 0.010$ | $102.16^{+0.78}_{-0.87}$ | - | $-0.0095 \pm 0.096$ | $0.004^{+0.036}_{-0.032}$ | $-0.390 \pm 0.160$ | Inconclusive |
| $\Gamma_{b3}$ | $0.7130^{+0.0099}_{-0.012}$ | $0.241^{+0.012}_{-0.013}$ | $101.83 \pm 0.90$ | $-0.0035 \pm 0.0027$ | $-0.0035 \pm 0.0027$ | $0.004 \pm 0.035$ | $-3.198 \pm 0.159$ | Moderate |
| $\Gamma_{b4}$ | $0.7132^{+0.0093}_{-0.012}$ | $0.241 \pm 0.012$ | $101.79 \pm 0.88$ | $-0.0036 \pm 0.0026$ | $-0.015 \pm 0.092$ | $0.006 \pm 0.033$ | $-3.136 \pm 0.250$ | Moderate |
| $\Gamma_{c}$ | $0.7014^{+0.0063}_{-0.0075}$ | $0.243 \pm 0.020$ | $102.06 \pm 0.85$ | $-0.033^{+0.063}_{-0.075}$ | - | $-0.001^{+0.038}_{-0.034}$ | $-0.372 \pm 0.158$ | Inconclusive |
| $\Gamma_{d}$ | $0.7126^{+0.0095}_{-0.012}$ | $0.242 \pm 0.013$ | $101.79 \pm 0.89$ | $0.0035 \pm 0.0026$ | - | $0.004 \pm 0.034$ | $-3.328 \pm 0.146$ | Moderate |
| $\Gamma_{e}$ | $0.7012^{+0.0065}_{-0.0077}$ | $0.236^{+0.030}_{-0.023}$ | $102.12^{+0.80}_{-0.90}$ | $-0.007 \pm 0.065$ | - | $0.003 \pm 0.035$ | $-0.605 \pm 0.165$ | Inconclusive |

# Cosmic shear

What is essential is invisible to the eye.

The Little Prince

The discovery of gravitational lensing dates back to over a century, in 1919, during a solar eclipse observed by two simultaneous expeditions, one in Sobral, Brazil and the other in the island of Principe, both lead by Arthur Eddington, which set out to test predictions from general relativity. Their findings confirmed Einstein's predicted deflection by the Sun, of light from stars of the Hyades cluster, and thus GR became the official theory of gravity. Consecutive detections were only made over half a century later in 1979, of the doubly imaged quasar [122], and the lensing distortions in 1987 [123], which reignited the interest in this field. Since then, gravitational lensing has become one of the most important tools for probing cosmology.

The following two chapters will be focused on **weak lensing**, and thus we introduce the reader to its formalism in this chapter. Weak lensing deals with the distortion of light from distant galaxies due to the tidal gravitational field of the density fluctuations at large scales [124]. This effect causes the images to be

sheared, i.e. we observe a change in their ellipticity, known as **cosmic shear**. The information obtained from the lensed images is unique because it probes the underlying matter distribution and hence delivers information on the power spectrum of matter overdensity perturbations which, in turn sheds light on dark energy [125].

In this chapter we closely follow the discussion and demonstrations presented in [126].

## 4.1 Light propagation and the lens equation

We begin by introducing the perturbed metric to first order,

$$g_{\mu\nu} = g_{\mu\nu}^{(0)} + \delta g_{\mu\nu} \ , \tag{4.1}$$

under the condition that

$$\left| \frac{\delta g_{\mu\nu}(x^\lambda)}{g_{\mu\nu}^{(0)}(x^\lambda)} \right| \ll 1 \ . \tag{4.2}$$

Rotating $\delta g_{\mu\nu}$ with respect to the spatial components we get

$$\delta g_{\mu\nu} = a^2(t) \left\{ \begin{matrix} -2\Phi(t, x^\nu) & \omega_i(t, x^\nu) \\ \omega_i(t, x^\nu) & 2\Psi(t, x^\nu)\delta_{ij} + h_{ij}(t, x^\nu) \end{matrix} \right\} \ , \quad \delta^{ij} h_{ij} = 0 \ , \tag{4.3}$$

where we have decomposed $\delta g_{\mu\nu}$ into its tensor, $h_{ij}$, vector, $\omega_i$ and scalar, $\Phi$ and $\Psi$, components [127]. Now the tensor and vector components have scalar parts of their own, but if we choose the Newtonian gauge, we set these to zero, such that our only scalar components are $\Phi$ and $\Psi$, which are known as the **Bardeen gravitational potentials**. This is useful because the density perturbation is also

scalar, and hence decouple from the other components. We can then write

$$ds^2 = \left(1 + \frac{2\Phi}{c^2}\right) dt^2 - a^2(t) \left(1 - \frac{2\Psi}{c^2}\right) d\sigma^2 \ , \tag{4.4}$$

where we are briefly reinserting $c$ for clarity. In GR, when dealing with large scale structures the anisotropic stress vanishes, which implies that $\Psi = \Phi$, and we call $\Phi$ the Newtonian gravitational potential [12].

### 4.1.1 Deflection angle

For a weak gravitational field, we can use $ds = 0$ to find the effective light speed,

$$c' = \left|\frac{d\sigma}{dt}\right| = c\left(1 + \frac{2\Phi}{c^2}\right) \ , \tag{4.5}$$

where $\Phi/c^2 \ll 1$ is used in a first-order Taylor expansion. The next steps taken are the same as conventionally done for light travelling through different mediums. We use $c'$ to obtain the effective index of refraction,

$$n = \frac{c}{c'} = 1 - \frac{2\Phi}{c^2} \ . \tag{4.6}$$

We can then calculate the travel time of the light ray,

$$t = \frac{1}{c} \int_a^b \left(1 - \frac{2\Phi}{c^2}\right) dr \ , \tag{4.7}$$

and thus apply Fermat's principle to look for a path $\sigma(r)$, for which

$$\delta \int_a^b n\left[(\sigma(r)\right] dr = 0 \ . \tag{4.8}$$

If we treat this is as a standard variational problem, it can be written as

$$dr = \left|\frac{d\sigma}{d\lambda}\right| d\lambda \ , \tag{4.9}$$

where $\lambda$ is an arbitrary curve parameter. Substituting in Eq. (4.8),

$$\delta \int_{\lambda_a}^{\lambda_b} n\left[(\sigma(\lambda)\right] \left|\frac{d\sigma}{d\lambda}\right| d\lambda = 0 \ , \tag{4.10}$$

we write the Langrangian,

$$n\left[(\sigma(\lambda)\right] \left|\frac{d\sigma}{d\lambda}\right| \equiv L\left(\dot{\sigma}, \sigma, \lambda\right) \ , \tag{4.11}$$

with the derivative being taken with respect to $\lambda$. We can now use the Euler-Lagrange equations,

$$\frac{d}{d\lambda}\frac{\partial L}{\partial \dot{\sigma}} - \frac{\partial L}{\partial \sigma} = 0 \ , \tag{4.12}$$

where we compute

$$\frac{\partial L}{\partial \sigma} = |\dot{\sigma}|\frac{\partial n}{\partial \sigma} = (\nabla n)\,|\dot{\sigma}| \quad \text{and} \quad \frac{\partial L}{\partial \dot{\sigma}} = \frac{\partial \dot{\sigma}}{\partial |\dot{\sigma}|} \ . \tag{4.13}$$

If we assume that the tangent vector to the light path is $|\dot{\sigma}| = 1$, for a convenient choice for $\lambda$ and, for simplicity, substitute $x \equiv \dot{\sigma}$,

$$\frac{d}{d\lambda}(nx) - \boldsymbol{\nabla}n = 0 \ ,$$
$$n\dot{x} = \boldsymbol{\nabla}n - x\left(\boldsymbol{\nabla}n \cdot x\right) \ . \tag{4.14}$$

Since the second term on the rhs is simply the gradient of $n$ along the line of sight, we can use $\boldsymbol{\nabla} n = \boldsymbol{\nabla}_\perp n + \boldsymbol{\nabla}_\parallel n$ to write

$$\dot{x} = \frac{1}{n}\boldsymbol{\nabla}_\perp n \ ,$$
$$\dot{x} = \boldsymbol{\nabla}_\perp \ln(n) \ .$$

$$(4.15)$$

Plugging in $n = 1 - 2\Phi/c^2$ and $\Phi/c^2 \ll 1$, $\ln(n) \approx -2\Phi/c^2$,

$$\dot{x} \approx -\frac{2}{c^2}\boldsymbol{\nabla}_\perp \Phi \ , \tag{4.16}$$

we find the **deflection angle** to be,

$$\hat{\boldsymbol{\alpha}} = \frac{2}{c^2} \int_{\lambda_a}^{\lambda_b} \boldsymbol{\nabla}_\perp \Phi d\lambda \ . \tag{4.17}$$

## 4.1.2 Lensing potential

We illustrate the schematics for the trajectory of the light path from the source, passing through the lens and converging to the observer in Figure 4.1. The angles shown are exaggerated for clarity but, in reality, they are small enough that we can use $\tan\theta \approx \theta$. Consider the comoving transverse distance between the source, at distance $\chi$ from the observer, and the optical axis, $\boldsymbol{x}_0(\chi) = f_K(\chi)\boldsymbol{\theta}$. The apparent separation will be greater, due to the deflection of the light ray by the potential $\Phi$, which is at $\chi'$ from the observer. The induced change will be given by

$$d\boldsymbol{x} = f_K(\chi - \chi')d\hat{\boldsymbol{\alpha}} \ , \tag{4.18}$$

where

$$d\hat{\boldsymbol{\alpha}} = \frac{2}{c^2}\boldsymbol{\nabla}_\perp \Phi(\boldsymbol{x}, \chi)d\chi' \ . \tag{4.19}$$
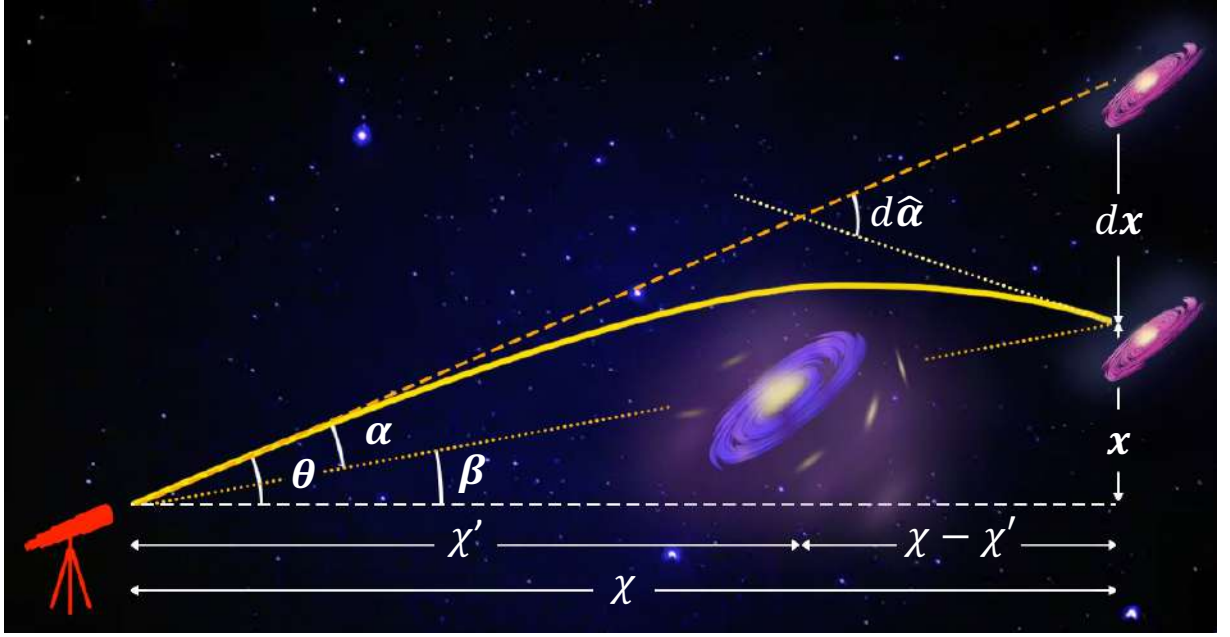
Figure 4.1: The trajectory of a light ray (continuous yellow curve) from the **source**
galaxy on the right (in pink), passing by the **lens** galaxy (in purple), to the
observer represented by the red telescope on the left. The distance from the
observer to the source is $\chi$, and from the observer to the lens is $\chi'$. The
dashed orange curve shows the apparent direction, subtended by the angle
$\boldsymbol{\theta}$, and the dotted white curve is the unperturbed geodesic, which converges
on the observer under the angle $\boldsymbol{\beta}$. Finally, $d\boldsymbol{\hat{\alpha}}$ is the deflection angle, $x(\chi)$
is the distance from the source to the optical axis, and $d\boldsymbol{x}$ is the distance
between the apparent and true location of the source.

Substituting Eq. (4.19) in Eq. (4.18) and integrating along the path,

$$\boldsymbol{x} = f_K(\chi)\boldsymbol{\theta} - \frac{2}{c^2} \int_0^{\chi} d\chi' f_K(\chi - \chi') \left[ \boldsymbol{\nabla}_{\perp} \Phi(\boldsymbol{x}, \chi') \right] \ , \tag{4.20}$$

which is the total transverse separation. Looking at Figure 4.1, we can obtain the
**lens equation**,

$$\boldsymbol{\beta} = \boldsymbol{\theta} - \boldsymbol{\alpha} \ , \tag{4.21}$$

where $\boldsymbol{\beta} = \boldsymbol{x}(\chi)/f_K(\chi)$, which gives

$$\boldsymbol{\alpha} = \frac{2}{c^2} \int_0^\chi d\chi' \frac{f_K(\chi - \chi')}{f_K(\chi)} \boldsymbol{\nabla}_\perp \Phi(\boldsymbol{x}, \chi') \ . \tag{4.22}$$

Up until now, we have been defining our variables in terms of the transverse distance, $\boldsymbol{x}$, it is, however, more convenient to do so in terms of the angular position on the celestial sphere, $\theta$, which can be readily measured for an observer. We therefore swap the gradient $\boldsymbol{\nabla}_\perp$ for,

$$\boldsymbol{\nabla}_\theta = \frac{\boldsymbol{\nabla}_\perp}{\chi'} \ . \tag{4.23}$$

Finally, we introduce the **lensing potential**,

$$\psi(\boldsymbol{\theta}, \chi) = \frac{2}{c^2} \int_0^\chi d\chi' \frac{f_K(\chi - \chi')}{f_K(\chi) f_K(\chi')} \Phi(f_K(\chi')\boldsymbol{\theta}, \chi') \ , \tag{4.24}$$

we can write the deflection angle as the gradient of this potential,

$$\boldsymbol{\alpha} = \boldsymbol{\nabla}_\theta \psi \ , \tag{4.25}$$

where we have used the Born approximation such that the integral is taken along a fiducial straight line, rather than the photon geodesic, and $\boldsymbol{x}(\chi) = f_K(\chi)\boldsymbol{\theta}$.

## 4.2 Convergence and shear

We have already established how the trajectories of the light rays change due to gravitational potential $\Phi$. We now explore other effects, like the magnification and distortion of the source, as illustrated in Figure 4.2. These distortions can be

Figure 4.2: Figure showing the effects of the convergence and shear. The leftmost object is the true galaxy shape. The middle one shows the convergence, which is the isotropic change in size, while maintaining a constant surface brightness. Finally, the rightmost object shows the effects of both convergence and shear, where the shear is the anisotropic stretch in a given direction.

summarised by the Jacobian matrix,

$$
\begin{aligned}
A_{ij} &\equiv \frac{\partial \beta_i}{\partial \theta_j} \ , \\
&= \delta_{ij} - \frac{\partial \alpha_i}{\partial \theta_j} \ , \\
&= \delta_{ij} - \frac{\partial^2 \psi}{\partial \theta_i \partial \theta_j} \ .
\end{aligned}
\tag{4.26}
$$

$\mathbf{A}$ is the amplification matrix describing the linear mapping from lensed coordinates $\boldsymbol{\theta}$ to unlensed coordinates $\boldsymbol{\beta}$, or, alternatively, its inverse is the magnification matrix, which maps the source onto the image coordinates. We can decompose $\mathbf{A}$

into two parts,

$$\left( \mathbf{A} - \frac{1}{2}\mathrm{tr}\mathbf{A} \cdot \mathbb{1} \right)_{ij} = \delta_{ij} - \psi_{ij} - \frac{1}{2}\left( 1 - \psi_{11} + 1 - \psi_{22} \right)\delta_{ij} \ ,$$

$$= -\psi_{ij} + \frac{1}{2}\left( \psi_{11} + \psi_{22} \right)\delta_{ij} \ , \tag{4.27}$$

$$= \begin{pmatrix} -\frac{1}{2}\left( \psi_{11} - \psi_{22} \right) & -\psi_{12} \\ -\psi_{12} & \frac{1}{2}\left( \psi_{11} - \psi_{22} \right) \end{pmatrix} \ ,$$

and

$$\frac{1}{2}\mathrm{tr}\mathbf{A} = \left[ 1 - \frac{1}{2}\left( \psi_{11} + \psi_{22} \right) \right]\delta_{ij} \ , \tag{4.28}$$

where we use $\psi_{ij} = \frac{\partial^2 \psi}{\partial\theta_i\partial\theta_j}$ for brevity. Eq. (4.27) is the **shear matrix**, it is trace-free and characterises the anisotropic stretching of the source image by quantifying the projection of the gravitational tidal field. We can further simplify this matrix by defining the two-component spin-two **shear**, $\gamma$, with a tangential and a cross component, $\gamma_t$ and $\gamma_\times$, respectively, where

$$\gamma_t = \frac{1}{2}\left( \psi_{11} - \psi_{22} \right) \ ,$$

$$\gamma_\times = \psi_{12} \ , \tag{4.29}$$

such that the shear matrix can be rewritten as

$$\begin{pmatrix} \gamma_t & \gamma_\times \\ \gamma_\times & -\gamma_t \end{pmatrix} = \gamma \begin{pmatrix} \cos 2\varphi & \sin 2\varphi \\ \sin 2\varphi & -\cos 2\varphi \end{pmatrix} \ , \tag{4.30}$$

with $\varphi$ being the polar angle between the two components of the shear. It is also convenient to write $\gamma = \gamma_t + i\gamma_\times = |\gamma|\,e^{2i\varphi}$. Eq. (4.28), on the other hand, is an isotropic distortion, known as the **convergence**, $\kappa = \frac{1}{2}\left( \psi_{11} + \psi_{22} \right)$, describing the change in size, while maintaining a constant surface brightness. In practice,

sources are only weakly lensed by the large scale structures of the universe, and so $\kappa$ and $\gamma$ are usually much smaller than unity. Before moving on, we present $\mathbf{A}$ in terms of these new quantities,

$$
\mathbf{A} = \begin{pmatrix} 1 - \kappa - \gamma_t & -\gamma_\times \\ -\gamma_\times & 1 - \kappa + \gamma_t \end{pmatrix} \ . \tag{4.31}
$$

Since weak lensing mostly deals with the shape, rather than the size, our observable is, in fact, the **reduced shear**,

$$
g = \frac{\gamma}{1 - \kappa} \ , \tag{4.32}
$$

which has the same properties as the shear. Furthermore, as we have established that $\kappa$ is often $\ll 1$, such that the shear is a good approximation of the reduced shear.

We now turn back to the convergence, which has some interesting properties to be explored. We find

$$
\begin{aligned}
\kappa(\boldsymbol{\theta}, \chi) &= \frac{1}{2} \left( \frac{\partial^2 \psi}{\partial^2 \theta_1} + \frac{\partial^2 \psi}{\partial^2 \theta_2} \right) \ , \\
&= \boldsymbol{\nabla}_\theta^2 \psi \ , \\
&= \frac{1}{c^2} \boldsymbol{\nabla}_\theta^2 \int_0^\chi d\chi' \frac{f_K(\chi - \chi')}{f_K(\chi) f_K(\chi')} \Phi(f_K(\chi')\boldsymbol{\theta}, \chi') \ , \\
&= \frac{1}{c^2} \int_0^\chi d\chi' \frac{f_K(\chi - \chi') f_K(\chi)}{f_K(\chi')} \boldsymbol{\nabla}_\perp^2 \Phi(f_K(\chi')\boldsymbol{\theta}, \chi') \ ,
\end{aligned} \tag{4.33}
$$

where we used Eq. (4.23). Take Poisson's equation,

$$
\boldsymbol{\nabla}^2 \Phi = \frac{4\pi G a^2 \bar{\rho} \delta}{c^2} \ , \tag{4.34}
$$

where

$$\delta = \frac{\rho - \bar{\rho}}{\bar{\rho}} \tag{4.35}$$

is the density contrast, with $\rho$ being the density and $\bar{\rho}$ the mean density. Since we want to probe the matter distribution we can use $\bar{\rho} \to \bar{\rho}_m$, such that

$$
\begin{aligned}
\bar{\rho}_m &= \frac{\Omega_m \rho_{\mathrm{crit}}}{a^3} \ , \\
&= \frac{3 H_0^2 \Omega_m c^2}{8 \pi G a^3} \ .
\end{aligned}
\tag{4.36}
$$

If we substitute $\bar{\rho}_m$ in Eq. (4.34),

$$\boldsymbol{\nabla}^2 \Phi = \frac{3 H_0^2 \Omega_m \delta}{2a} \ , \tag{4.37}$$

which we can then use in Eq. (4.33),

$$
\begin{aligned}
\kappa(\boldsymbol{\theta}, \chi) &= \frac{3 H_0^2 \Omega_m}{2ac^2} \int_0^\chi d\chi' \frac{f_K(\chi - \chi') f_K(\chi)}{f_K(\chi')} \delta(f_K(\chi')\boldsymbol{\theta}, \chi') \ , \\
&= \int_0^\chi d\chi' \mathcal{W}(\chi, \chi') \delta(f_K(\chi')\boldsymbol{\theta}, \chi') \ ,
\end{aligned}
\tag{4.38}
$$

where

$$\mathcal{W}(\chi, \chi') = \frac{3 H_0^2 \Omega_m}{2ac^2} \frac{f_K(\chi - \chi') f_K(\chi)}{f_K(\chi')} \ , \tag{4.39}$$

is the function that weighing function along the line of sight. Finally, when dealing with a population of source galaxies, we take the mean convergence,

$$\kappa(\boldsymbol{\theta}) = \int d\chi \ n(\chi) \kappa(\boldsymbol{\theta}, \chi) \ , \tag{4.40}$$

which is weighted by the galaxy probability distribution, $n(\chi)d\chi = n(z)dz$, that can be obtained using photometric redshifts.

## 4.3 Lensing power spectrum

Since we do not know the underlying matter distribution of large scale structures, we cannot predict the expected lensing effects; we hence turn to correlations between the sources. Take a measured quantity on the sky, $g(\boldsymbol{\vartheta})$, and its angular two point correlation function, $\xi_{gg}(\boldsymbol{\theta}) = \langle g(\boldsymbol{\vartheta}) g^*(\boldsymbol{\vartheta} + \boldsymbol{\theta}) \rangle$. Its **angular power spectrum** is its Fourier transform,

$$\langle \hat{g}(\boldsymbol{k}) \hat{g}^*(\boldsymbol{k}') \rangle = \int d^3\vartheta \; e^{i\boldsymbol{\vartheta}\cdot\boldsymbol{k}} \int d^3\vartheta' \; e^{-i\boldsymbol{\vartheta}'\cdot\boldsymbol{k}'} \langle g(\boldsymbol{\vartheta}) g^*(\boldsymbol{\vartheta}') \rangle \;, \qquad (4.41)$$

substituting $\boldsymbol{\vartheta}' = \boldsymbol{\vartheta} + \boldsymbol{\theta}$,

$$\begin{aligned} \langle \hat{g}(\boldsymbol{k}) \hat{g}^*(\boldsymbol{k}') \rangle &= \int d^3\vartheta \; e^{i\boldsymbol{\vartheta}\cdot\boldsymbol{k}} \int d^3\theta \; e^{-i(\boldsymbol{\vartheta}+\boldsymbol{\theta})\cdot\boldsymbol{k}'} \langle g(\boldsymbol{\vartheta}) g^*(\boldsymbol{\vartheta} + \boldsymbol{\theta}) \rangle \;, \\ &= (2\pi)^3 \delta_D^{(3)}(\boldsymbol{k} - \boldsymbol{k}') \int d^3\theta \; e^{-i\boldsymbol{\theta}\cdot\boldsymbol{k}'} \langle g(\boldsymbol{\vartheta}) g^*(\boldsymbol{\vartheta} + \boldsymbol{\theta}) \rangle \;, \\ &= (2\pi)^3 \delta_D^{(3)}(\boldsymbol{k} - \boldsymbol{k}') P_g(k) \;, \end{aligned} \qquad (4.42)$$

where

$$P_g(k) \equiv \int d^3\theta \; e^{-i\boldsymbol{k}\cdot\boldsymbol{\theta}} \xi_{gg}(\boldsymbol{\theta}) \;, \qquad (4.43)$$

is the power spectrum, and $\delta_D^{(3)}$ is the Dirac delta function in 3 dimensions. In cosmology, we often use the Limber approximation, which ensures that a two dimensional quantity such as the convergence,

$$\kappa(\boldsymbol{\theta}) = \int d\chi' \; q(\chi') \delta(f_K(\chi')\boldsymbol{\theta}, \chi') \;, \qquad (4.44)$$

can be expressed as a projection of a three dimensional one, $\delta(f_K(\chi')\boldsymbol{\theta}, \chi')$. For simplicity, we write

$$q(\chi') = \frac{3H_0^2\Omega_m}{2ac^2} \frac{f_K(\chi - \chi')f_K(\chi)}{f_K(\chi')} \ . \tag{4.45}$$

Before we proceed to calculate the power spectrum of the convergence, we look for its correlation function,

$$\xi_{\kappa\kappa} = \langle \kappa(\boldsymbol{\theta})\kappa(\boldsymbol{\theta}')\rangle \ ,$$

$$= \int q(\chi)d\chi \int q(\chi')d\chi' \langle \delta(f_K(\chi)\boldsymbol{\theta}, \chi)\delta(f_K(\chi')\boldsymbol{\theta}, \chi')\rangle \ ,$$

$$= \int q(\chi)d\chi \int q(\chi')d\chi' \int \frac{d^3k}{(2\pi)^3} \int \frac{d^3k'}{(2\pi)^3} \langle \delta(\boldsymbol{k})\delta^*(\boldsymbol{k}')\rangle \tag{4.46}$$

$$e^{-if_k(\chi)\boldsymbol{\theta}\cdot\boldsymbol{k}_\perp} e^{-if_k(\chi')\boldsymbol{\theta}'\cdot\boldsymbol{k}'_\perp} e^{-i\boldsymbol{k}_\parallel\chi} e^{-i\boldsymbol{k}'_\parallel\chi'} \ ,$$

where we have taken the Fourier transform of $\delta$ and separated the wave vector $\boldsymbol{k}$ into its perpendicular, $\boldsymbol{k}_\perp$, and parallel, $\boldsymbol{k}_\parallel$ parts. We can further replace the power spectrum of $\delta$,

$$\xi_{\kappa\kappa} = \int q(\chi)d\chi \int q(\chi')d\chi' \int \frac{d^3k}{(2\pi)^3} 2\pi\delta_D(\boldsymbol{k}_\parallel)P_\delta(k) \ e^{-i(f_k(\chi)\boldsymbol{\theta} - f_k(\chi')\boldsymbol{\theta}')\cdot\boldsymbol{k}_\perp} \ ,$$

$$= \int q^2(\chi)d\chi \int \frac{d^2k_\perp}{(2\pi)^2} P_\delta(|k_\perp|)e^{if_k(\chi)(\boldsymbol{\theta}-\boldsymbol{\theta}')\cdot\boldsymbol{k}_\perp} \ , \tag{4.47}$$

$$= \int q^2(\chi)d\chi \int \frac{d^2k}{(2\pi)^2} P_\delta(k)e^{if_k(\chi)\boldsymbol{k}\cdot\boldsymbol{\vartheta}} \ .$$

To derive the above result, we defined $\vartheta = |\theta - \theta'|$ and used the isotropy of the

universe to replace $\boldsymbol{k}_{\parallel} \to k$. Finally, the power spectrum of the convergence is

$$
\begin{aligned}
P_\kappa(\ell) &= \int d^2\vartheta \; \xi_{\kappa\kappa}(\vartheta) \; e^{i\boldsymbol{\ell}\cdot\boldsymbol{\vartheta}} \; , \\
&= \int q^2(\chi)d\chi \int \frac{d^2k}{(2\pi)^2} P_\delta(k) e^{i(\boldsymbol{\ell}-f_k(\chi)\boldsymbol{k})\cdot\boldsymbol{\vartheta}} \; , \\
&= \int d\chi \frac{q^2(\chi)}{f_k^2(\chi)} P_\delta\left(\frac{\ell}{f_k(\chi)}\right) \; .
\end{aligned}
\tag{4.48}
$$

## 4.4 Shear correlation function

Recall the tangential and cross components of the shear defined earlier, $\gamma_t$ and $\gamma_\times$, and the lensing potential $\psi$. We let the separation vector $\boldsymbol{\phi}$ between two arbitrary points have a polar angle $\alpha$. We start with the correlation function of the tangential component of the shear,

$$
\langle \gamma_t \gamma_t' \rangle = \int \frac{d^2\ell}{(2\pi)^2} P_{\gamma_t}(\ell) e^{-i\boldsymbol{\ell}\cdot\boldsymbol{\phi}} \; ,
\tag{4.49}
$$

and its Fourier transform,

$$
\hat{\gamma}_t = \frac{k^2}{2} \left( \cos^2\alpha - \sin^2\alpha \right) \hat{\psi} \; .
\tag{4.50}
$$

We find its power spectrum,

$$
P_{\gamma_t} = \frac{k^4}{4} \left( \cos^2\alpha - \sin^2\alpha \right)^2 P_\psi \; .
\tag{4.51}
$$

We can relate $P_\psi$ to the power spectrum of the convergence,

$$
P_\kappa = \frac{k^4}{4} P_\psi \; ,
\tag{4.52}
$$

and thus,

$$P_{\gamma_t} = \left(\cos^2 \alpha - \sin^2 \alpha\right)^2 P_\kappa \; ,$$

$$= \frac{1}{2} \left(1 + \cos 4\alpha\right)^2 P_\kappa \; . \tag{4.53}$$

Plugging this result back in Eq. (4.50),

$$\langle \gamma_t \gamma_t' \rangle = \int \frac{d^2\ell}{(2\pi)^2} \left(\cos^2 \alpha - \sin^2 \alpha\right)^2 P_\kappa(\ell) e^{-i\boldsymbol{\ell}\cdot\boldsymbol{\phi}} \; ,$$

$$= \int \frac{\ell d\ell}{2(2\pi)^2} P_\kappa(\ell) \int d\alpha \; e^{-i\ell\phi\cos\alpha} \left(1 + \cos 4\alpha\right) \; ,$$

$$= \int \frac{\ell d\ell}{2(2\pi)^2} P_\kappa(\ell) \left[ \int d\alpha \; e^{-i\ell\phi\cos\alpha} + \int d\alpha \; e^{-i\ell\phi\cos\alpha} \cos 4\alpha \right] \; ,$$

$$= \int \frac{\ell d\ell}{4\pi} P_\kappa(\ell) \left[J_0(\ell\phi) + J_4(\ell\phi)\right] \; , \tag{4.54}$$

where $J_0$ and $J_4$ are Bessel functions of the first kind [128]. Similarly, for the cross component we have its power spectrum,

$$P_{\gamma_\times} = \frac{1}{2} \left(1 - \cos 4\alpha\right)^2 P_\kappa \; , \tag{4.55}$$

from which its autocorrelation can be found,

$$\langle \gamma_\times \gamma_\times' \rangle = \int \frac{\ell d\ell}{4\pi} P_\kappa(\ell) \left[J_0(\ell\phi) - J_4(\ell\phi)\right] \; . \tag{4.56}$$

We omit the calculation of the mixed correlations between $\gamma_\times$ and $\gamma_t$ since they are equal to zero. Finally, we define the shear correlation functions $\xi_\pm = \langle \gamma_t \gamma_t' \rangle \pm \langle \gamma_\times \gamma_\times' \rangle$, so that we can write

$$\xi_+ = \int \frac{\ell d\ell}{2\pi} P_\kappa(\ell) J_0(\ell\phi) \tag{4.57}$$

and

$$\xi_- = \int \frac{\ell d\ell}{2\pi} P_\kappa(\ell) J_4(\ell\phi) \,. \tag{4.58}$$

There two quantities will be essential for the work presented in the next two sections.

# Data compression and covariance matrix inspection: Cosmic shear

> Truth suffers from too much analysis.
>
> ――――――――――――――――――――
>
> Dune Chapterhouse

In this chapter I detail the work I did in collaboration with Tianqing Zhang, Niyani Chen and Scott Dodelson, in [129], for the Vera Rubin Observatory Legacy Survey of Space and Time, Dark Energy Science Collaboration.[1]

## 5.1 Motivation

As we have seen in the previous chapter, cosmic shear is a weak lensing effect caused by the large-scale structure of the universe and is an important tool for constraining cosmology. For a cosmological analysis, it is common to assume that the two-point functions follow a Gaussian distribution, and thus require a covariance matrix. If the data vector has length $n$, then it has a symmetric $n \times n$

―――――――――――――――

[1] https://lsstdesc.org/

covariance matrix with $n \times (n+1)/2$ individual elements that capture its auto and cross-correlation. The number of elements of the covariance matrix thus increases quadratically, such that, the larger the data vector, the harder it is to analyse the covariance matrix.

One of the common ways to reduce the dimensionality of the dataset and its corresponding covariance matrix is to employ compression schemes. The most powerful ones, as we will see, are capable of shrinking the number of elements of the data vector down to the number of free parameters of the analysis. In this chapter, we explore different compression methods to help identify the parts of the covariance matrix which are most crucial to parameter estimation. These are then evaluated based on how well they reproduce the original parameter constraints.

Next, we show that compression can be an effective tool for comparing covariance matrices. Finally, we perform a tolerance test on the elements of the compressed covariance matrix. This is done by investigating the change in the parameter constraints due the noise added separately to elements and eigenvalues of the covariance matrix.

## 5.2 Methods

### 5.2.1 DES Cosmic Shear: Data and Analysis

To test the compression schemes, we use cosmic shear statistics from the Dark Energy Survey Year 1 (DESY1) [130, 131]. The data were taken over an area of 1321 deg$^2$ of the southern sky and are divided into four tomographic redshift bins ranging from $0.20 < z < 1.30$ [132], according to the posterior of the photometric redshift as estimated from $griz^2$ flux measurements [133]. Each bin then yields 10 bin-pair combinations, with each one containing 20 angular bins between 2.5 and

---

$^2 g$: green; $r$: red; $i$ and $z$: near-infrared.

250 arcmin, resulting in 200 data points per statistic.

Not all angular bins are used, however, since smaller scales are more sensitive to baryonic feedback from supernovae, gas cooling, and active galactic nuclei (AGN) [134]. To establish which scales should be removed, DESY1 modelled these effects as a rescaling of the nonlinear matter power spectrum. The scales from the $\xi_\pm$ dataset with a fractional contamination from baryonic effects superior to 2% at any physical scales are removed. This results in 167 points for $\xi_+(\theta)$ and 60 for $\xi_-(\theta)$, totalling 227 points.

For the analyses, we assume a flat $\Lambda$CDM model, with six free parameters, $\{A_s, \Omega_m, \Omega_b, \Omega_\nu h^2, H_0, n_s\}$. We fix the equation of state for the dark energy component, $w = -1$, and $\tau = 0.08$. Since we do not consider baryonic effects, the astrophysical systematics are mostly dominated by intrinsic alignment (IA), which describes the coherent orientation of galaxies due to overdense regions. We vary the amplitude of the nonlinear alignment model, $A_{IA0}$, and its redshift evolution, $\eta_{IA}$. We also have the shear multiplicative bias, $m^i$, which varies with each tomographic bin. Lastly, we vary the photo-$z$ bias, $\Delta z^i$, on the distribution of galaxies in each redshift bin. The priors for these 16 parameters are given in Table 5.1. Since cosmic shear is not sensitive to most of these, their constraints are largely dependent on the priors used. As such, throughout, we will mostly only be showing constraints on three parameters: the matter density parameter, $\Omega_m$, the amplitude of matter fluctuations, $S_8 \equiv \sigma_8(\Omega_m/0.3)^{0.5}$, and the amplitude of the intrinsic alignment, $A_{IA}$.

The cosmological parameter inference is performed with the `CosmoSIS` [135, 136, 137, 138, 139, 140, 141, 142] pipeline, while employing the `MultiNest` [112] sampler to explore the parameter space, with 1000 `livepoints`, `efficiency` set to 0.05, `tolerance` to 0.1 and `constant_efficiency` set to True.

We use the aforementioned dataset alongside two different covariance matrices.

Table 5.1: List of the priors used in the analysis for parameter constraints using DESY1 data. $\mathcal{U}$ denotes flat in the given range and $\mathcal{G}$ is Gaussian with mean equal to its first argument and dispersion equal to its second.

| Parameter | Prior |
|---|---|
| Cosmological | |
| $\Omega_m$ | $\mathcal{U}(0.1, 0.9)$ |
| $\log A_s$ | $\mathcal{U}(3.0, 3.1)$ |
| $H_0$ (km s$^{-1}$Mpc$^{-1}$) | $\mathcal{U}(55, 91)$ |
| $\Omega_b$ | $\mathcal{U}(0.03, 0.07)$ |
| $\Omega_\nu h^2$ | $\mathcal{U}(0.0005, 0.01)$ |
| $n_s$ | $\mathcal{U}(0.87, 1.07)$ |
| Astrophysical | |
| $A_{\mathrm{IA}}$ | $\mathcal{U}(-5, 5)$ |
| $\eta_{\mathrm{IA}}$ | $\mathcal{U}(-5, 5)$ |
| Systematic | |
| $m^i$ | $\mathcal{G}(0.012, 0.023)$ |
| $\Delta z^1$ | $\mathcal{G}(-0.001, 0.016)$ |
| $\Delta z^2$ | $\mathcal{G}(-0.019, 0.013)$ |
| $\Delta z^3$ | $\mathcal{G}(0.009, 0.011)$ |
| $\Delta z^4$ | $\mathcal{G}(-0.018, 0.022)$ |

The covariance matrix that we will refer to as the Full Covariance Matrix (FCM) is the one originally used in the DESY1 cosmic shear analysis in [131]. It was analytically obtained with `CosmoLike` [143] and is mainly dominated by the shape-noise and Gaussian components of the covariance, with a halo model framework being used to include the non-Gaussian parts.

The one that we will call the Gaussian Covariance Matrix (GCM) was computed with the code used for the KiDS-450 and KiDS-1000 surveys [144, 145]. Similarly to the FCM, it is analytical, and was obtained following the procedure in [146] for obtaining second-order cosmic shear measurements under the assumption that density field is Gaussian, the galaxies are uniformly distributed, and the survey has a straightforward geometry. Contrary to the FCM, however, it was produced

only considering the Gaussian contributions to shape-noise, sample variance and the mixed noise-sample variance term. The non-Gaussian components and the super-sample covariance were not included, so that the differences are accentuated in the two covariance matrices and in the parameter constraints. These ensuing discrepancies help us assess various validation techniques. Where not otherwise stated, the analysis and constraints are performed on the FCM.

Figure 5.1 shows the cosmological constraints for the FCM and the GCM, while Figure 5.2 shows the constraints for the systematic parameters. The 68% confidence level (CL) constraints are as follows, for the three parameters of interest: for the FCM: $\Omega_m = 0.306^{+0.018}_{-0.023}$, $S_8 = 0.784^{+0.054}_{-0.06}$ and $A_{\mathrm{IA}} = 0.852^{+0.359}_{-0.233}$; and for the GCM: $\Omega_m = 0.309^{+0.017}_{-0.023}$, $S_8 = 0.787^{+0.051}_{-0.058}$ and $A_{\mathrm{IA}} = 0.948^{+0.329}_{-0.22}$. This shows that the variations we introduced to the calculation of the two matrices are measurable in the parameter constraints.

### 5.2.2 Eigenvalues

One of the simplest ways of analysing the covariance matrix is to probe its eigenvalues. Each eigenvalue is associated with a linear combination of the data vector, or a *mode*. The smallest eigenvalues are usually attributed to numerical noise and, therefore, are the least relevant to parameter estimation. The largest eigenvalues, on the other hand, have the largest variance and are thus considered to be the most significant ones [147].

To shrink the covariance matrix based on this information, we first diagonalise the covariance matrix to obtain its eigenvalues, and then sort them in increasing order. One of the ways to remove the effective contribution of the lowest eigenvalues, would be to set them to zero. This would, however, result in a non-positive definite (NPD) matrix. Since we do not want to alter this characteristic of the covariance matrix, we resort to replacing these smaller eigenvalues with values nine
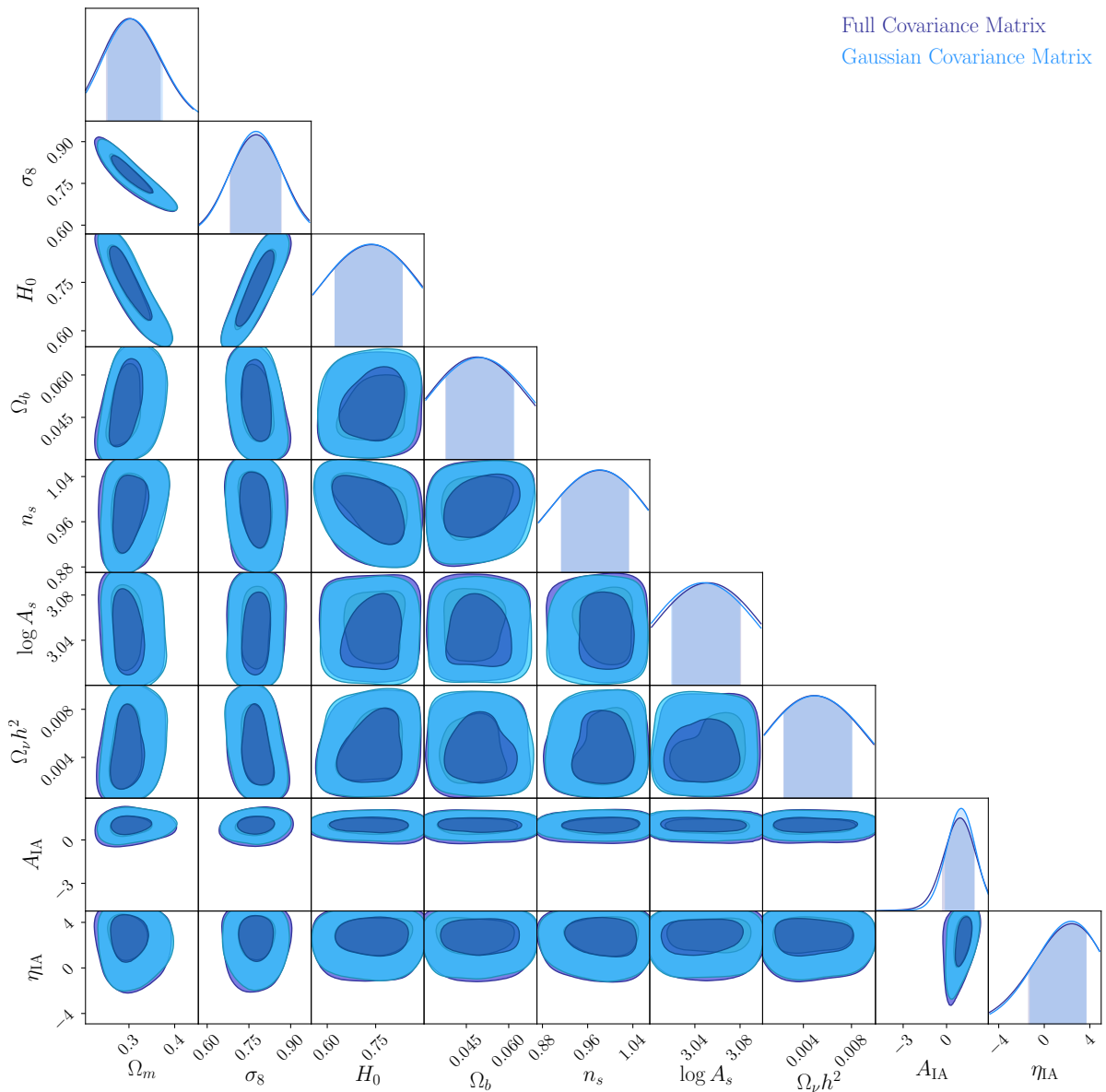
Figure 5.1: Constraints on cosmological parameters for two covariance matrices produced for cosmic shear. The purple curve is for the FCM while the blue is for the GCM. In the 16–dimensional parameter space, the volume of the posterior is about 22% larger for the former.
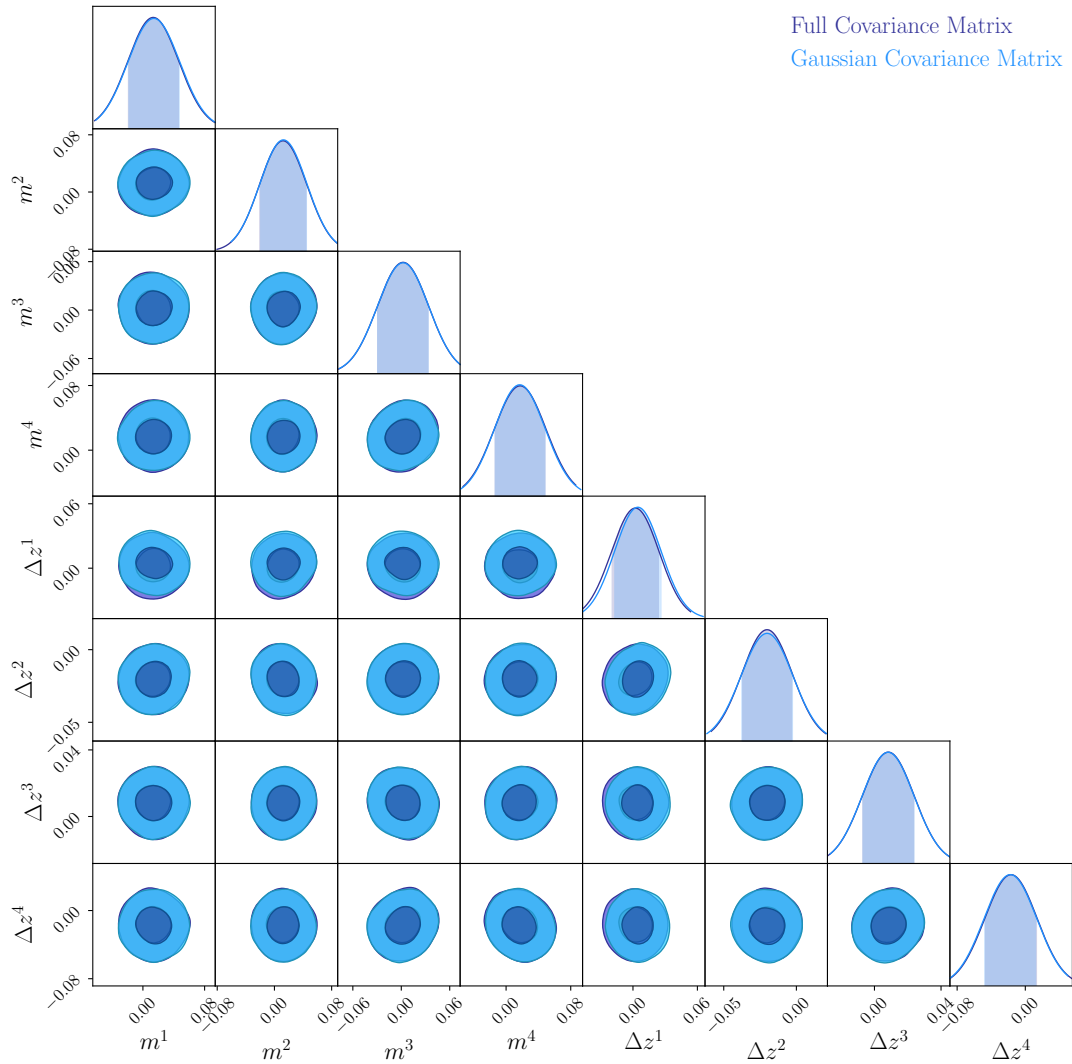
Figure 5.2: Constraints on systematic parameters for two covariance matrices produced for cosmic shear. The purple curve is for the FCM while the blue is for the GCM.

orders of magnitude lower. The new set of eigenvalues are then used, along with the eigenvectors, to obtain a modified covariance matrix.

We use this procedure to discard 200 such modes, and thus "reduce" the covariance matrix to about 10% of its original size. The results for the cosmological analysis with this new covariance matrix are shown in Figure 5.3. The loss in

constraining power for two of the three parameters in the plots is consistent when considering that 90% of the information held in the covariance matrix was removed. In fact, constraints on $S_8$ for the FCM are $0.779^{+0.044}_{-0.46}$, whereas, for the new covariance matrix, we obtain $0.725^{+0.076}_{-0.083}$, showing an increase in the errors of almost 77%. This shows that, for a 90% compression, this method is unsuited to reproduce the original parameter constraints.
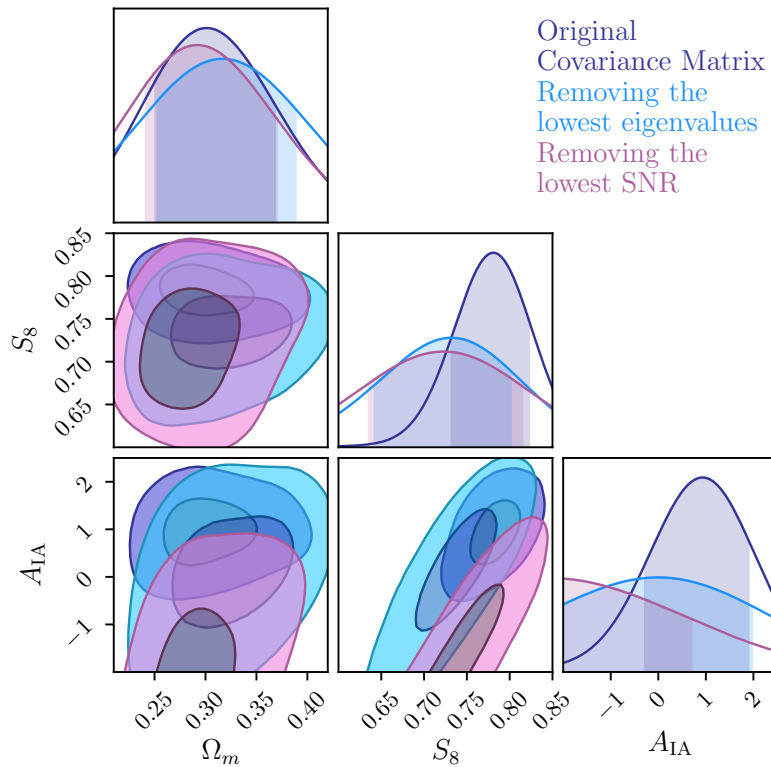


Figure 5.3: Constraints on cosmological parameters $\Omega_m$, $S_8$ and the intrinsic alignment parameter $A_{\mathrm{IA}}$ for the original covariance matrix (in purple) and for the two new covariance matrices obtained in §5.2.2 (in blue) and §5.2.3 (in magenta).

### 5.2.3 Signal-to-noise ratio

This next method is more sophisticated than the previous one because instead of concentrating on the "noise" – or the eigenvalues of the covariance matrix – we assess the relevance of each mode by considering the signal as well. We can evaluate the signal-to-noise ratio (SNR) as

$$\left(\frac{S}{N}\right)^2 = T_i C_{ij}^{-1} T_j \; , \tag{5.1}$$

where $T_i$ is the predicted theoretical signal for the $i^{th}$ data point, given a fiducial cosmology, and $C$ is the covariance matrix. The repeated indices are summed in all cases throughout this chapter. Just as in the previous method, the first step is to diagonalise $C$. The SNR can then be written as a linear combination of the $T_i$s,

$$\left(\frac{S}{N}\right)^2 = \frac{v_i^2}{\lambda_i} \; , \tag{5.2}$$

where $\lambda_i$ are the eigenvalues of the covariance matrix, which is diagonalised with the unitary matrix $U$, and the eigenvectors are

$$v_i \equiv U_{ij}^t T_j \; , \tag{5.3}$$

with the superscript $t$ denoting the transpose. Our goal, for this case, is to discard the modes $v_i$ for which $(v^2/\lambda)_i$ is small. To do so while retaining a positive definite matrix, we increase the noise (or, alternatively, decrease the signal) of the 200 lowest modes by replacing them with values seven orders of magnitude lower. Next, we use these modified SNR values to obtain a new covariance matrix. We report the parameter constraints for this procedure in Figure 5.3, where we find that the results are similar to those obtained in §5.2.2. We see that, while the constraints for $\Omega_m$ fared slightly better for cuts in the SNR, as compared to cuts on

the eigenvalues, there was still considerable loss for the other two parameters. This therefore suggests that the modes removed did indeed carry significant information for these two parameters.

To understand the reason for the failure of our assumption, we consider what was meant by the "signal" for these modes. In our procedure, we only examined the amplitude of the data points, and not their shape, which are also relevant. We can see this more clearly when taking the SNR per parameter $p_\alpha$,

$$\left(\frac{\partial S/\partial p_\alpha}{N}\right)^2 = \frac{(\partial v_i/\partial p_\alpha)^2}{\lambda_i} \ . \tag{5.4}$$

Figure 5.4 further illustrates this by showing the normalised SNR per mode on the abscissa and the SNR for $\Omega_m$, $S_8$ and $A_{IA}$ on the ordinate. The 200 excluded modes are shown in the shaded region. From the figure we can see that for $S_8$ and more particularly for $A_{IA}$, many of the modes with high SNR were removed with our cuts, which was not the case for $\Omega_m$. This makes it clear that simply cutting on raw SNR can potentially result in a loss constraining power for parameters which are sensitive to lower SNR modes.

The authors in [148] found that, due to the skewness of the two-point functions, if we were to use Gaussian likelihoods to analyse them (as is usually the case), we would be likely to find lower amplitudes for the cosmic shear. This occurs due to the Gaussian being unable to accurately estimate the frequency at which the data takes values below their mean. This bias is often strongest in the modes with the highest SNR and, hence, if one wishes to continue using Gaussian likelihoods, one way to correct this effect is to remove these modes. Following their findings, we performed an analysis where we removed, instead of the lowest SNR modes, the 200 highest ones by replacing them with values several orders of magnitude lower. This modification yielded weaker constrains not only for $S_8$ and $A_{IA}$, but

also for $\Omega_m$. We believe that this divergence was due to the large quantity of modes removed for our analysis and does not, in any way, invalidate the findings of the aforementioned work.
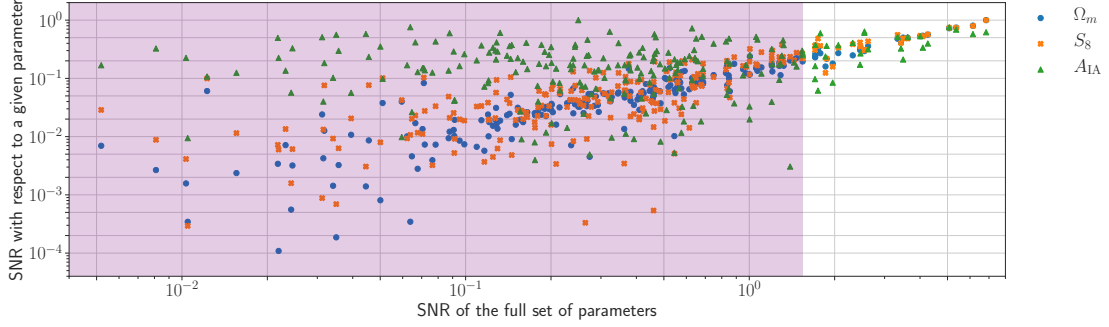


Figure 5.4: Scatter plot for the relation between the signal to noise (SNR) for each parameter (y-axis) against that for the full set of parameters (x-axis). The derivatives are shown with respect to $\Omega_m$ (blue circle), for $S_8$ (orange **x**) and for the intrinsic alignment parameter $A_{\mathrm{IA}}$ (green triangle). The purple rectangle spreads until the two hundred lowest values of SNR, which corresponds to the values that are modified for parameter constraints.

## 5.2.4 Tomographic Compression

The tomographic compression method of this section is based on a Karhunen-Loéve (KL) decomposition for the shear power spectrum suggested by [149] and later applied to real space two-point function in [150] for the CFHTLens survey. It finds the eigenmode, or, in our case, the linear combination of the convergence in different tomographic bins, with the highest SNR contribution to the power spectrum, then transforms its two-point function into real space. Since this method is dependent on the multipole $\ell$, it is not the most general compression scheme for two-point functions in real space. Nevertheless, the authors of [150] have shown that it is also valid for real space data.

We identify a mode as $b_{\ell m} = r_i \kappa^i_{\ell m}$, where $r_i$ is the weight factor on the $i^{\text{th}}$ tomographic bins. To find the linear transformation that captures as much information as possible in that mode, we start with the total power spectrum $\mathcal{C}_\ell$. We can decompose it into its signal and noise, $\mathcal{C}_\ell = S_\ell + N_\ell$, and use a general eigenvalue problem to find the KL-modes for each $\ell$,

$$\mathcal{C} e_p = \lambda_p N e_p \; , \tag{5.5}$$

where we have refrained from using the subscript. The index $p$ in $e_p$ corresponds to the $p^{th}$ KL-mode of $\mathcal{C}$. Applying the Cholesky decomposition for $N = LL^t$,

$$\mathcal{C} e_p = \lambda_p L L^t e_p \; , \tag{5.6}$$

and multiplying both sides by $L^{-1}$ from the left,

$$L^{-1} \mathcal{C} e_p = L^{-1} \lambda_p L L^t e_p \; ,$$
$$= \lambda_p L^t e_p \; . \tag{5.7}$$

Using $L^t L^{-t}$ on the left-hand side,

$$\left( L^{-1} \mathcal{C} \; L^{-t} \right) \left( L^t e_p \right) = \lambda_p \left( L^t e_p \right) \; , \tag{5.8}$$

which we recognise as a standard eigenvalue problem. We can further simplify by defining $\tilde{e}_p \equiv L^t e_p$:

$$\left( L^{-1} \mathcal{C} \; L^{-t} \right) \tilde{e}_p = \lambda_p \tilde{e}_p \; . \tag{5.9}$$

Solving for $\tilde{e}_p$, we can compute the transformed data vector as $b_p = \tilde{e}_p^t L^{-1} \kappa$. We also find that $E_\ell = [e_1, e_2, \cdots]^t$ is a transformation of basis so that the shear signal is diagonalised. The transformed power spectrum $\mathcal{D}_\ell$ can be calculated for the new

uncorrelated observable $b_{\ell m}$,

$$\mathcal{D}_\ell = \langle b_{\ell m} b_{\ell m}^t \rangle \ ,$$

$$= E_\ell^t L L^{-1} \, \mathcal{C}_\ell \, L^{-t} L^t E_\ell \ , \qquad (5.10)$$

$$= \Lambda_\ell \ ,$$

where $\Lambda_\ell = \mathrm{diag}[\lambda_1, \lambda_2, \cdots]$. If we denote $E_\ell N^{-1}$ as $R_\ell$ and further write $U_\ell^{ij} = R_\ell^i R_\ell^j$, where $i$ and $j$ are the indices for the tomographic bin-pairs, we have the compression in terms of one simple linear combination,

$$\mathcal{D}_\ell = R_\ell^i \, \mathcal{C}_\ell^{ij} R_\ell^j \ ,$$

$$= U_\ell^{ij} \mathcal{C}_\ell^{ij} \ , \qquad (5.11)$$

with $U_\ell^{ij}$ being the weight we will use to compress the two-point functions. We note that these KL-modes $b_{\ell m}^p$ are uncorrelated, so that their power spectrum $\mathcal{D}_\ell^{pp'}$ is a diagonal matrix whose entries are 1+SNR of the corresponding eigenmodes. This allows us to compress ten tomographic bin-pairs to one, or two, by taking only the modes with the highest SNR.

We want, however, to eventually compress the two-point function data vector of DESY1, which is measured in the real space tomographic bin pair $i, j$ and related to the angular power spectrum $\mathcal{C}_\ell$ via

$$\xi_+^{ij}(\theta) = \int \frac{\ell d\ell}{2\pi} J_0(\ell\theta) \mathcal{C}^{ij}(\ell) \ ,$$

$$\xi_-^{ij}(\theta) = \int \frac{\ell d\ell}{2\pi} J_4(\ell\theta) \mathcal{C}^{ij}(\ell) \ . \qquad (5.12)$$

To use linear combinations of all the tomographic bins, we need to ensure that the combination is $\ell$-independent, that is, the transformed two-point correlation

function, $\tilde{\xi}_\pm(\theta)$, can be directly computed from other two-point functions. In fact, Figure 5.6 shows that the $U^{ij}(\ell)$ are generally $\ell$-independent, except for low $\ell$s which can be attributed to the existence of cosmic variance. Therefore, we have

$$
\begin{aligned}
\tilde{\xi}_\pm(\theta) &= \int \frac{\ell d\ell}{2\pi} J_{0/4}(\ell\theta) \mathcal{D}(\ell) \ , \\
&= \int \frac{\ell d\ell}{2\pi} J_{0/4}(\ell\theta) U_\ell^{ij} \mathcal{C}^{ij}(\ell) \ , \\
&= \bar{U}^{ij} \xi_\pm^{ij}(\theta) \ ,
\end{aligned}
\tag{5.13}
$$

where $\bar{U}^{ij}$ is the average $U_\ell^{ij}$ given by

$$
\bar{U}^{ij} = \frac{\int_{\ell_{\min}}^{\ell_{\max}} d\ell \ (2\ell + 1) U_\ell^{ij}}{\int_{\ell_{\min}}^{\ell_{\max}} d\ell \ (2\ell + 1)} \ .
\tag{5.14}
$$

For the purposes of exploring the KL-transform, we make a more conservative angular cut than the one discussed in [131], making sure that both $\xi_\pm(\theta)$ are uniform in regard to tomographic combinations. We consider an angular scale for $\xi_+$ from $7.195'$ to $250.0'$, and for $\xi_-$ from $90.579'$ to $250.0'$. Therefore, the raw data vector has a length of 190. By shrinking 10 tomographic combinations for each angle into 1 KL-mode, the data vector is reduced to length 19, and so the number of elements in the covariance matrices has a compression of 99%. With `CosmoSIS`, we calculate the shear angular power spectrum $\mathcal{C}_\ell$ of the convergence $\kappa^i$, where $i = [1, 4]$ for the 4 tomographic bins probed by DESY1 with a fiducial cosmology at the best-fit parameters. We thus have $4 \times 5/2 = 10$ pairs of bins for which we can compute spectra.

The left plot in Figure 5.5 shows the diagonal elements of the signal part, $S_\ell$, and of the noise part, $N_\ell$, of the spectrum. The right-hand panel shows the SNR for the KL-transformed eigenmodes, that we call $D_\ell$, ranging from $\ell = 10$ to $\ell = 2500$.
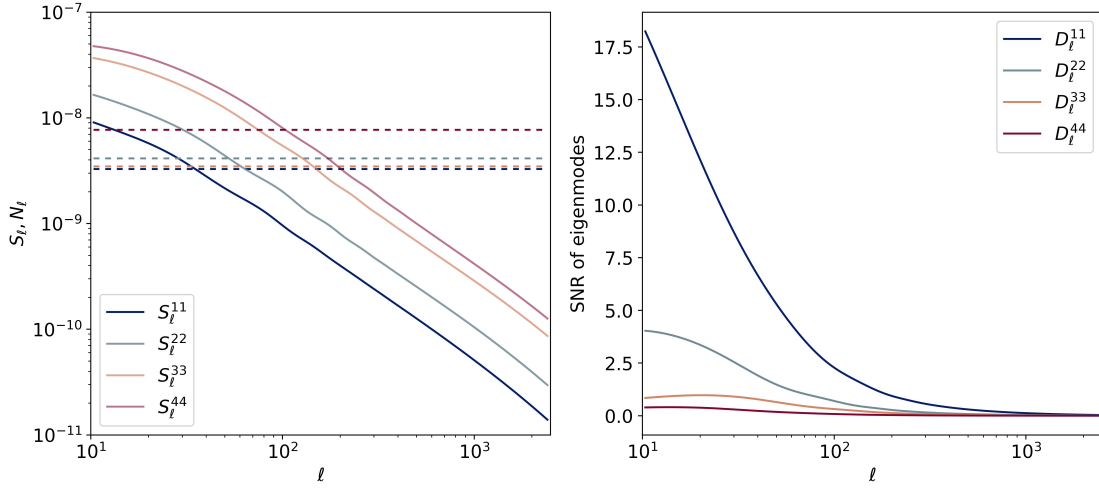
Figure 5.5: **Left:** Shear power spectrum of the FCM. Solid lines are diagonal elements of the signal matrix $S_\ell$, and dashed lines are the diagonal elements of noise matrix $N_\ell$. **Right:** Signal-to-noise ratio matrix $D_\ell$ of the first to fourth KL-modes of the power spectrum on the left.

We can see from the figure that the first KL mode contains most of the SNR contribution to the power spectrum, as expected. To recover more information, we would need to include the second and the cross mode between the first and second KL-mode.

In Figure 5.6, we plot the normalised KL-eigenmode $e_\ell^p N^{-\frac{1}{2}}$ and its corresponding weight, $U_\ell^{ij}$. Modes with increasing $\ell$ are plotted in increasing opacity of the colour. The KL-modes are found to be only weakly sensitive to $\ell$ and, as it increases, they converge to their weighted average, which are represented by the dashed black lines. For the first KL-mode, the tomographic bins with higher redshift contribute more to the SNR than those with low redshift. This is also true in the right panel, as seen for the tomographic combination of bins 3 and 4. This is consistent with the fact that low-redshift galaxies are less affected by lensing than high-redshift galaxies, as indicated in the left panel of Figure 5.5.
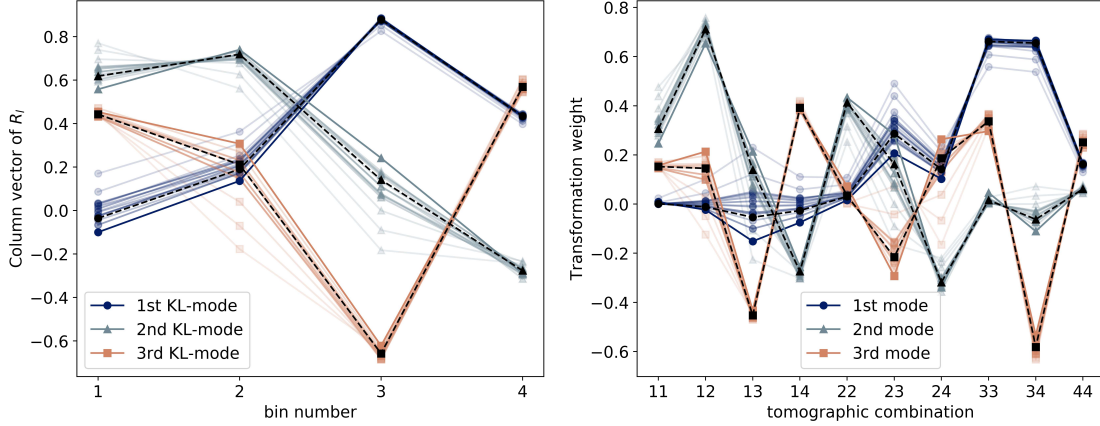
Figure 5.6: **Left:** Column vectors of the matrix $R_\ell$, or $e_\ell^p N^{-\frac{1}{2}}$, for compressing the shear power spectrum $\mathcal{C}_\ell$. **Right:** Transformation on tomographic bin combination $U_{ij}$ constructed from the KL-eigenmodes. For both plots, the dashed black lines are the weighted average of each mode. The lightest shade represents $\ell = 10$ and the increment is $\Delta\ell = 10$ for each darker shade.

We ran the likelihood analysis as detailed in §5.2.1 with the first KL-mode and the first two KL-modes with their cross-correlation mode, which correspond to a 10-to-1 and 10-to-3 compression, respectively, and show the parameter constraints on the $\Omega_m - S_8 - A_{\mathrm{IA}}$ plane in Figure 5.7. We do not include the third and fourth KL mode because they contain considerably less SNR. We can see that the first KL-mode is generally not sufficient to recover the information in the data vector. Since the first two modes contain most of the SNR contribution at a map level, we were able to recover the $\Omega_m$ constraints. However, information about the $S_8 - A_{\mathrm{IA}}$ combination is clearly lost. This could be due to the fact that the SNR-prioritised modes are not the sensitive direction for these parameters, as was also the case in Figure 5.4. Indeed, the $S_8 - A_{\mathrm{IA}}$ plane shows a strong correlation between these two parameters. This likely explains why the constraints for $S_8$ widened: the KL-modes fail to break the degeneracy on $A_{\mathrm{IA}}$, which is mostly present in the modes that are insensitive to cosmic shear and are discarded in the compression process.
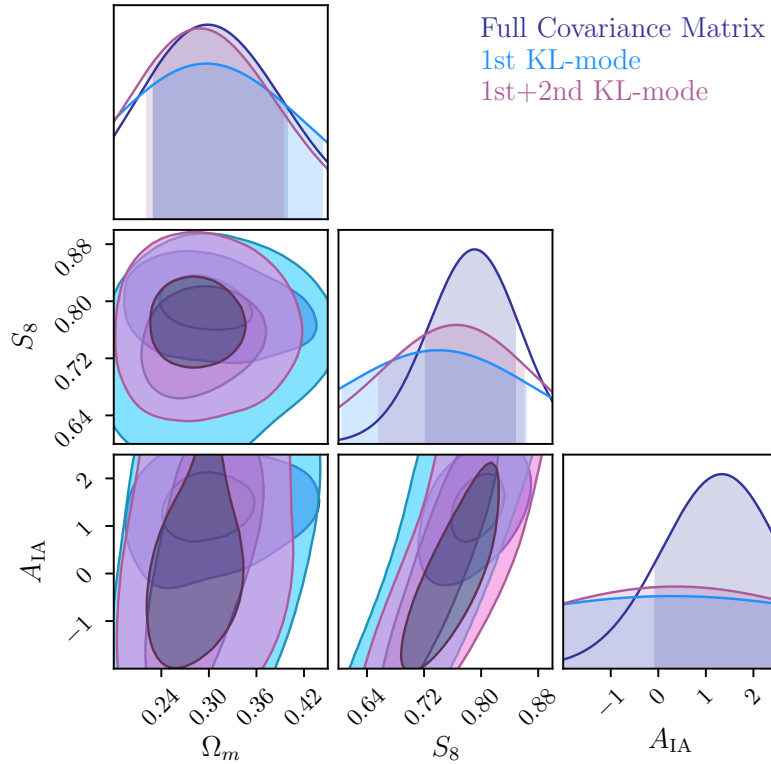
Figure 5.7: Cosmological constraints marginalised over all 16 parameters for the 190 ×
190 the FCM and that compressed using the first KL-mode and the first
two KL-modes.

## 5.2.5 Applying MOPED

We use the Massively Optimised Parameter Estimation and Data compression
(MOPED) [151] to shrink the data vector at the two-point level by using linear
combinations of the many two-point functions. MOPED has been shown to work
remarkably well in the case of Gaussian data, where only the mean depends on the
parameters. When these circumstances are met, the method is said to be lossless
in the sense that there is no loss of precision in the parameter constraints [152].
This compression scheme has been used in literature for a variety of applications,
for example, CMB data [153], the redshift-space galaxy power spectrum and bis-

pectrum [154], parameter-dependent covariance matrices [155], compression of the Planck 2015 temperature likelihood [156], weak lensing and galaxy clustering [157] and has been paired with a Gaussian Process emulator to analyse weak lensing data [158].

In principle, we only require $N_p$ linear combinations of the two-point functions, where $N_p$ is the number of free parameters, and each mode, or linear combination, contains all the information necessary about the parameter of interest.

We begin with a dataset represented by the vector $D = (D_1, D_2, ..., D_n)$ with probability distribution $L(D; p)$, where $p = (p_1, p_2, ..., p_N)$ is a vector of the model parameters. The logarithm of the probability distribution, $\mathcal{L} = \ln L$; its first derivative, $\mathcal{L}_{,i}$, known as the score function, tells how sensitive the model is with respect to the parameters. Its second derivative, the Hessian matrix,

$$H_{ij} = \mathcal{L}_{,ij} \; , \tag{5.15}$$

describes the correlation of the estimated values of $p_i$ and $p_j$. The expectation value of the negative of the Hessian, $F_{ij} = -\langle H_{ij} \rangle$, gives us the Fisher information matrix. To obtain a compression scheme capable of retaining the highest amount of information, we seek to maximise $F_{ij}$; to do so, we take the log-likelihood function for a Gaussian probability distribution,[3]

$$2\mathcal{L} = \ln \det C + (D - T)^t C^{-1} (D - T) \; , \tag{5.16}$$

with both the covariance matrix, $C = \langle (D - T)(D - T)^t \rangle$, and $T = \langle D \rangle$ dependent of the model parameters $p$. We also define the data matrix as

$$\mathrm{x} \equiv (D - T)(D - T)^t \; . \tag{5.17}$$

---

[3] We have dropped the additive constant $n\ln(2\pi)$.

Combining this definition with $\ln \det C = \text{Tr}\left[\ln C\right]$, we can express Eq. (5.16) in a simpler form,

$$2\mathcal{L} = \text{Tr}\left[\ln C + C^{-1}\mathbf{x}\right] . \tag{5.18}$$

Derivating for $p_i$ and $p_j$, we find the quantity we wish to maximise:

$$\langle \mathcal{L}_{,ij} \rangle = \frac{1}{2}\text{Tr}\left[C^{-1}C_{,i}C^{-1}C_{,j} + C^{-1}M_{ij}\right] , \tag{5.19}$$

where $M_{ij} = T_{,i}T_{,j}^t + T_{,j}T_{,i}^t$.

There are three ways one can proceed from here, with respect to the dependence on the model parameters: 1) the more general case, where both the mean and the covariance depend on the model parameters; 2) only the covariance has a dependence, in which case the second term vanishes; and 3) only the mean is dependent, and the first term vanishes. The general case has been tackled by [159], where they use the score function to derive $n$ compressed statistics of the data. The second case often reduces to the tomographic compression described in the previous subsection. Finally, the third case is the basis for MOPED [160, 151], which uses linear compression to radically reduce the dataset and covariance matrix. Here, we will only be working with the latter, such that Eq. (5.19) reduces to

$$F_{ij} = \langle \mathcal{L}_{,ij} \rangle = \frac{1}{2}\text{Tr}\left[C^{-1}M_{ij}\right] . \tag{5.20}$$

For the simplest case of only one parameter, we have

$$F_{11} = T_{,1}^t C^{-1} T_{,1} . \tag{5.21}$$

If we apply a compression of the type $y = U^t D$, we can follow these same steps to

obtain the compressed Fisher matrix,

$$F_{11}^{\text{comp}} = \frac{U^t M_{11} U}{U^t C U} \ .$$
(5.22)

To find an extremum such that $U^t C U = 1$, we apply a Lagrange multiplier,

$$M_{11} U = \lambda C U \ .$$
(5.23)

If we use a Cholesky decomposition for $C = LL^t$, then

$$\left( L^{-1} M_{11} L^{-t} \right) \left( L^t U \right) = \lambda \left( L^t U \right) \ ,$$

$$2 \left( L^{-1} T_{,1} \right) \left( T_{,1}^t U \right) = \lambda \left( L^t U \right) \ .$$
(5.24)

Since the lhs always points in the direction of $(L^{-1} T_{,1})$, then the only non-trivial solution is,

$$U = C^{-1} T_{,1} \ .$$
(5.25)

Plugging this back in Eq. (5.22), we find

$$F_{11}^{\text{comp}} = T_{,1}^t C^{-1} T_{,1} = F_{11} \ ,$$
(5.26)

which shows that the Fisher matrix is unchanged.

This can be further extended to multiple parameters, such that,

$$U_{\alpha i} \equiv \frac{\partial T_j}{\partial p_\alpha} C^{-1}{}_{ji}$$
(5.27)

and

$$y_\alpha = U_{\alpha i} D_i \ ,$$
(5.28)

for each parameter $p_\alpha$. The now much smaller data set $\{y_\alpha\}$, which contains $N_p$

data points, carries its own $N_p \times N_p$ covariance matrix, from which $\chi^2$ can be computed for each point in parameter space. Propagating through shows that this covariance matrix is related to the original $C_{ij}$ via

$$C_{\alpha\beta} = U_{\alpha i} C_{ij} U_{j\beta} \; . \tag{5.29}$$

An illustration of the matrix $U$ is shown in Figure 5.8, showing the weighting vector for parameters $\Omega_m$, $S_8$ and $A_{\mathrm{IA}}$.
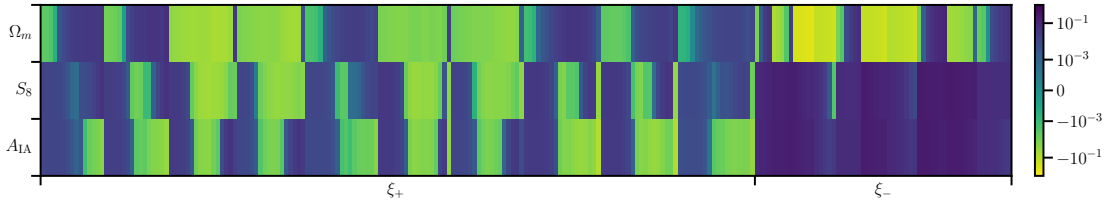


Figure 5.8: An illustration of the 227 values of the weights corresponding to $\Omega_m$, $S_8$ and $A_{\mathrm{IA}}$ used for compressing the covariance matrices. Note the similarity of the weighting vectors for $S_8$ and $A_{\mathrm{IA}}$, and that the largest values correspond to the last 60 elements, i.e. those that we will use to compress the part of the covariance matrix that holds information for $\xi_-$.

This compression was first suggested by [152] for a single parameter only. The non-trivial extension to multiple parameters, where the full Fisher matrix is reproduced with the compressed data, is the MOPED algorithm [151]. One difference here is that our weighing vector given by Eq. (5.27) does not carry the normalising factor of Eq. (11) of [151]. In our case, the covariance matrix is $227 \times 227$, while the number of parameters needed to specify the model is only 16, so $C_{\alpha\beta}$ is a $16 \times 16$ matrix. We have apparently captured from the initial set of $(227 \times 228)/2 = 25{,}878$ independent elements of the covariance matrix a small subset (only 136) of linear combinations of these 26k elements that really matter. If two covariance matrices give the same set of $C_{\alpha\beta}$, it should not matter whether any of the other thousands

of elements differ from one another.

To use MOPED as described here, we have assumed a Gaussian likelihood and that the fiducial value at which the derivatives are taken are those at the maximum likelihood point. If one does not have prior knowledge of this value, then one could iterate to find it but, as [151] have found, this is often unnecessary. We also trust that the cosmological model we have chosen is the correct one; deviations from a baseline cosmological model can be accounted for by introducing additional weighing vectors, as described in [161].
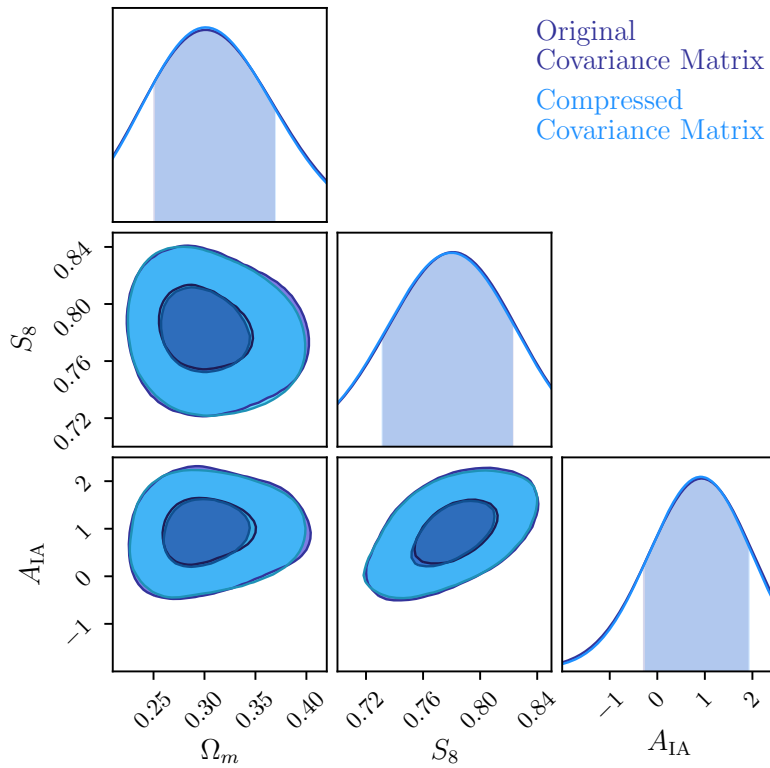


Figure 5.9: Constraints on cosmological parameters $\Omega_m$ and $S_8$ and for the intrinsic alignment parameter $A_{\mathrm{IA}}$ for the original covariance matrix, FCM, (in purple) and for the compressed one (in blue).

Figure 5.9 compares the constraints obtained for the compressed covariance matrix and data set with results from the full one. The two curves agree extremely

well for the three parameters shown. This is also true for all the other cosmological and intrinsic alignment parameters, where their mean values agree at the $1\sigma$ confidence level. While the volume of the whole constrained parameter space does increase by about 13%, the constraints for most parameters are less than 4% broader, which shows that the information loss is negligible.

## 5.3 Comparison of Covariance Matrices

Since the data vector and all the analyses settings are the same, it must follow that the parts of the covariance that are relevant to parameter constraints be similar to each other. Establishing which regions of the covariance matrix are most informative is the first step towards building a tool for comparing these matrices without the need for a full cosmological analysis.

In the previous section, we have seen that, out of the four compression schemes analysed here, MOPED was the only one capable of retaining the required information about the parameters in a compressed covariance matrix. Our compressed covariance matrix comparison therefore uses the MOPED algorithm.

### 5.3.1 Element-by-element Comparison

We begin by performing an element-by-element comparison between the two covariance matrices, the GCM and the FCM, described in §5.2.1. If there were only a single data point, then the covariance matrix would be one number and comparing them to try to understand why they give different constraints would be as simple as evaluating these two numbers. The simplest generalization is then to do an element-by-element comparison. We make a scatter plot of the elements of the two matrices in the bottom panel of Figure 5.10, where we can see that the elements of the FCM are, in general, larger than the GCM's, with many of the

off-diagonal elements differing by 2 orders of magnitude or more. In some ways, this is useful and reassuring, as it aligns with what we see in the parameter constraints, in Figures 5.1 and 5.2: larger elements in the covariance matrix translates to less constraining power.

The limitation of this method is that it remains unclear which of the differences are responsible for the final discrepancies in parameter constraints. This difficulty is an outgrowth of the increasing size of the data sets and hence the growing number of elements of the covariance matrix that any two codes are likely to disagree on. This element-by-element comparison, however, would prove much more practical if we had fewer elements to compare. Towards that end, we turn to compressed covariance matrices.

## 5.3.2 Compressed Matrices Comparison

We compress both covariance matrices using the same $U_{\alpha,i}$ (we also tried using different $U$'s for each and obtained similar results).

Figure 5.11 shows a one-to-one scatter plot of the compressed elements, which, as expected, exhibits a similar behaviour to that observed in Figure 5.10, with the elements of the FCM being larger than those of the GCM. Here, however, the ratio of the diagonal elements is closer to 1, with a fractional difference of up to 17%, as compared to 26% with the original matrices. Perhaps even more importantly, there are much fewer points on this plot, since MOPED reduces the number of elements that need to be compared. These figures provide a greater insight into the relevant elements for parameter estimation: the dispersion is largely damped, and most of the elements are within 25% of each other, which explains what we see in the parameter constraints. Figure 5.12 shows the correlation matrix for the GCM and the FCM, and the difference between the normalised off-diagonal elements. The small differences suggest that the root of the slightly looser constraints obtained

with the GCM is the larger diagonal elements of the MOPED-reduced covariance matrix. Hence, a problem that initially required inspecting hundreds of thousands of elements is reduced to involving only 16 of them.

## 5.4 Tolerance of the Compressed Matrices

Now that we have shown that we are indeed able to compress the covariance matrix into a much simpler and considerably smaller one, our next step is to analyse the amount of error the elements can tolerate while reproducing compatible parameter constraints.

In the next two sections we test two different ways of perturbing the covariance matrix: first we consider an error to the elements themselves, then we follow a similar procedure to study the effects of introducing an error to the eigenvalues of the compressed covariance matrix. In both cases the perturbation is drawn in the following manner: consider that we want to test the impact of an error $x\%$, this can either be an increase or a decrease in the original element (or eigenvalue), as what we care about most is not whether the parameter constraints will be larger, but rather how different they are. For this error to be random, but centred at our desired percentage, we draw a $\delta$, for each new element/eigenvalue, from a Gaussian distribution, $\mathcal{G}(0, \frac{x}{100})$ and calculate the new value to be

$$C_{\alpha\beta}^{\text{new}} = (1 + \delta)C_{\alpha\beta}^{\text{old}} \; , \tag{5.30}$$

where, for the eigenvalue, we replace $C_{\alpha\beta}$ with $\lambda_i$. This analysis is done only for the FCM, with errors ranging from $5 - 45\%$, and for 50 realizations of the perturbed matrices.

One of the concerns that arises when modifying the covariance matrix is that the resulting one has to be positive definite (PD). For this reason, in each section we

also describe the steps taken to ensure this. Another intelligent way of guaranteeing that the matrix is PD would be to perturb the log of the covariance matrix. The issue, however, is how to introduce an error to the log matrix that would be similar to what we expect to see in the original covariance matrix. In

$$C_{\alpha\beta}^{\mathrm{new}} = e^{(1+\delta)(\log\ C^{\mathrm{old}})_{\alpha\beta}} \ , \tag{5.31}$$

the value of $C_{\alpha\beta}^{\mathrm{new}}$ is not necessarily within $\delta\%$ of $C_{\alpha\beta}^{\mathrm{old}}$. Introducing a 10% error, for example, in such a matrix, results in a perturbed covariance matrix with some of its elements differing by several orders of magnitude from the original one. A safer procedure would then be to perturb the log of its eigenvalues, but, since we have a section dedicated to perturbations to the eigenvalues themselves, we deemed this would be repetitive.

### 5.4.1 Modifying the elements

Once we generate new values for each independent element, following Eq. (5.30), we check for positive definiteness. Since the resulting matrix is, more often than not, non-PD, we correct this by identifying the smallest negative eigenvalue and adding it to the diagonal [162]. We check that, although doing this largely increases the values of the diagonal elements, less than 40% have a standard deviation of more than twice the original perturbation.

The constraints for $\Omega_m$, $S_8$ and $A_{\mathrm{IA}}$ are shown in Figure 5.13, in purple, where the blue rectangle spans over the constraints for the unchanged compressed covariance matrix. The relative change in size for the 68% CL interval is mostly $> 10\%$ for the cosmological parameters. On the other hand, for the intrinsic alignment parameter $A$, the mean values are more than $1\sigma$ away from the original one and the loss in constraining power goes up to $\sim 30\%$.

### 5.4.2 Modifying the eigenvalues

Another way of introducing error to the covariance matrix is to perturb its eigenvalues. For a symmetric matrix, we have

$$C = Q \Lambda Q^{-1} \, , \tag{5.32}$$

where $\Lambda = \lambda I$, with $\lambda$ being the eigenvalues and $I$ the identity matrix; and $Q$ is a square matrix whose columns are composed of the eigenvectors of $C_{\alpha\beta}$. The eigenvalues are then perturbed as described in Eq. (5.30), and the error, $\delta$ is drawn from $\mathcal{G}(0, \frac{x}{100})$, with the requirement that $|\delta| < 1$. We then have $\lambda^{\mathrm{new}} > 0$, and thus the perturbed covariance matrix associated with these new eigenvalues is PD.

The results for this method are also plotted in Figure 5.13, in green. Despite the results following the same tendency as those of the last section, we find that about 80% of the elements of the perturbed covariance matrices are within 10% of their original value.

## 5.5 Conclusion

In this work, we set out to explore different ways of compressing, comparing and analysing covariance matrices, while giving particular emphasis to the MOPED compression scheme. We started by looking at the parameter constraints of two $227 \times 227$ covariance matrices, the FCM and the GCM, generated for DESY1 cosmic shear measurements, and saw that, although some of their elements differed by several orders of magnitude, they generated similar constraints. It was clear, then, that not all elements contribute equally to the parameter constraints, and we needed to employ increasingly complicated methods to try and locate the most relevant parts of the covariance matrix.

The first step was then to analyse the eigenvalues. We began with the hypothesis that modes associated with the highest eigenvalues carry most information, as such, those with the lowest eigenvalues would contribute less to parameter estimation. Using this notion to compress the covariance matrix we "removed" the lowest 200 eigenvalues, by setting them to several orders of magnitude lower. While the loss in constraining power for $\Omega_m$ was only around 20%, we saw a loss of about 77% in the size of the constraints for $S_8$, and more than 100% for $A_{\mathrm{IA}}$. Next, we moved on to the SNR, and, using a similar procedure adopted for the eigenvalues, we "removed" the modes with the lowest SNR. The results were similar to those obtained with the eigenvalue cuts and showed us that these modes did not contribute significantly to constraining some cosmological parameters, like $\Omega_m$, however constraints on the IA parameters, and even $S_8$ were more affected. This is consistent with the fact that the IA parameters are more sensitive to low SNR scales in cosmic shear, and it shows us that we need to look at the SNR per parameter before making any cuts, so that we do not lose important information for the parameters that we want to constrain.

The next step was to shrink the covariance matrix by applying a tomographic compression, where we decompose the shear angular power spectrum into KL modes, then we look for modes with the highest SNR and compress the shear data vector with these modes. We thus go from ten tomographic bin combinations to only one or two. The resulting covariance matrix, for one mode, is then reduced from $190 \times 190$ to $19 \times 19$ or $59 \times 59$, showing a reduction of about 99% or 91%, respectively. We show, however, that one mode is not sufficient for constraining the parameters of our model, with the results being similar to our previous tests involving SNR: the constraints for $\Omega_m$, for example, are reproduced with the first and second KL-mode, but this is not the case for the IA parameters. Since essential information of IA parameters is contained in low SNR KL-mode, the high KL-

modes failed to break the degeneracy of $A_{IA} - S_8$ correlation, resulting in wider $S_8$ constraints.

Finally, we applied MOPED, which uses linear combinations of the data vector. By transforming the data vector and covariance matrix with a weighting vector that is parameter dependent, we were able to reduce the $227 \times 227$ matrix to a $16 \times 16$ matrix. We show that the cosmological analysis using this compressed matrix reproduced similar constraints to the DESY1 analysis, for an uncompressed covariance matrix. We also performed a comparison of the elements of the compressed covariance matrix for the FCM and the GCM and found that the new elements show reasonable agreement, with their correlation matrices being very similar, and the diagonal elements showing a percentage difference of less than 15%.

Given these results, we successfully show that MOPED is the only compression scheme, out of the ones considered in this work, capable of capturing all the relevant information required to reproduce reliable parameter constraints for the 16 parameters of interest. It is worth noting here that compression does not automatically speed up the computation for parameter inference if the projection to form the MOPED coefficients is done at each sampled point. For speed gains, a way to compute the theoretical MOPED coefficients rapidly needs to be used, for e.g. by using Gaussian Processes to generate the compressed theory [158].

When looking at the one-to-one element comparison of the FCM and the GCM, in Figure 5.10, the region of large variance suggests that there could be considerable differences in the parameter constraints. We see, however, in Figures 5.1 and 5.2, that this is not the case. This becomes clearer when comparing the elements of the compressed covariance matrices, where, while they do follow the same tendency as the full comparison, only a smaller portion of the elements display a greater dispersion. In this sense, one of our most important results is in the ability of

using MOPED to compare different matrices.

One last step was taken to analyse the error tolerance of the compressed FCM. We adopted two ways of doing this, by introducing error taken from a Gaussian distribution for $5 - 45\%$ of the original 1) element and 2) eigenvalue of the compressed covariance matrix. For the latter, we checked that only about 20% of elements of the resulting, perturbed, covariance matrix showed errors within the expected value, while the vast majority had only about a 10% error. In both cases, however, the results were similar: for the cosmological parameters $\Omega_m$ and $S_8$, the $2\sigma$ constraints changed by about 7%, on average, while for the IA parameter $A_{\mathrm{IA}}$, the constraints were up to 30% larger. Finally, we highlight the increasing shift, in the mean values of $A_{\mathrm{IA}}$, to about 32% smaller than those obtained with the uncompressed FCM; while for the cosmological parameters this was only about 5%, in general.
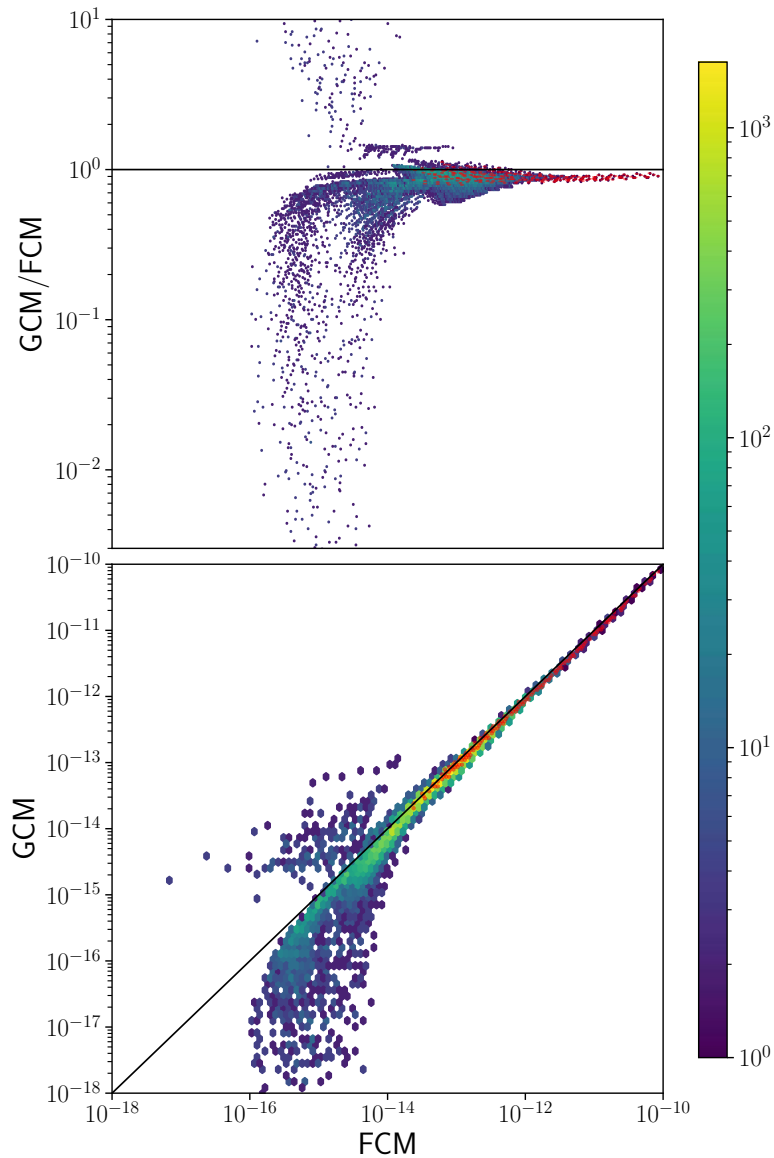
Figure 5.10: In both plots, the red points refer to the diagonal elements, and the color bar varies according to the number of elements in one hexagonal bin, where the darkest blue color corresponds to only one element, and the brightest yellow shade to 2000. **Top:** Scatter plot of the ratio of the elements of the GCM and the FCM vs the FCM value. For illustrative purposes, we draw a black, horizontal line at GCM/FCM = 1. **Bottom:** Density of the scatter plot of the positive elements of the GCM and the FCM, with the black line showing FCM = GCM.
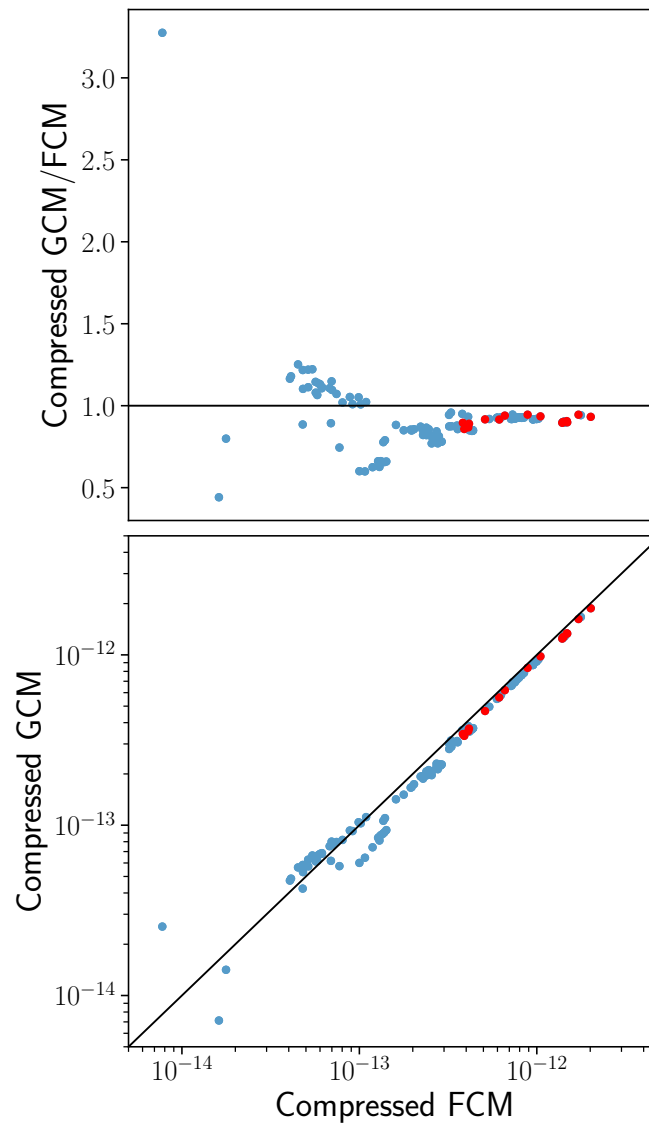
Figure 5.11: Results for the covariance matrices compressed following the procedure described in §5.2.5, with the red points corresponding to the diagonal elements. **Top:** One-to-one scatter of the ratio of the elements of the GCM and the FCM, over elements of the FCM. The black horizontal line is drawn at GCM/FCM = 1. **Bottom:** One-to-one scatter of the elements of the compressed matrices, with the black line describing FCM = GCM.
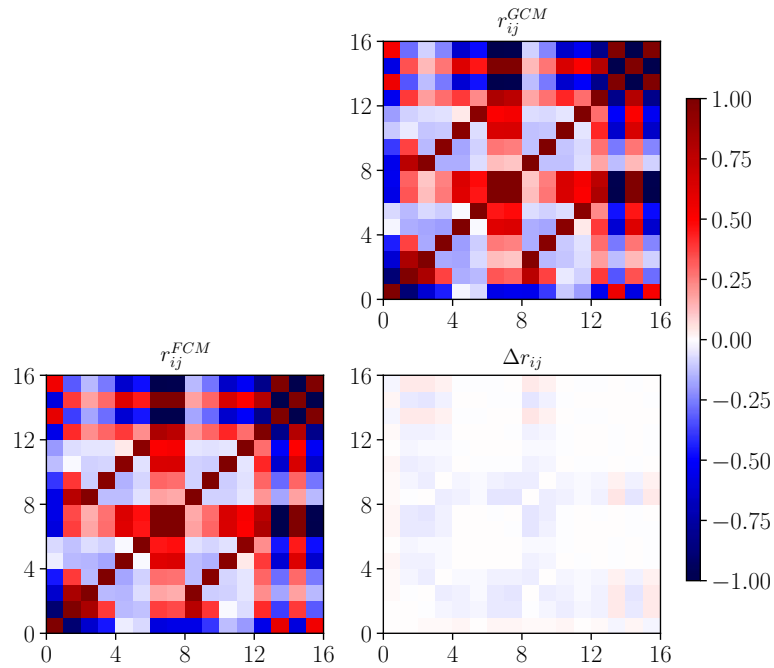
Figure 5.12: The upper right and lower left plots display the correlation matrix for the GCM and the FCM respectively, and the difference between them, $\Delta r_{ij}$, is shown on the lower right.
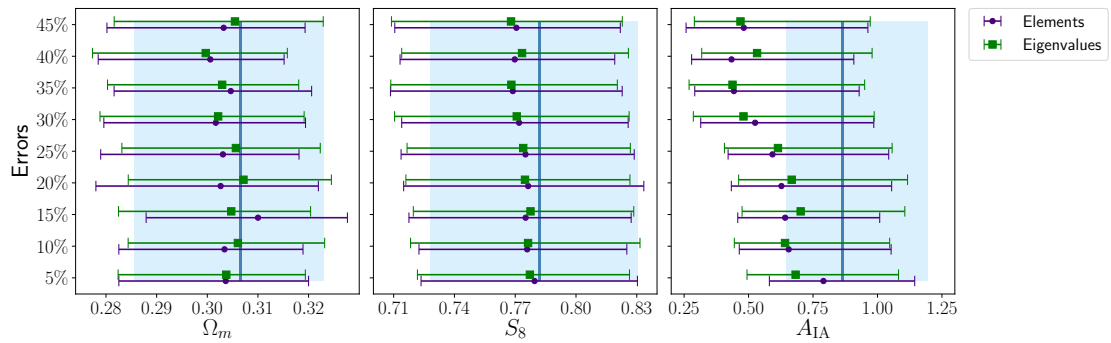


Figure 5.13: An error plot showing the changes to the constraints for $\Omega_m$, $S_8$ and $A_{\mathrm{IA}}$ for errors added at $5\%, 10\%, 15\%, 25\%, 30\%, 35\%, 40\%$ and $45\%$ of the original elements (in purple) and eigenvalues (in green) of the compressed covariance matrix. The blue rectangle covers the $68\%$ CL interval obtained for the FCM, and the darker blue vertical line shows the mean value for the respective parameter.

# A fast and reliable method for the comparison of covariance matrices

> How are you holding up? Because I'm a potato.
>
> Portal 2

In this chapter I will detail the work I did in collaboration with Valerio Marra, in [163].

## 6.1 Motivation

This is an exciting time for cosmology, as modern technological developments enable us to build telescopes capable of exploring almost the entire observable universe with unprecedented accuracy. As we brace ourselves for the large amount of data that will be made available in upcoming surveys like J-PAS,[1] LSST,[2]

---

[1] www.j-pas.org
[2] www.lsst.org

Euclid[3] and SKA,[4] we must prepare novel ways to process and extract as much information as possible from the data. This brings us to the issue of software development and validation (see, e.g., [164, 165]).

In the previous chapter we have discussed the issue of comparing covariance matrices, which, to this author's knowledge, is a problem yet unresolved. The most certain and forward way of comparing covariance matrices is in terms of their ability to reproduce cosmology, that is, by performing a full Bayesian analysis. This approach, however, can be very time consuming and computationally demanding.

We build upon the exciting results found in Chapter 5 to create a reliable method of comparison by using the compressed covariance matrices obtained with MOPED. Another aspect that will be discussed here is how to obtain the full covariance matrix from a compressed one. Since compressed covariance matrices are potentially faster to obtain analytically, we propose an invertible transformation capable of reproducing the full sized covariance matrix.

## 6.2 Compression Scheme

We use the compressed scheme described in §5.2.5. In this chapter, however, we change the notation to,

$$
\begin{aligned}
\text{Covariance matrix} &: \ C \to \mathbf{C} \ , \\
\text{Compression scheme} &: \ U \to \mathbf{b} \ .
\end{aligned}
\tag{6.1}
$$

### 6.2.1 Invertible Compression

We investigate an invertible "compression" scheme that, given a compressed covariance matrix, is capable of recreating a covariance matrix with the same length

---

[3]www.euclid-ec.org
[4]www.skatelescope.org

as the desired data vector. We also require that the recreated and compressed covariance matrices yield similar parameter constraints. For the transformation to be invertible, we do not reduce the size of the covariance matrix, but rather the number of relevant elements. We thus start with Eq. (5.25), and expand it to an invertible, $n \times n$ transformation matrix,

$$\mathbf{B} = (\mathbf{b} \quad U) \ , \tag{6.2}$$

where $U$ has dimension $(n-N) \times n$, and $\mathbf{b}$ is the usual $N \times n$ compression scheme, where $n$ is the length of the data vector and $N$ is the number of free parameters. We want to find $U$ such that the transformed covariance matrix, partitioned blockwise, is

$$\mathbf{C}^{\mathrm{trans}} = \mathbf{B}^t \mathbf{C} \mathbf{B} = \begin{pmatrix} \mathbf{b}^t \mathbf{C} \mathbf{b} & 0 \\ 0 & U \mathbf{C} U^t \end{pmatrix} \ , \tag{6.3}$$

which implies that

$$\mathbf{b}^t \mathbf{C} U = 0 \ . \tag{6.4}$$

For the above to be true, the rows of $U$ must be composed of vectors which form the nullspace of $\mathbf{b}^t \mathbf{C}$. To simplify notation, we write

$$\mathbf{C}^{\mathrm{trans}} = \begin{pmatrix} C1 & 0 \\ 0 & C3 \end{pmatrix} \ . \tag{6.5}$$

At first glance, it seems that we have produced a matrix $C3$ with $(n-N) \times (n-N)/2$ more relevant elements than the compressed one. As we will see in the next section, however, this is not the case. In fact, $C3$ is completely irrelevant to parameter constraints.

## 6.2.2 Toy example

Let us take a toy example to further illustrate the invertible transformation and how $C3$ influences $\mathbf{C}$. Consider the Gaussian data described by:

$$\{t_i, x_i\} \text{with} i = 1, 2, 3 \ ,$$

$$\mathbf{C} = \sigma^2 I_3 \ ,$$

(6.6)

where $I_3$ is the 3-d identity matrix, $t_i$ is the independent variable associated to $x_i$, and $\sigma$ is the error associated to $x_i$. Next, we propose the following model,

$$\mu(t) = \theta_1 + \theta_2 t \ ,$$

(6.7)

for which we can obtain the likelihood as

$$2\mathcal{L} = (x_i - \mu(t_i))\mathbf{C}_{ij}^{-1}(x_j - \mu(t_j)) \ ,$$

$$= \sum_{i=1,2,3} \frac{(x_i - \mu(t_i))^2}{\sigma^2} \ .$$

(6.8)

The next step is then to obtain an explicit expression for $\mathbf{b}$, $U$, $C1$ and $C3$ as a function of $t_i$, $x_i$, $\sigma$ and $\theta_i$. We start with

$$\mathbf{b} = \frac{1}{\sigma^2} \begin{pmatrix} 1 & 1 & 1 \\ t_1 & t_2 & t_3 \end{pmatrix}$$

(6.9)

and

$$U = \begin{pmatrix} \frac{t_2 - t_3}{t_1 - t_2} & \frac{t_3 - t_1}{t_1 - t_2} & 1 \end{pmatrix} \ ,$$

(6.10)

which we can use to find,

$$\mathbf{C}^{\text{trans}} = \begin{pmatrix} \frac{3}{\sigma^2} & \frac{t_1+t_2+t_3}{\sigma^2} & 0 \\ \frac{t_1+t_2+t_3}{\sigma^2} & \frac{t_1^2+t_2^2+t_3^2}{\sigma^2} & 0 \\ 0 & 0 & \mathbf{C3} \end{pmatrix} , \tag{6.11}$$

where

$$\mathbf{C3} = 2\sigma^2 \frac{t_1^2 + t_2^2 + t_3^2 - t_2 t_3 - t_1 (t_2 + t_3)}{(t_1 - t_2)^2} . \tag{6.12}$$

Plugging our values in Eq. (5.20), we get,

$$F_{ij}^{\text{trans}} = \frac{1}{\sigma^2} \begin{pmatrix} 3 & t_1 + t_2 + t_3 \\ t_1 + t_2 + t_3 & t_1^2 + t_2^2 + t_3^2 \end{pmatrix} = C1 . \tag{6.13}$$

Making $\mathbf{C3} = C3$, we can revert back the transformation to find $C'$. If we substitute $C'$ in Eq. (5.20), we find that $F' = F$, which shows that the Fisher matrix of the modified covariance matrix does not depend on $C3$.

### 6.2.3 Cosmic shear example

#### 6.2.3.1 The DESY1 data

We use the cosmic shear measurements from DESY1 detailed in §5.2.1. The cosmological parameter inference is also performed with `CosmoSIS`, with the same settings as the analyses of the previous chapter.

#### 6.2.3.2 The KiDS-1000 data

The measurements for the Kilo-Degree Survey 1000 (KiDS-1000, [4]) contain 1006 deg$^2$ of images, with the primary images taken in the $r$-band, but with the final

set having photometry in $ugriZYJHK_s$[5] [166], after being combined with infrared data from the VISTA Kilo-degree INfrared Galaxy survey (VIKING, [167]). The data is divided into five tomographic bins, based on their best-fitting photometric redshifts and ranging from $0.1 < z < 1.2$.

There are nine angular bins between 0.5 and 500 arcmin, resulting in a data vector of length 270. The angular cuts are applied to $\xi_-(\theta)$, removing scales with $\theta < 4$ arcmin [168], which leaves 135 data points for $\xi_+(\theta)$ and 90 for $\xi_-(\theta)$. The final dataset has length 225, with a $225 \times 225$ covariance matrix.

The analyses assume a flat $\Lambda$CDM model, with $w = -1$, and five free cosmological parameters, $\{S_8, \Omega_c h^2, \Omega_b h^2, h, n_s\}$. There are two astrophysical nuisance parameters: the baryon feedback parameter, $A_{\mathrm{bary}}$ and $A_{\mathrm{IA}}$, where, for analyses with this dataset, the latter does not carry a redshift dependence. The mean of the five redshift distributions also varies and are correlated through their covariance matrix. Finally, for $\xi_+(\theta)$, we have,

$$\delta_c = \pm\sqrt{c_1^2 + c_2^2} \,, \tag{6.14}$$

to account for the uncertainty of the additive ellipticity bias terms, $c_1$ and $c_2$, assuming that they are constants. Table 6.1 shows the free parameters along with their priors.

For parameter constraints, we use the `MultiNest` sampler within `CosmoSIS`, with the same settings described in the previous section, but with the KiDS Cosmology Analysis Pipeline, KCAP [4]. We use a modified likelihood to account for the transformed and compressed covariance matrices and data vectors.

---

[5]$u$: ultraviolet; $g$: green; $r$: red; $i, Z, Y, J, H$ and $K_s$: different bands in the near-infrared.

Table 6.1: List of the priors used in the analysis for parameter constraints using the dataset described in §6.2.3.2.

| Parameter | Prior |
|---|---|
| Cosmological | |
| $S_8$ | $\mathcal{U}(0.1, 1.3)$ |
| $\Omega_c h^2$ | $\mathcal{U}(0.051, 0.255)$ |
| $\Omega_b h^2$ | $\mathcal{U}(0.019, 0.026)$ |
| $h$ | $\mathcal{U}(0.64, 0.82)$ |
| $n_s$ | $\mathcal{U}(0.84, 1.1)$ |
| Astrophysical | |
| $A_{\mathrm{IA}}$ | $\mathcal{U}(-6, 6)$ |
| $A_{\mathrm{bary}}$ | $\mathcal{U}(2.0, 3.13)$ |
| Systematic | |
| $\delta_z^1$ | $\mathcal{G}(0, 1.0)$ |
| $\delta_z^2$ | $\mathcal{G}(-0.181, 1.0)$ |
| $\delta_z^3$ | $\mathcal{G}(-1.110, 1.0)$ |
| $\delta_z^4$ | $\mathcal{G}(-1.395, 1.0)$ |
| $\delta_z^5$ | $\mathcal{G}(1.265, 1.0)$ |
| $\delta_c$ | $\mathcal{G}(0, 2.3 \times 10^{-4})$ |

### 6.2.3.3 The covariance matrices

There are three distinct covariance matrices used in this work, which will be described in this section. What we refer to as the *DES Covariance Matrix* (DCM), throughout the text is the DESY1 cosmic shear covariance matrix of §5.2.1 (previously referred to as FCM). The second one, which we label the *Gaussian Covariance Matrix* (GCM), is the same as described in §5.2.1.

Finally, the *KiDS Covariance Matrix* (KCM) is used here for testing our invertible transformation as well as for some of the tests with $C3$. It is the same covariance matrix employed in the KiDS-1000 survey analysis with cosmic shear [144, 145], and it has two additional terms, as compared to GCM. One of them is responsible for the non-Gaussianity of the field, which generates higher-order correlations

between different modes. The other term is related to the super-sample covariance, which accounts for the correlations between modes in the survey and those that are larger than the survey scale.

### 6.2.3.4 Perturbing C3

To assess the relevance of $C3$ for the parameter constraints, we perturb it in several ways. We start by replacing $C3 = \mathbb{1}$, which is a dramatic change to the elements of $C3$. Since the elements of $C3$, as found here, are of order $\lesssim 1^{-10}$ (similarly to the elements of the original and compressed covariance matrices), this increases its diagonal elements by a large amount, while completely removing any information the off-diagonal elements might potentially carry. Figure 6.1 shows the results for this modification to the transformed KCM. We see that the constraints are, in fact, consistent with the unmodified covariance matrix. This new configuration is thus irrelevant for the parameter constraints.

Next, we follow the procedure outlined in §5.4 for the elements of the covariance matrix, on the elements of the $C3$ block of DCM. We introduce errors of $5\%, 10\%$ and $50\%$. As expected, the size of the $2\sigma$ constraints of $\Omega_m$ and $S_8$ are essentially identical to those obtained with the unperturbed, transformed covariance matrix, see Figure 6.2 (top panel).

We have so far demonstrated that the original parameter constraints are recovered for the modified transformed covariance matrix. For completeness, we verify the consequences to a "retransformed" covariance matrix. We start by perturbing the elements of $C3$ in a similar fashion, as described above, choosing errors of $5\%, 10\%$ and $50\%$. Then, we apply $\mathbf{B}^{-1}$ to revert the transformation of basis, such that the cosmological analyses are then performed with the original data vector. The bottom panel of Figure 6.2 shows the contour plots for $\Omega_m$ and $S_8$, which also confirm that $C3$ has no influence on the parameter constraints.
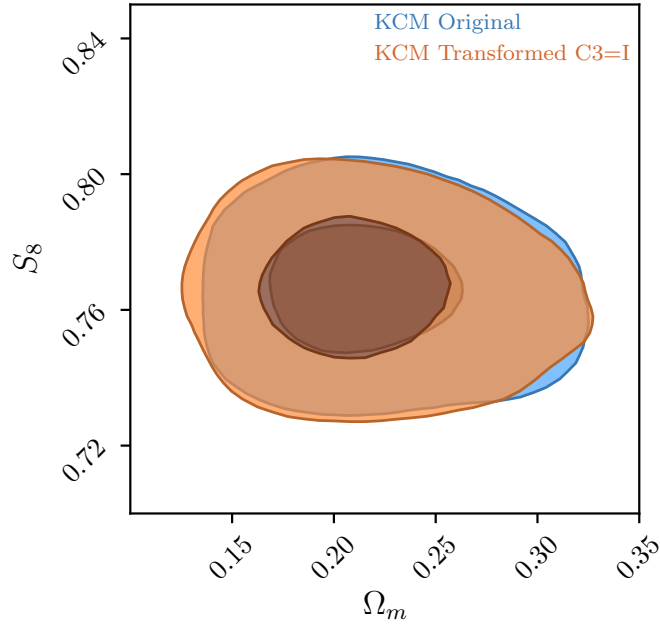
Figure 6.1: KiDS-1000 parameter constraints for the original and transformed covariance matrix for the cosmological parameters $\Omega_m$ and $S_8$. The darker curve, in blue, is for the original covariance matrix and the lighter curve, in orange, is for when the block $C3$ of KCM is replaced by the identity matrix.

Finally, in Figure 6.3 (left for DCM and right for KCM) we show the ratio between the elements of the perturbed covariance matrices and the original one for a 5% (top) and 50% perturbation (bottom), and highlight the diagonal elements in red. A clear trend can be seen: the smallest elements display a greater disagreement, and this decreases as their values increase. Since these large differences between the elements have no impact in the parameter constraints, we conclude that metrics to compare covariance matrices based solely on the elements themselves do not produce decisive results. As such, our best choice is to concentrate on $C1$, as originally proposed.
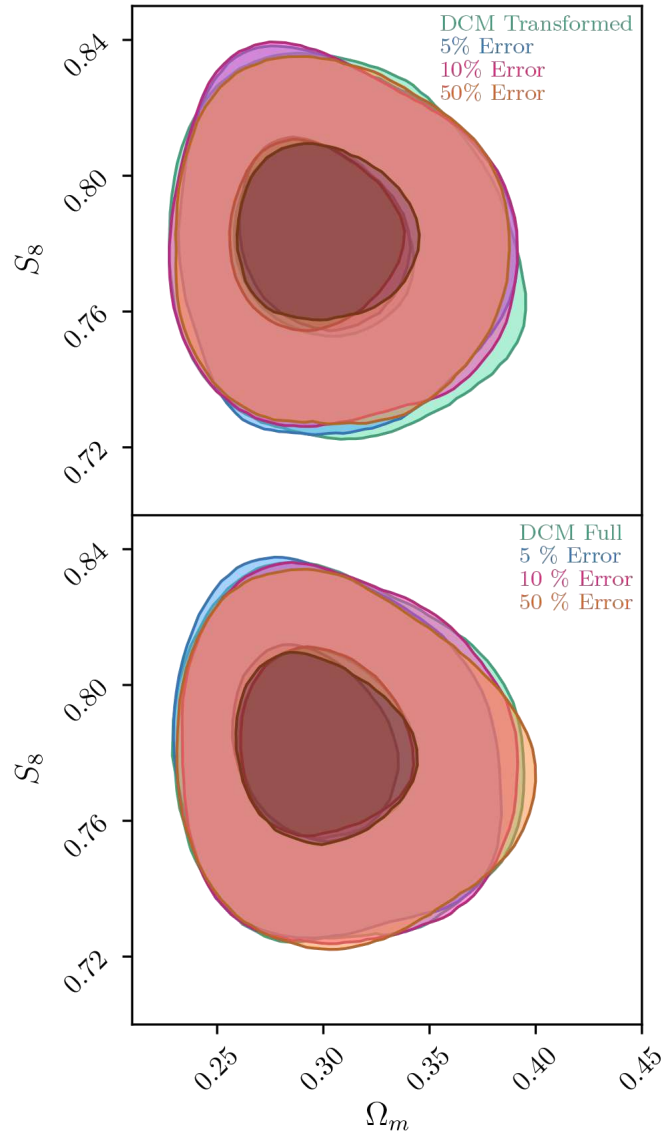
Figure 6.2: **Top:** DESY1 constraints on $\Omega_m$ and $S_8$ for the transformed covariance matrix (green) and for a 5% (blue), 10% (pink) and 50% (orange) perturbation applied to the $C3$ block of DCM. **Bottom:** DESY1 constraints for the original covariance matrix (green) and for three covariance matrices produced by applying the inverse transformation to those with 5% (blue), 10% (pink) and 50% (orange) perturbation applied to the $C3$ block of the transformed DCM.
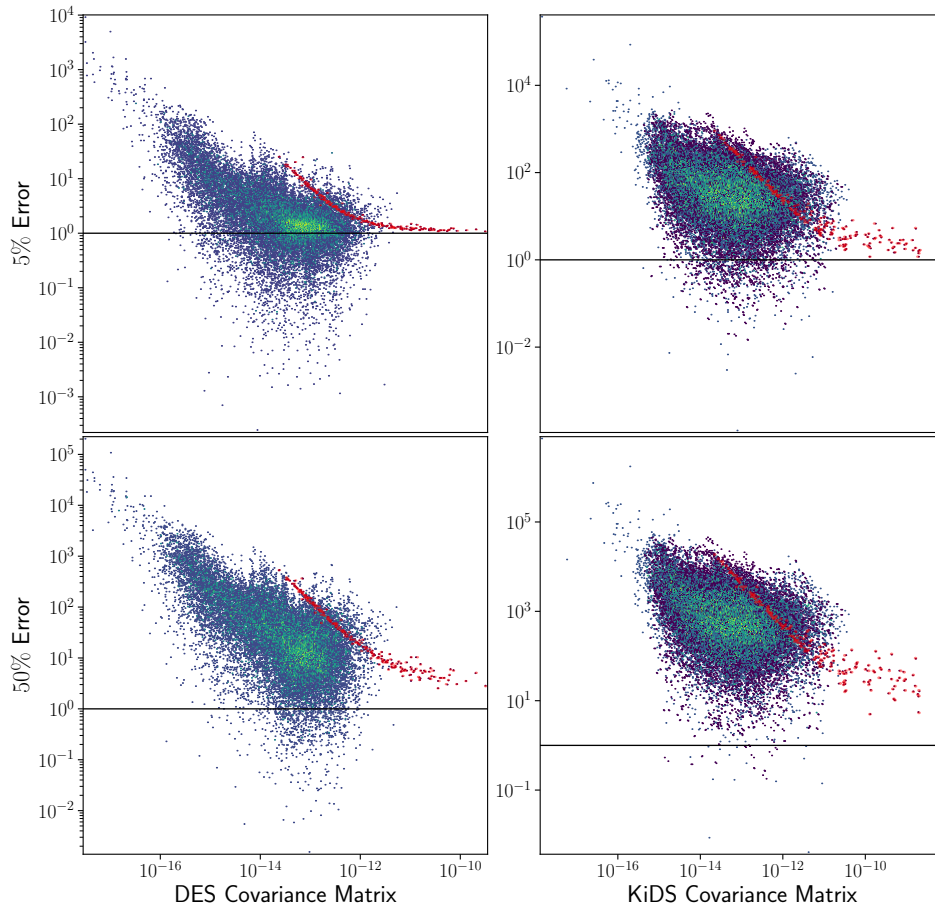
Figure 6.3: Scatter plots of the ratio of the elements of the perturbed covariance matrix and those of the original one against the latter. The top panels show the ratio for a 5% perturbation, the bottom ones for a 50% perturbation, the ones on the left are relative to DESY1, and the ones on the right to KiDS-1000. The red dots represent the ratio between the diagonal elements of the two matrices.

## 6.3 Comparing Covariance Matrices

Our results thus far have shown that all the relevant information for parameter constraints is contained in $C1$. This is fortunate for comparing matrices because we need to examine a significantly smaller number of elements (as opposed to large covariance matrices). In this section we explain the method we developed for obtaining a reliable metric of comparison that discards the need for a full cosmological analysis and is consequently able to deliver results in a considerably shorter amount of time.

Consider two covariance matrices that we want to compare: $C_{\text{base}}$, and $C_{\text{test}}$. We use MOPED to obtain their compressed covariance matrices, or the $C1$ blocks. The comparison is then divided into two parts: $n$–dimensional vector $\mathcal{D}$ containing the diagonal elements, which are related to the variance of the data and; the $n(n-1)/2$–dimensional vector $\mathcal{C}$ composed of the independent elements of the correlation matrix.

The python code developed to carry out this comparison can be accessed in github.com/t-ferreira/Covariance_comparison. Here, we detail its construction and functionality. The steps are as follows:

1. create a mock sample $\{\mathcal{D}_{\delta,i}\}$ by perturbing, with a given error percentage $\delta$, the vector $\mathcal{D}_{\text{base}}$ (or $\mathcal{C}_{\text{base}}$);

2. produce the sample covariance matrix $S_\delta$ from the generated mocks:

$$S_\delta = \frac{1}{m-1} \sum_{i=1}^{m} \left(\mathcal{D}_{\delta,i} - \overline{\mathcal{D}_\delta}\right) \left(\mathcal{D}_{\delta,i} - \overline{\mathcal{D}_\delta}\right)^t ,$$

where $m$ is the size of the mock sample;

3. obtain the fiducial $\chi^2$–distribution using:

$$\chi^2_{\delta,i} = (\mathcal{D}_{\delta,i} - \mathcal{D}_{\text{base}})\, S_\delta^{-1}\, (\mathcal{D}_{\delta,i} - \mathcal{D}_{\text{base}})^t \;\; ;$$

4. calculate $\chi^2_{\text{test}} = (\mathcal{D}_{\text{test}} - \mathcal{D}_{\text{base}})\; S_\delta^{-1}\, (\mathcal{D}_{\text{test}} - \mathcal{D}_{\text{base}})^t \;\; ;$

5. find $\delta^{\mathcal{D}}_{\text{test}}$ such that $\chi^2_{\text{test}}$ is the maximum of the $\chi^2$–distribution above;

6. find $\sigma_\delta = (\delta_+ - \delta_-)/2$, where $\delta_+$ is the value that makes $\chi^2_{\text{test}}$ fall at the right-hand border of the 68% probability interval of the $\chi^2$–distribution, and similarly for $\delta_-$.

The value of $\delta^{\mathcal{D}}_{\text{test}} \pm \sigma_\delta$ found by this method estimates the distance between the two $C1$ matrices, $C_{\text{base}}$ and $C_{\text{test}}$, as far as the uncertainties or correlations in the parameters are concerned.

The perturbed $\mathcal{D}_{\delta,i}$ is simply obtained by drawing $\mathcal{E}_{\mathcal{D}}$ from a multivariate Gaussian distribution $\mathcal{G}[0_n, \delta^2 I_n]$, such that,

$$\mathcal{D}_{\delta,i} = (1 + \mathcal{E}_{\mathcal{D}})\mathcal{D}_{\text{base}} \; . \tag{6.15}$$

For the correlation matrix, on the other hand, we adopt a more complicated approach to ensure that the perturbed values follow a smooth distribution. Simply taking the same method used for the diagonal elements and imposing a hard cut in the range $[-1, 1]$, could result in biased results not cohesive with our chosen $\delta$. Instead, we work with the hyperbolic tangent function and correct it for the Jacobian,

$$z_i = \tanh^{-1}(\mathcal{C}_{\text{base}}) \; ,$$

$$\delta z_i = \mathcal{E}_{\mathcal{C}}\left[\cosh\left(z_i + \frac{1}{2}\mathcal{E}_{\mathcal{C}}\right)\right]^2 \; , \tag{6.16}$$

where $\mathcal{E}_{\mathcal{C}}$ is drawn similarly to $\mathcal{E}_{\mathcal{D}}$. Our perturbed vector then becomes,

$$\mathcal{C}_{\delta,i} = \tanh\left(z_i + \delta z_i\right) \ . \tag{6.17}$$

Figure 6.4 illustrates how smoothly the error on $z_i$ translates to $\mathcal{C}_{\delta,i}$.
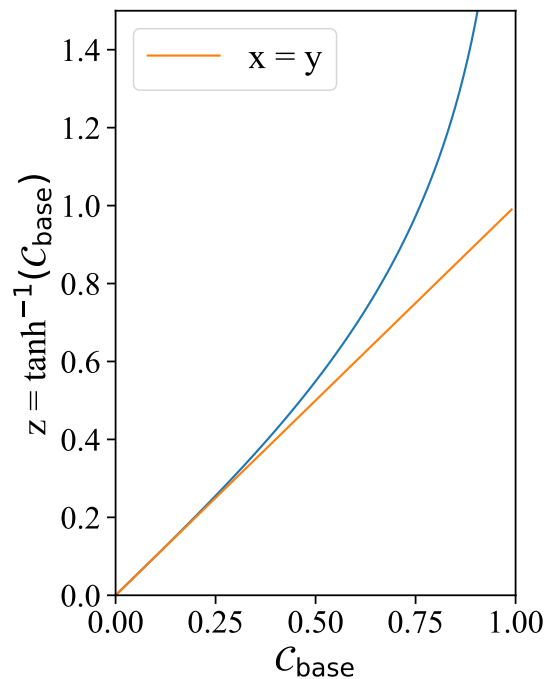


Figure 6.4: Illustration of how the error applied to $\delta z$ relates to the final value of $\mathcal{C}_\delta$. The blue curve is the function $\tanh^{-1}\left(\mathcal{C}_{\text{base}}\right)$

For steps (v-vi), we use `lmfit`'s minimize function and define the default to use Powell's method. For the mocks, we take the sample size $m$ to be 1000. This returns a value of $\delta_{\text{test}}$ in a few minutes, but, for robustness, we recommend setting this to $> 5000$.
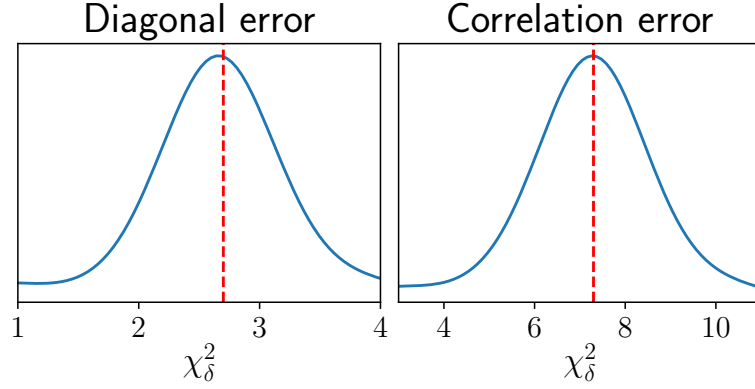
Figure 6.5: $\chi^2$–distributions that are used to determine $\delta_{\text{test}}$ for the diagonal elements of the covariance matrix (left) and for the elements of the correlation matrix (right). The method finds the $\delta_{\text{test}}$ value such that $\chi^2_{\text{test}}$ (red dashed line) falls at the maximum of the distribution.

### 6.3.1 Cosmic shear covariance matrices

The next steps are then to apply our methodology to the covariance matrices we wish to compare, $C_{\text{base}} = \text{DCM}$ and $C_{\text{test}} = \text{GCM}$. We have shown the parameter constraints for these two covariance matrices, given the same data vector, in Figure 5.1 for the cosmological parameters, and in Figure 5.2 for the systematic ones. Recall that, in this chapter, we refer to the FCM as DCM. In terms of constraints for individual parameters, the percentage differences for the cosmological parameters are up to 1.2%, with the interval shifts for the 68% contour levels of 2.4%, with larger differences for the nuisance parameters (of 6.2% and 24%, respectively).

Figure 6.5 shows the $\chi^2$–distributions used by our method: the values of $\delta_{\text{test}}$ are such that the $\chi^2_{\text{test}}$ values fall at the maximum of the distributions. We find that the diagonal elements of the $C1$ block of GCM differ by

$$\delta^{\mathcal{D}}_{\text{test}} = 2.6 \pm 0.2\% \; , \qquad (6.18)$$

while the correlations differ by

$$\delta^{\mathcal{C}}_{\text{test}} = 7.8 \pm 0.1\% \ .$$

(6.19)

While our results were not able to reproduce the exact differences in the parameter constraints, they set an upper bound on the error for the interval shifts. The larger disagreement between our values and the contour levels for the nuisance parameter remains to be examined.

Finally, our algorithm took roughly 0.5 CPUh (2020 laptop) to generate the desired output, while a full cosmological analysis takes roughly 100 times more.

## 6.4 Conclusion

The complexity and the considerable size of covariance matrices make them increasingly difficult to analyse. Because of the vast range of values, with its own elements often differing by several orders of magnitude, it is customary to identify the largest elements and the diagonal ones. Should these be similar, then it is likely that the parameter constraints are also compatible; we show here that this is a perilous assumption. Using an invertible transformation, we showed that it is possible to generate very distinct covariance matrices capable of generating the same cosmology, given the same data vector.

On the other hand, we also see that MOPED is capable of reducing the size of the covariance matrix while retaining the necessary information for parameter constraints. We use the compressed matrix formalism to develop a fast and reliable method for the comparison of covariance matrices that only considers the portion of the covariance matrix that is relevant for the parameter constraints.

Using our method, we show that the DCM and the GCM, which produce compatible cosmological constraints, feature a difference of 7.8% for the elements of

the correlation matrix and only 2.6% for the diagonal elements of the covariance matrix, in qualitative agreement with the full cosmological analysis.

While our approximate method cannot replace a full Bayesian analysis, it may be useful during the development and validation of codes that estimate covariance matrices. Lastly, we find a remarkable gain in terms of runtime, with our method taking roughly 100 times less CPUh than a full cosmological analysis.

# Conclusion

Mischief managed.

*Harry Potter and the Prisoner of Azkaban*

In this thesis, we presented two topics of agitated discussion in the cosmology community: alternatives to the standard model and how to tackle the dimensionality of covariance matrices in light of future Stage IV cosmological surveys. In this final chapter, I summarize the main takeaways from the works presented here.

In the realm of dark energy models, in Chapter 3, we introduced models with a phenomenological interaction in the dark sector, and compared their viability, against the standard cosmological model, by performing a Bayesian model selection. We show in Figure 3.1 a joint analysis with JLA + BAO + CC + CMB data, where we found disfavourable evidence for twelve, out of the fifteen, models with a linear interaction, and for two, of the six, models with a non-linear interaction. The remaining models were not discarded due to inconclusive evidence neither for nor against them, given the interpretation with Jeffreys scale. As the analyses were made with two sets of BAO measurements, as well as two different prior choices, we attribute interesting conclusions to each. In regard to the BAO measurements,

Figure 3.1 shows that the evidence against the interacting models is weaker for BAO2 than BAO3. This is expected since BAO2 is claimed to be more model independent [58]. On the other hand, when considering the prior scenarios 3.35 and 3.36, we see that the model-dependency of BAO3 appears to be partly related to the estimation of $r_d$ as the sound horizon at the drag epoch.

We then moved on to analysing the covariance matrices of cosmic shear statistics, with the intent of identifying the most relevant parts for parameter estimation. Towards that goal, we used data from the Dark Energy Survey Year 1 [131] to examine four compression schemes. The first method was to find the eigenvalues of the covariance matrix, which involved setting the 200 lowest eigenvalues to several orders of magnitude lower. The next analysis followed a similar procedure, where the eigenvalues were replaced with the signal-to-noise ratio of the modes of the covariance matrix. These two methods yielded similar results, showing good constraining power (as compared to the original constraints) for $\Omega_m$, and less so for $S_8$ and $A_{\mathrm{IA}}$. These results were analogous to those obtained with the third approach, which employed a tomographic compression. The compression with one and two KL-modes produced a reduction of 99% or 91%, respectively, for a $190 \times 190$ covariance matrix. The resulting constraints are consistent with the IA parameters being more sensitive to low SNR scales in cosmic shear, and we see that the high KL-modes fail to break the degeneracy of $A_{\mathrm{IA}} - S_8$ correlation, resulting in larger $S_8$ constraints. Finally, we showed that MOPED was not only the compression scheme with the highest reduction, going from a $227 \times 227$ matrix to a $16 \times 16$ matrix, but it was also capable of reproducing the parameter constraints obtained with the full covariance matrix.

The covariance comparison was done in terms of the elements of the full covariance matrix and in terms of the elements of their compressed ones. We showed that the one-to-one comparison between the compressed FCM and the GCM, in

Figure 5.11, are more consistent with the direct comparison of their parameter constraints. In this sense, one of our most important results of the chapter is the ability to use MOPED to compare different matrices. Finally, we tested the error tolerance of the compressed the FCM by introducing error taken from a Gaussian distribution for $5 - 45\%$ of the original elements and of the eigenvalues of the compressed covariance matrix. For both cases, the means and $2\sigma$ constraints for $A_{\mathrm{IA}}$ were more pronounced than for $\Omega_m$ and $S_8$.

Finally, we extended MOPED to a reversible transformation and generated mock $227 \times 227$ covariance matrices with the same compressed one ($C1$), and showed that, although their elements greatly diverged, the parameter constraints were largely similar. This motivated the construction of a python algorithm to compare compressed covariance matrices in terms of their diagonal elements and the independent elements of their correlation matrix. We then demonstrated its performance by comparing the FCM and the GCM, yielding results about 100 times faster, that were in close agreement with a comparison of their parameter constraints.

# Bibliography

[1] B. Moore, T. R. Quinn, F. Governato, J. Stadel, and G. Lake. *Cold collapse and the core catastrophe.* Monthly Notices of the Royal Astronomical Society **310** (1999). `arXiv:9903164`. Cited on page 1.

[2] M. Boylan-Kolchin, J. S. Bullock, and M. Kaplinghat. *Too big to fail? The puzzling darkness of massive Milky Way subhaloes.* Monthly Notices of the Royal Astronomical Society: Letters **415** (2011). `arXiv:1103.0007`. Cited on page 1.

[3] A. G. Riess, S. Casertano, W. Yuan, L. M. Macri, and D. Scolnic. *Large Magellanic Cloud Cepheid Standards Provide a 1% Foundation for the Determination of the Hubble Constant and Stronger Evidence for Physics Beyond ΛCDM.* The Astrophysical Journal **876** (2019). `arXiv:1903.07603`. Cited on page 1.

[4] M. Asgari et al. *KiDS-1000 Cosmology: Cosmic shear constraints and comparison between two point statistics.* Astronomy & Astrophysics **645** A104 (2021). `arXiv:2007.15633`. Cited on pages 1, 110, and 111.

[5] K. Heitmann, D. Higdon, M. White, S. Habib, B. J. Williams, and C. Wagner. *The Coyote Universe II: Cosmological Models and Precision Emulation of the Nonlinear Matter Power Spectrum.* The Astrophysical Journal **705** (2009). `arXiv:0902.0429`. Cited on page 2.

[6] H. Bondi. *Cosmology.* Cambridge University Press Cambridge, England 1952. Cited on page 4.

[7] R. Maartens. *Is the universe homogeneous?* Philosophical Transactions of the Royal Society A **369** 5115 (2011). arXiv:1104.1300. Cited on page 5.

[8] H. Mo, F. van den Bosch, and S. White. *Galaxy formation and evolution.* Cambridge University Press Cambridge, England 2010. Cited on page 6.

[9] S. M. Carroll. *Spacetime and geometry: An introduction to general relativity.* Cambridge University Press Cambridge, England 2019. Cited on pages 6 and 7.

[10] E. Hubble. *A relation between distance and radial velocity among extragalactic nebulae.* Proceedings of the National Academy of Sciences of the United States of America **15** 168 (1929). Cited on pages 9, 13, and 18.

[11] A. W. McConnachie. *The observed properties of dwarf galaxies in and around the local group.* The Astronomical Journal **144** (2012). arXiv:1204.1562. Cited on page 10.

[12] L. Amendola and S. Tsujikawa. *Dark energy: Theory and observations.* Cambridge University Press Cambridge, England 2010. Cited on pages 11 and 59.

[13] A. G. Riess, S. Casertano, W. Yuan, J. B. Bowers, L. Macri, J. C. Zinn, and D. Scolnic. *Cosmic distances calibrated to 1% precision with gaia EDR3 parallaxes and hubble space telescope photometry of 75 milky way cepheids confirm tension with ΛCDM.* The Astrophysical Journal **908** L6 (2021). arXiv:2012.08534. Cited on pages 13 and 30.

[14] W. L. Freedman, B. F. Madore, T. Hoyt, I. S. Jang, R. Beaton, M. G. Lee, A. Monson, J. Neeley, and J. Rich. *Calibration of the tip of the red giant branch.* The Astrophysical Journal **891** 57 (2020). `arXiv:2002.01550`. Cited on page 13.

[15] Planck Collaboration. *Planck 2018 results. VI. Cosmological parameters.* Astronomy & Astrophysics **641** A6 (2020). `arXiv:1807.06209`. Cited on pages 13 and 30.

[16] N. A. Bahcall. *Hubble's Law and the expanding universe.* Proceedings of the National Academy of Sciences **112** 3173 (2015). Cited on page 13.

[17] R. C. Tolman. *On the astronomical implications of the de sitter line element for the universe.* The Astrophysical Journal **69** 245 (1929). Cited on page 15.

[18] I. M. H. Etherington. *LX. On the definition of distance in general relativity.* The London, Edinburgh, and Dublin Philosophical Magazine and Journal of Science **15** 761 (1933). Cited on page 15.

[19] L. D. Landau and L. M. Lifshitz. *Quantum mechanics non-relativistic theory.* Butterworth-Heinemann Oxford, England 1981. Cited on page 17.

[20] A. G. Riess et al. *Observational evidence from supernovae for an accelerating universe and a cosmological constant.* The Astronomical Journal **116** 1009 (1998). `arXiv:9805201`. Cited on page 18.

[21] A. V. Filippenko and A. G. Riess. *Results from the high-z supernova search team.* Physics Reports **307** 31 (1998). `arXiv:9807008`. Cited on page 18.

[22] R. J. Adler, B. Casey, and O. C. Jacob. *Vacuum catastrophe: An elementary exposition of the cosmological constant problem.* American Journal of Physics **62** 620 (1995). Cited on page 19.

[23] S. Tsujikawa. *Quintessence: A review.* Classical and Quantum Gravity **30** 214003 (2013). `arXiv:1304.1961`. Cited on pages 20 and 23.

[24] H. Wei. *Cosmological evolution of quintessence and phantom with a new type of interaction in dark sector.* Nuclear Physics B **845** 381 (2011). `arXiv:1008.4968`. Cited on pages 20 and 23.

[25] L. Amendola. *Coupled quintessence.* Physical Review D **62** 043511 (2000). `arXiv:9908023`. Cited on pages 20, 23, and 25.

[26] G. W. Horndeski. *Second-order scalar-tensor field equations in a four-dimensional space.* International Journal of Theoretical Physics **10** 363 (1974). Cited on page 20.

[27] L. Amendola, M. Kunz, I. D. Saltas, and I. Sawicki. *The fate of large-scale structure in modified gravity after GW170817 and GRB170817A.* Physical Review Letters **120** 131101 (2018). `arXiv:1711.04825`. Cited on page 20.

[28] F. Zwicky. *Die Rotverschiebung von extragalaktischen Nebeln.* Helvetica Physica Acta **6** 110 (1933). Cited on page 20.

[29] V. C. Rubin and J. Ford,W. Kent. *Rotation of the andromeda nebula from a spectroscopic survey of emission regions.* The Astrophysical Journal **159** 379 (1970). Cited on page 20.

[30] R. Massey, T. Kitching, and J. Richard. *The dark matter of gravitational lensing.* Reports on Progress in Physics **73** (2010). `arXiv:1001.1739`. Cited on page 20.

[31] D. Harvey, A. Robertson, R. Massey, and J.-P. Kneib. *Looking for dark matter trails in colliding galaxy clusters.* Monthly Notices of the Royal Astronomical Society **464** 3991– (2016). `arXiv:1610.05327`. Cited on page 20.

[32] C. S. Frenk and S. D. M. White. *Dark matter and cosmic structure.* Annalen der Physik **524** 507 (2012). `arXiv:1210.0544`. Cited on page 20.

[33] A. Cid, B. Santos, C. Pigozzo, T. Ferreira, and J. Alcaniz. *Bayesian comparison of interacting scenarios.* Journal of Cosmology and Astroparticle Physics **2019** 030 (2019). `arXiv:1805.02107`. Cited on page 22.

[34] U. Debnath. *Variable modified chaplygin gas and accelerating universe.* Astrophysics and Space Science **312** 295 (2007). `arXiv:0710.1708`. Cited on page 22.

[35] T. Ferreira, C. Pigozzo, S. Carneiro, and J. Alcaniz. *Interaction in the dark sector: A bayesian analysis with latest observations.* (2017). `arXiv:1712.05428`. Cited on page 22.

[36] N. Dalal, K. Abazajian, E. E. Jenkins, and A. V. Manohar. *Testing the cosmic coincidence problem and the nature of dark energy.* Physical Review Letters **87** 141302 (2001). `arXiv:0105317`. Cited on pages 23 and 25.

[37] F. Arevalo, A. P. R. Bacalhau, and W. Zimdahl. *Cosmological dynamics with non-linear interactions.* Classical and Quantum Gravity **29** 235001 (2012). `arXiv:1112.5095`. Cited on pages 23 and 26.

[38] L. P. Chimento. *Linear and nonlinear interactions in the dark sector.* Physical Review D **81** 043525 (2010). `arXiv:0911.5687`. Cited on pages 23, 24, and 25.

[39] W. Zimdahl, D. Pavon, and L. Chimento. *Interacting quintessence.* Physics Letters B **521** 133 (2001). `arXiv:0105479`. Cited on pages 23 and 25.

[40] H. M. Sadjadi and M. Alimohammadi. *Cosmological coincidence problem*

*in interactive dark energy models.* Physical Review D **74** 103007 (2006). `arXiv:0610080`. Cited on page 23.

[41] B. Bassett and R. Hlozek. *Baryon acoustic oscillations* chapter 9. Cambridge University Press Cambridge, England 2010. Cited on pages 27 and 28.

[42] X. Li, S. Cao, X. Zheng, S. Li, and M. Biesiada. *Comparison of cosmological models using standard rulers and candles.* Research in Astronomy and Astrophysics **16** 015 (2016). `arXiv:1510.03494`. Cited on page 27.

[43] D. J. Eisenstein and W. Hu. *Baryonic features in the matter transfer function.* The Astrophysical Journal **496** 605 (1998). `arXiv:9709112`. Cited on page 27.

[44] D. J. Eisenstein. *Large-scale structure & future surveys.* In *Next generation wide-field multi-object Spectroscopy* volume 280 of *Astronomical Society of the Pacific Conference Series* 2002. Cited on page 27.

[45] D. J. Eisenstein et al. *Detection of the baryon acoustic peak in the large-scale correlation function of SDSS luminous red galaxies.* The Astrophysical Journal **633** 560 (2005). `arXiv:0501171`. Cited on page 27.

[46] S. Alam et al. *The clustering of galaxies in the completed SDSS-III baryon oscillation spectroscopic survey: Cosmological analysis of the dr12 galaxy sample.* Monthly Notices of the Royal Astronomical Society **470** 2617 (2017). `arXiv:1607.03155`. Cited on pages 28 and 29.

[47] H. du Mas des Bourboux et al. *Baryon acoustic oscillations from the complete SDSS-III Ly$\alpha$-quasar cross-correlation function at $z = 2.4$.* Astronomy & Astrophysics **608** A130 (2017). `arXiv:1708.02225`. Cited on pages 28 and 29.

[48] A. J. Ross, L. Samushia, C. Howlett, W. J. Percival, A. Burden, and M. Man- era. *The clustering of the SDSS DR7 main galaxy sample – I. A 4 per cent distance measure at $z = 0.15$*. Monthly Notices of the Royal Astronomical Society **449** 835 (2015). `arXiv:1409.3242`. Cited on pages 28 and 29.

[49] F. Beutler, C. Blake, M. Colless, D. H. Jones, L. Staveley-Smith, L. Camp- bell, Q. Parker, W. Saunders, and F. Watson. *The 6dF galaxy survey: Baryon acoustic oscillations and the local hubble constant*. Monthly No- tices of the Royal Astronomical Society **416** 3017 (2011). `arXiv:1106.3366`. Cited on pages 28 and 29.

[50] A. J. Cuesta et al. *The clustering of galaxies in the SDSS-III Baryon Oscil- lation Spectroscopic Survey: Baryon Acoustic Oscillations in the correlation function of LOWZ and CMASS galaxies in Data Release 12*. Monthly Notices of the Royal Astronomical Society **457** 1770 (2016). `arXiv:1509.06371`. Cited on pages 28 and 29.

[51] P. A. R. Ade et al. *Planck 2015 results. XIII. Cosmological parameters*. Astronomy & Astrophysics **594** A13 (2016). `arXiv:1502.01589`. Cited on pages 28, 31, 33, 41, and 42.

[52] J. Hou et al. *The clustering of the SDSS-IV extended Baryon Oscillation Spectroscopic Survey DR14 quasar sample: Anisotropic clustering analysis in configuration-space*. Monthly Notices of the Royal Astronomical Society **480** 2521 (2018). `arXiv:1801.02656`. Cited on page 29.

[53] M. Ata et al. *The clustering of the SDSS-IV extended baryon oscillation spec- troscopic survey DR14 quasar sample: first measurement of baryon acoustic oscillations between redshift 0.8 and 2.2*. Monthly Notices of the Royal As- tronomical Society **473** 4773 (2018). `arXiv:1705.06373`. Cited on page 29.

[54] N. Aghanim et al. *Planck 2018 results. vi. Cosmological parameters.* Astronomy & Astrophysics **641** A6 (2020). `arXiv:1807.06209`. Cited on page 29.

[55] W. J. Percival et al. *Baryon acoustic oscillations in the sloan digital sky survey data release 7 galaxy sample.* Monthly Notices of the Royal Astronomical Society **401** 2148 (2010). `arXiv:0907.1660`. Cited on page 29.

[56] A. Lewis and A. Challinor. *CAMB: Code for Anisotropies in the Microwave Background* 2011. `arXiv:1102.026`. Cited on pages 30 and 32.

[57] A. G. Sánchez et al. *The clustering of galaxies in the SDSS-III Baryon Oscillation Spectroscopic Survey: cosmological implications of the large-scale two-point correlation function.* Monthly Notices of the Royal Astronomical Society **425** 415 (2012). `arXiv:1203.6616`. Cited on page 30.

[58] G. C. Carvalho, A. Bernui, M. Benetti, J. C. Carvalho, and J. S. Alcaniz. *Baryon acoustic oscillations from the SDSS DR10 galaxies angular correlation function.* Physical Review D **93** 023530 (2016). `arXiv:1507.08972`. Cited on pages 30, 31, and 124.

[59] J. S. Alcaniz, G. C. Carvalho, A. Bernui, J. C. Carvalho, and M. Benetti. *Measuring baryon acoustic oscillations with angular two-point correlation function.* Gravity and the Quantum **187** 11 (2017). `arXiv:1611.08458`. Cited on page 31.

[60] G. C. Carvalho, A. Bernui, M. Benetti, J. C. Carvalho, and J. S. Alcaniz. *Measuring the transverse baryonic acoustic scale from the SDSS DR11 galaxies.* 2017). `arXiv:1709.00271`. Cited on page 31.

[61] E. de Carvalho, A. Bernui, G. C. Carvalho, and C. P. Novaes. *Angular baryon acoustic oscillation measure at z=2.225 from the SDSS quasar survey.*

Journal of Cosmology and Astroparticle Physics **1804** 064 (2018). `arXiv:1709.00113`. Cited on page 31.

[62] L. Verde, J. L. Bernal, A. F. Heavens, and R. Jimenez. *The length of the low-redshift standard ruler.* Monthly Notices of the Royal Astronomical Society **467** 731 (2017). `arXiv:1607.05297`. Cited on pages 30, 31, 41, and 42.

[63] J. L. Bernal, L. Verde, and A. G. Riess. *The trouble with $H_0$.* Journal of Cosmology and Astroparticle Physics **1610** 019 (2016). `arXiv:1607.05617`. Cited on page 30.

[64] A. Heavens, R. Jimenez, and L. Verde. *Standard rulers, candles, and clocks from the low-redshift Universe.* Physical Review Letters **113** 241302 (2014). `arXiv:1409.6217`. Cited on page 30.

[65] A. A. Penzias and R. W. Wilson. *A Measurement of Excess Antenna Temperature at 4080 Mc/s.* The Astrophysical Journal **142** 419 (1965). Cited on page 31.

[66] G. F. Smoot et al. *Structure in the COBE Differential Microwave Radiometer First-Year Maps.* The Astrophysical Journal: Letters **396** L1 (1992). Cited on page 31.

[67] W. Hu and M. White. *Acoustic Signatures in the Cosmic Microwave Background.* The Astrophysical Journal **471** 30 (1996). `arXiv:astro-ph/9602019`. Cited on page 32.

[68] M. Baldi and V. Pettorino. *High-z massive clusters as a test for dynamical coupled dark energy.* Monthly Notices of the Royal Astronomical Society **412** L1 (2011). `arXiv:1006.3761`. Cited on page 32.

[69] P. A. R. Ade et al. *Planck 2015 results. XIV. Dark energy and modified gravity.* Astronomy & Astrophysics **594** A14 (2016). `arXiv:1502.01590`. Cited on pages 32, 33, and 42.

[70] G. Efstathiou and J. R. Bond. *Cosmic confusion: degeneracies among cosmological parameters derived from measurements of microwave background anisotropies.* Monthly Notices of the Royal Astronomical Society **304** 75 (1999). Cited on page 32.

[71] R. J. Cooke, M. Pettini, K. M. Nollett, and R. Jorgenson. *The primordial deuterium abundance of the most metal-poor damped Lyα system.* The Astrophysical Journal **830** 148 (2016). `arXiv:1607.03900`. Cited on pages 32 and 42.

[72] W. Hu and N. Sugiyama. *Small scale cosmological perturbations: An Analytic approach.* The Astrophysical Journal **471** 542 (1996). `arXiv:astro-ph/9510117`. Cited on page 33.

[73] R. Jimenez and A. Loeb. *Constraining cosmological parameters based on relative galaxy ages.* The Astrophysical Journal **573** 37 (2002). `arXiv:0106145`. Cited on page 33.

[74] J. Dunlop, J. Peacock, H. Spinrad, A. Dey, R. Jimenez, D. Stern, and R. Windhorst. *A 3.5-Gyr-old galaxy at redshift 1.55.* Nature **381** 581 (1996). Cited on page 33.

[75] L. Verde, P. Protopapas, and R. Jimenez. *The expansion rate of the intermediate universe in light of Planck.* Physics of the Dark Universe **5–6** 307 (2014). `arXiv:1403.2181`. Cited on page 34.

[76] G. Bruzual and S. Charlot. *Stellar population synthesis at the resolution of*

*2003.* Monthly Notices of the Royal Astronomical Society **344** 1000– (2003). `arXiv:0309134`. Cited on page 34.

[77] M. Moresco et al. *Improved constraints on the expansion rate of the universe up to $z \sim 1.1$ from the spectroscopic evolution of cosmic chronometers.* Journal of Cosmology and Astroparticle Physics **2012** 006 (2012). `arXiv:1201.3609`. Cited on pages 34 and 35.

[78] C. Zhang, H. Zhang, S. Yuan, T.-J. Zhang, and Y.-C. Sun. *Four new observational $H(z)$ data from luminous red galaxies in the sloan digital sky survey data release seven.* Research in Astronomy and Astrophysics **14** 1221 (2014). `arXiv:1207.4541`. Cited on page 35.

[79] J. Simon, L. Verde, and R. Jimenez. *Constraints on the redshift dependence of the dark energy potential.* Physical Review D **71** 123001 (2005). `arXiv:0412269`. Cited on page 35.

[80] M. Moresco et al. *A 6% measurement of the Hubble parameter at $z \sim 0.45$: direct evidence of the epoch of cosmic re-acceleration.* Journal of Cosmology and Astroparticle Physics **1605** 014 (2016). `arXiv:1601.01701`. Cited on page 35.

[81] D. Stern, R. Jimenez, L. Verde, M. Kamionkowski, and S. A. Stanford. *Cosmic chronometers: Constraining the equation of state of dark energy. I: $H(z)$ measurements.* Journal of Cosmology and Astroparticle Physics **1002** 008 (2010). `arXiv:0907.3149`. Cited on page 35.

[82] N. N. Weinberg and L. Bildsten. *Carbon Detonation and Shock-Triggered Helium Burning in Neutron Star Superbursts.* The Astrophysical Journal **670** 1291 (2007). `arXiv:0706.3062`. Cited on page 36.

[83] B. Ryden. *Introduction to Cosmology.* Pearson Ohio, USA 2003. Cited on page 36.

[84] M. Betoule et al. *Improved cosmological constraints from a joint analysis of the sdss-ii and snls supernova samples.* Astronomy & Astrophysics **568** A22 (2014). `arXiv:1401.4064`. Cited on page 37.

[85] J. Guy et al. *The Supernova Legacy Survey 3-year sample: Type Ia supernovae photometric distances and cosmological constraints.* Astronomy & Astrophysics **523** A7 (2010). `arXiv:1010.4743`. Cited on page 37.

[86] R. Tripp. *A two-parameter luminosity correction for Type IA supernovae.* Astronomy & Astrophysics **331** 815 (1998). Cited on page 37.

[87] D. M. Scolnic et al. *The Complete Light-curve Sample of Spectroscopically Confirmed SNe Ia from Pan-STARRS1 and Cosmological Constraints from the Combined Pantheon Sample.* The Astrophysical Journal **859** 101 (2018). `arXiv:1710.00845`. Cited on page 38.

[88] A. G. Riess et al. *BVRI light curves for 22 type ia supernovae.* The Astronomical Journal **117** 707 (1999). `arXiv:astro-ph/9810291`. Cited on page 38.

[89] S. Jha et al. *UBVRI light curves of 44 type ia supernovae.* The Astronomical Journal **131** 527 (2006). `arXiv:astro-ph/0509234`. Cited on page 38.

[90] M. Hicken, W. M. Wood-Vasey, S. Blondin, P. Challis, S. Jha, P. L. Kelly, A. Rest, and R. P. Kirshner. *Improved Dark Energy Constraints from ~100 New CfA Supernova Type Ia Light Curves.* The Astrophysical Journal **700** 1097 (2009). `arXiv:0901.4804`. Cited on page 38.

[91] M. Hicken et al. *CfA3: 185 type ia supernova light curves from the CfA*. The Astrophysical Journal **700** 331 (2009). `arXiv:0901.4787`. Cited on page 38.

[92] M. Hicken et al. *CfA4: Light curves for 94 type ia supernovae*. The Astrophysical Journal Supplement Series **200** 12 (2012). Cited on page 38.

[93] C. Contreras et al. *The Carnegie Supernova Project: First Photometry Data Release of Low-Redshift Type Ia Supernovae*. The Astronomical Journal **139** 519 (2010). `arXiv:0910.3330`. Cited on page 38.

[94] G. Folatelli et al. *The Carnegie Supernova Project: Analysis of the First Sample of Low-Redshift Type-Ia Supernovae*. The Astronomical Journal **139** 120 (2010). `arXiv:0910.3317`. Cited on page 38.

[95] M. D. Stritzinger et al. *The Carnegie Supernova Project: Second Photometry Data Release of Low-redshift Type Ia Supernovae*. The Astronomical Journal **142** 156 (2011). `arXiv:1108.3108`. Cited on page 38.

[96] A. Conley et al. *Supernova Constraints and Systematic Uncertainties from the First Three Years of the Supernova Legacy Survey*. The Astrophysical Journal Supplement **192** 1 (2011). `arXiv:1104.1443`. Cited on page 38.

[97] M. Sullivan et al. *SNLS3: Constraints on Dark Energy Combining the Supernova Legacy Survey Three-Year Data with Other Probes*. The Astrophysical Journal **737** 102 (2011). `arXiv:1104.1444`. Cited on page 38.

[98] J. A. Frieman et al. *The Sloan Digital Sky Survey-II Supernova Survey: Technical Summary*. The Astronomical Journal **135** 338 (2008). `arXiv:0708.2749`. Cited on page 38.

[99] R. Kessler et al. *First-Year Sloan Digital Sky Survey-II Supernova Results:*

*Hubble Diagram and Cosmological Parameters.* The Astrophysical Journal Supplement **185** 32 (2009). `arXiv:0908.4274`. Cited on page 38.

[100] N. Suzuki et al. *The Hubble Space Telescope Cluster Supernova Survey. V. Improving the Dark-energy Constraints above z ¿ 1 and Building an Early-type-hosted Supernova Sample.* The Astrophysical Journal **746** 85 (2012). `arXiv:1105.3470`. Cited on page 38.

[101] A. G. Riess et al. *New Hubble Space Telescope Discoveries of Type Ia Supernovae at z >= 1: Narrowing Constraints on the Early Behavior of Dark Energy.* The Astrophysical Journal **659** 98 (2007). `arXiv:astro-ph/0611572`. Cited on page 38.

[102] S. A. Rodney et al. *Type Ia Supernova Rate Measurements to Redshift 2.5 from CANDELS: Searching for Prompt Explosions in the Early Universe.* The Astronomical Journal **148** 13 (2014). `arXiv:1401.7978`. Cited on page 38.

[103] O. Graur et al. *Type-Ia Supernova Rates to Redshift 2.4 from CLASH: The Cluster Lensing And Supernova Survey with Hubble.* The Astronomical Journal **783** 28 (2014). `arXiv:1310.3495`. Cited on page 38.

[104] A. G. Riess et al. *Type Ia Supernova Distances at Redshift ¿1.5 from the Hubble Space Telescope Multi-cycle Treasury Programs: The Early Expansion Rate.* The Astrophysical Journal **853** 126 (2018). `arXiv:1710.00844`. Cited on page 38.

[105] M. Kunz, B. A. Bassett, and R. A. Hlozek. *Bayesian estimation applied to multiple species.* Physical Review D **75** 103508 (2007). `arXiv:astro-ph/0611004`. Cited on page 38.

[106] R. Kessler and D. Scolnic. *Correcting Type Ia Supernova Distances for Selection Biases and Contamination in Photometrically Identified Samples.* The Astrophysical Journal **836** 56 (2017). `arXiv:1610.04677`. Cited on page 38.

[107] R. Allison and J. Dunkley. *Comparison of sampling techniques for Bayesian parameter estimation.* Monthly Notices of the Royal Astronomical Society **437** 3918 (2014). `arXiv:1308.2675`. Cited on page 40.

[108] T. Bayes. *An Essay Towards Solving A Problem In The Doctrine Of Chances.* Philosophical Transactions **53** 370 (1763). Cited on page 40.

[109] H. Jeffreys. *Theory of Probability.* Oxford University Press Oxford, England 1961. Cited on page 40.

[110] R. Trotta. *Bayes in the sky: Bayesian inference and model selection in cosmology.* Contemporary Physics **49** 71 (2008). `arXiv:0803.4089`. Cited on pages 40 and 41.

[111] F. Feroz and M. P. Hobson. *Multimodal nested sampling: An efficient and robust alternative to Markov Chain Monte Carlo methods for astronomical data analyses.* Monthly Notices of the Royal Astronomical Society **384** 449 (2008). `arXiv:0704.3704`. Cited on page 41.

[112] F. Feroz, M. P. Hobson, and M. Bridges. *MultiNest: An efficient and robust Bayesian inference tool for cosmology and particle physics.* Monthly Notices of the Royal Astronomical Society **398** 1601 (2009). `arXiv:0809.3437`. Cited on pages 41 and 75.

[113] F. Feroz, M. P. Hobson, E. Cameron, and A. N. Pettitt. *Importance nested sampling and the MultiNest algorithm.* 2013). `arXiv:1306.2144`. Cited on page 41.

[114] A. G. Riess et al. *A 2.4% Determination of the Local Value of the Hubble Constant.* The Astrophysical Journal **826** 56 (2016). `arXiv:1604.01424`. Cited on pages 41 and 42.

[115] F. Arevalo, A. Cid, and J. Moya. *AIC and BIC for cosmological interacting scenarios.* European Physical Journal **C77** 565 (2017). `arXiv:1610.09330`. Cited on pages 42 and 46.

[116] D. Pavon and B. Wang. *Le Chatelier-Braun principle in cosmological physics.* General Relativity and Gravitation **41** 1 (2009). `arXiv:0712.0565`. Cited on page 42.

[117] E. Komatsu et al. *Seven-Year Wilkinson Microwave Anisotropy Probe (WMAP) Observations: Cosmological Interpretation.* The Astrophysical Journal Supplemental **192** 18 (2011). `arXiv:1001.4538`. Cited on page 42.

[118] G. Mangano, G. Miele, S. Pastor, T. Pinto, O. Pisanti, and P. D. Serpico. *Relic neutrino decoupling including flavor oscillations.* Nuclear Physics **B729** 221 (2005). `arXiv:hep-ph/0506164`. Cited on page 42.

[119] R. von Marttens, L. Casarini, D. F. Mota, and W. Zimdahl. *Cosmological constraints on parametrized interacting dark energy.* Physics of the Dark Universe **23** 100248 (2019). `arXiv:1807.11380`. Cited on page 45.

[120] M. Benetti, L. L. Graef, and J. S. Alcaniz. *The $H_0$ and $\sigma_8$ tensions and the scale invariant spectrum.* Journal of Cosmology and Astroparticle Physics **1807** 066 (2018). `arXiv:1712.00677`. Cited on page 45.

[121] B. Santos, N. C. Devi, and J. S. Alcaniz. *Bayesian comparison of nonstandard cosmologies using type Ia supernovae and BAO data.* Physical Review D **95** 123514 (2017). `arXiv:1603.06563`. Cited on page 46.

[122] D. Walsh, R. F. Carswell, and R. J. Weymann. *0957+561 A, B: twin quasistellar objects or gravitational lens?* Nature **279** 381 (1979). Cited on page 57.

[123] G. Soucail, Y. Mellier, B. Fort, G. Mathez, and M. Cailloux. *Discovery of the first gravitational Einstein ring - The luminous arc in Abell 370.* The Messenger **50** 5 (1987). Cited on page 57.

[124] P. Schneider, L. van Waerbeke, and Y. Mellier. *B-modes in cosmic shear from source redshift clustering.* Astronomy & Astrophysics **389** 729 (2002). arXiv:0112441. Cited on page 57.

[125] T. D. Kitching, J. Alsing, A. F. Heavens, R. Jimenez, J. D. McEwen, and L. Verde. *The limits of cosmic shear.* Monthly Notices of the Royal Astronomical Society **469** 2737 (2017). arXiv:1611.04954. Cited on page 58.

[126] M. Meneghetti. *Introduction to Gravitational Lensing* 2017. URL: http://pico.oabo.inaf.it/~massimo/teaching/notes/. Cited on page 58.

[127] O. Piattella. *Lecture notes in cosmology.* Springer 2018. Cited on page 58.

[128] G. B. Arfken. *Mathematical Methods for Physicists.* Elsevier Ohio, USA 2012. Cited on page 71.

[129] T. Ferreira, T. Zhang, N. Chen, and S. Dodelson. *Data compression and covariance matrix inspection: Cosmic shear.* Physical Review D **103** 103535 (2021). arXiv:2010.15986. Cited on page 73.

[130] T. M. C. Abbott et al. *Dark energy survey year 1 results: Cosmological constraints from galaxy clustering and weak lensing.* Physical Review D **98** 043526 (2018). arXiv:1708.01530. Cited on page 74.

[131] M. A. Troxel et al. *Dark energy survey Year 1 results: Cosmological constraints from cosmic shear.* Physical Review D **D98** (2018). `arXiv:1708.01538`. Cited on pages 74, 76, 86, and 124.

[132] J. Zuntz et al. *Dark energy survey year 1 results: Weak lensing shape catalogues.* Monthly Notices of the Astronomical Society **481** 1149 (2018). `arXiv:1708.01533`. Cited on page 74.

[133] B. Hoyle, D. Gruen, G. M. Bernstein, M. M. Rau, J. de Vicente, et al. *Dark energy survey year 1 results: Redshift distributions of the weak-lensing source galaxies.* Monthly Notices of the Royal Astronomical Society **478** 592 (2018). `arXiv:1708.01532`. Cited on page 74.

[134] M. P. van Daalen, J. Schaye, C. M. Booth, and C. Dalla Vecchia. *The effects of galaxy formation on the matter power spectrum: a challenge for precision cosmology.* Monthly Notices of the Royal Astronomical Society **415** 3649 (2011). `arXiv:1104.1174`. Cited on page 75.

[135] J. Zuntz, M. Paterno, E. Jennings, D. Rudd, A. Manzotti, S. Dodelson, S. Bridle, S. Sehrish, and J. Kowalkowski. *CosmoSIS: Modular cosmological parameter estimation.* Astronomy and Computing **12** 45 (2015). `arXiv:1409.3409`. Cited on page 75.

[136] A. Lewis, A. Challinor, and A. Lasenby. *Efficient computation of cosmic microwave background anisotropies in closed Friedmann-Robertson-Walker models.* The Astrophysical Journal **538** 473 (2000). `arXiv:astro-ph/9911177`. Cited on page 75.

[137] D. Kirk, A. Rassat, O. Host, and S. Bridle. *The cosmological impact of intrinsic alignment model choice for cosmic shear.* Monthly Notices of the Astronomical Society **424** 1647 (2012). `arXiv:1112.4752`. Cited on page 75.

[138] M. Kilbinger, K. Benabed, J. Guy, P. Astier, I. Tereno, L. Fu, D. Wraith, J. Coupon, Y. Mellier, C. Balland, F. R. Bouchet, T. Hamana, D. Hardin, H. J. McCracken, R. Pain, N. Regnaul, M. Schultheis, and H. Yahagi. *Dark-energy constraints and correlations with systematics from CFHTLS weak lensing, SNLS supernovae Ia and WMAP5.* Astronomy & Astrophysics **497** 677 (2009). `arXiv:0810.5129`. Cited on page 75.

[139] C. Howlett, A. Lewis, A. Hall, and A. Challinor. *CMB power spectrum parameter degeneracies in the era of precision cosmology.* Journal of Cosmology and Astroparticle Physics **2012** (2012). `arXiv:1201.3654`. Cited on page 75.

[140] S. Bridle and L. King. *Dark energy constraints from cosmic shear power spectra: Impact of intrinsic alignments on photometric redshift requirements.* New Journal of Physics **9** 444 (2007). `arXiv:0705.0166`. Cited on page 75.

[141] R. Takahashi, M. Sato, T. Nishimichi, A. Taruya, and M. Oguri. *Revising the Halofit model for the nonlinear matter power spectrum.* The Astrophysical Journal **761** (2012). `arXiv:1208.2701`. Cited on page 75.

[142] R. E. Smith, J. A. Peacock, A. Jenkins, S. D. M. White, C. S. Frenk, F. R. Pearce, P. A. Thomas, G. Efstathiou, and H. M. P. Couchman. *Stable clustering, the halo model and non-linear cosmological power spectra.* Monthly Notices of the Astronomical Society **341** 1311 (2003). `arXiv:astro-ph/0207664`. Cited on page 75.

[143] E. Krause and T. Eifler. *COMOLIKE – cosmological likelihood analyses for photometric galaxy surveys.* Monthly Notices of the Astronomical Society **470** 2100 (2017). `arXiv:1601.05779`. Cited on page 76.

[144] F. Köhlinger et al. *KiDS-450: The tomographic weak lensing power spectrum and constraints on cosmological parameters.* Monthly Notices of the Astronomical Society **471** 4412 (2017). `arXiv:1706.02892`. Cited on pages 76 and 112.

[145] B. Joachimi, C. A. Lin, M. Asgari, T. Tröster, C. Heymans, et al. *KiDS-1000 methodology: Modelling and inference for joint weak gravitational lensing and spectroscopic galaxy clustering analysis.* Astronomy & Astrophysics **646** A129 (2020). `arXiv:2007.01844`. Cited on pages 76 and 112.

[146] B. Joachimi, P. Schneider, and T. Eifler. *Analysis of two-point statistics of cosmic shear: III. Covariances of shear measures made easy.* Astronomy & Astrophysics **477** 43 (2008). `arXiv:0708.0387`. Cited on page 76.

[147] M. S. Vogeley and A. S. Szalay. *Eigenmode analysis of galaxy redshift surveys. I. theory and methods.* The Astrophysical Journal **465** 34 (1996). `arXiv:astro-ph/9601185`. Cited on page 77.

[148] A. J. Louca and E. Sellentin. *The impact of signal-to-noise, redshift, and angular range on the bias of weak lensing 2-point functions.* The Open Journal of Astrophysics **3** (2020). `arXiv:2007.07253`. Cited on page 82.

[149] D. Alonso. *Science-driven 3D data compression.* Monthly Notices of the Astronomical Society **473** 4306 (2018). `arXiv:1707.08950`. Cited on page 83.

[150] E. Bellini, D. Alonso, S. Joudaki, and L. V. Waerbeke. *Sheer shear: Weak lensing with one mode.* The Open Journal of Astrophysics **2** (2019). `arXiv:1903.04957`. Cited on page 83.

[151] A. F. Heavens, R. Jimenez, and O. Lahav. *Massive lossless data compression and multiple parameter estimation from galaxy spectra.* Monthly Notices of

the Astronomical Society **317** 965 (2000). `arXiv:astro-ph/9911102`. Cited on pages 89, 91, 93, and 94.

[152] M. Tegmark, A. N. Taylor, and A. Heavens. *Karhunen-Loève eigenvalue problems in cosmology: how should we tackle large data sets?* The Astrophysical Journal **480** 22 (1997). `arXiv:astro-ph/9603021`. Cited on pages 89 and 93.

[153] A. Zablocki and S. Dodelson. *Extreme data compression for the CMB.* Physical Review D **93** 083525 (2016). `arXiv:1512.00072`. Cited on page 89.

[154] D. Gualdi, M. Manera, B. Joachimi, and O. Lahav. *Maximal compression of the redshift-space galaxy power spectrum and bispectrum.* Monthly Notices of the Astronomical Society **4070** 4045 (2018). `arXiv:1709.03600`. Cited on page 90.

[155] A. Heavens, E. Sellentin, D. de Mijolla, and A. Vianello. *Massive data compression for parameter-dependent covariance matrices.* Monthly Notices of the Royal Astronomical Society **472** 4244 (2017). `arXiv:1707.06529`. Cited on page 90.

[156] H. Prince and J. Dunkley. *Data compression in cosmology: A compressed likelihood for Planck data.* Physical Review D **100** 083502 (2019). `arXiv:1909.05869`. Cited on page 90.

[157] R. Ruggeri and C. Blake. *Compressing combined probes: Redshift weights for joint lensing and clustering analyses.* Monthly Notices of the Astronomical Society **498** 2948–2956 (2020). `arXiv:2006.11297`. Cited on page 90.

[158] A. Mootoovaloo, A. F. Heavens, A. H. Jaffe, and F. Leclercq. *Parameter inference for weak lensing using Gaussian Processes and MOPED.* Monthly

Notices of the Astronomical Society **497** 2213 (2020). `arXiv:2005.06551`. Cited on pages 90 and 101.

[159] J. Alsing and B. Wandelt. *Generalized massive optimal data compression.* Monthly Notices of the Royal Astronomical Society **476** L60 (2018). `arXiv:1712.00012`. Cited on page 91.

[160] M. Tegmark, A. Taylor, and A. Heavens. *Karhunen-Loeve eigenvalue problems in cosmology: How should we tackle large data sets?* Astrophysical Journal **480** 22 (1997). `arXiv:astro-ph/9603021`. Cited on page 91.

[161] A. F. Heavens, E. Sellentin, and A. H. Jaffe. *Extreme data compression while searching for new physics.* Monthly Notices of the Royal Astronomical Society **498** 3440 (2020). `arXiv:2006.06706`. Cited on page 94.

[162] K.-H. Yuan and W. Chan. *Structural equation modelling with near singular covariance matrices.* Computational Statistics and Data Analysis **52** 4842 (2008). Cited on page 98.

[163] T. Ferreira and V. Marra. *A fast and reliable method for the comparison of covariance matrices.* (2021). `arXiv:2107.04211`. Cited on page 106.

[164] N. E. Chisari et al. *Core Cosmology Library: Precision cosmological predictions for LSST.* Astrophysical Journal Supplement **242** 2 (2019). `arXiv:1812.05995`. Cited on page 107.

[165] A. Blanchard et al. *Euclid preparation: VII. Forecast validation for Euclid cosmological probes.* Astronomy & Astrophysics **642** A191 (2020). `arXiv:1910.09273`. Cited on page 107.

[166] A. H. Wright et al. *KiDS+VIKING-450: A new combined optical and near-*

*infrared dataset for cosmology and astrophysics.* Astronomy & Astrophysics **632** A34 (2019). `arXiv:1812.06077`. Cited on page 111.

[167] A. Edge, W. Sutherland, K. Kuijken, S. Driver, R. McMahon, S. Eales, and J. P. Emerson. *The VISTA kilo-degree infrared galaxy (VIKING) survey: Bridging the gap between low and high redshift.* The Messenger **154** 32 (2013). Cited on page 111.

[168] H. Hildebrandt et al. *KiDS-450: Cosmological parameter constraints from tomographic weak gravitational lensing.* Monthly Notices of the Astronomical Society **456** 1454 (2017). `arXiv:1606.05338`. Cited on page 111.